Chemical Adsorption and Reaction Processes on Single Crystal Surfaces of Metal Oxides

（金属酸化物の単結晶表面における化学吸着と反応過程）

氏 名 大西 洋

Hiroshi Onishi

Chemical Adsorption and Reaction Processes on

(1)

Chemical Adsorption and Reaction Processes on Single Crystal Surfaces of Metal Oxides

(金属酸化物の単結晶表面における化学吸着と反応過程)

by Hiroshi Onishi

A Thesis Submitted to The University of Tokyo
for The Degree of Doctor of Science
December, 1992

金子　功・芳江夫妻にささぐ

Contents

Chapter 1

Introduction

1.1. General remarks

Modern chemistry is constructed on the basis of understanding of molecular structures in an atomic level. Physical and chemical properties of substance are discussed, as if we could distinguish individual atom in materials; bond length, bonding angle, coordination number, atomic distance and distribution of orbitals are considered. The principle has brought victories in molecular science.

Catalytic chemistry, especially over solid catalysts, is however often regarded as art rather than science, because it has deviated from the general principle. Catalysis is one of the most interesting and challenging fields in chemistry. Reaction brings us to a dynamic world of chemistry. As soon as a reaction starts, novel species appear and play an important role as reaction intermediates, which are never stable in a static world at equilibrium. There is huge amount of experience accumulated in a traditional field of catalytic chemistry. The experience is mainly devoted to discovery of new catalysts of demanded performances without clear picture of reaction sites, reaction interme-

diates and reaction processes. Model study on chemical processes is thus required over well-defined surface of solid to address the experience properly, and to deduce a general picture in catalysis. Here, I have investigated chemical adsorption and reaction processes on single crystal surfaces of metal oxides to bring a new aspect in catalytic chemistry. The goal of this work is a better understanding of reaction sites on metal oxide in the light of microscopic structure.

1.2. Why metal oxide ?

Metal oxide is popular material in catalytic chemistry. It has been employed as active catalyst and support for metal supported catalyst. Many studies on polycrystalline powders have revealed that catalytic properties over metal oxide strongly depend on the preparation and history of catalysts. In recent years, chemistry on well-defined surface of metal oxide is attracting attention in surface science community. Experimental [1-5] and theoretical [6] studies on single crystal surface pointed out that local coordination environment at surface controls the dissociation of adsorbed water on metal oxide.

Metal oxide is ionic compound. Ionic character distinguishes metal oxide from metal or covalent semiconductor. Metal oxide hence catalyzes chemical reactions in much different way from metal. Ionic adsorbate, ionic intermediate, and ionic transition state are favored on metal oxide. Redox property is another character on metal oxide. Various reactions occur with redox process of metal cation.

My work is focused on two aspects on metal oxide: acid-base property and interaction with metal adatoms. Acid-base character is one of the most typical properties that plays an important role in ionic reaction processes. Selectivity in the decomposition reaction of formic acid is employed as a scale: dehydration for acidic oxides, and dehydrogenation for basic oxides [9,10]. Parallel behavior is seen in the decomposition of alcohols [11]. Isomerization of 1-butene yields high stereo-selectivity in 2-butene; *trans* for acidic oxides and *cis* for basic oxides [12].

Cracking is an important reaction in industry and catalyzed by acidic catalysts [13].

Metal oxide is also indispensable support for supported metal catalyst; small metal particles with $1\text{-}10^3$ metal atoms are supported on powdery metal oxide. Most of industrial catalysts are designed in this way. Catalytic reactions over supported metal catalysts are markedly affected by the nature of supports [7] and the size of metal particles [8]. Interaction through the interface of metal and metal oxide affects physical and hence catalytic properties on metal particles.

Nevertheless, surface scientific techniques have been believed to be unavailable on metal oxide. Electron spectroscopies, such as X-ray photoelectron spectroscopy (XPS), ultraviolet photoelectron spectroscopy (UPS), Auger electron spectroscopy (AES), electron energy loss spectroscopy (EELS) and low energy electron diffraction (LEED), could not be applied on metal oxide due to charge up under irradiation. Thermal desorption spectroscopy (TDS) is another powerful method to characterize adsorbate and substrate. Low electric conductivity would hinder TDS measurement on metal oxide. I designed devices suitable for oxide crystals to overcome the inevitable barriers. For example; a flood electron gun for charge compensation, and sample holding device to cool and heat crystals. The details of experiments are mentioned in Chapter 2.

In addition, stable surfaces of metal oxides cannot adsorb "pet" molecules on metals, such as CO, H_2 and C_2H_4. Surface scientist familiar with metal surface was also afraid of surface stoichiometry on metal oxide. Accordingly, less studies have been performed on metal oxides, while surface chemistry on metals has been extensively developed in 1970's [14]. Most of surface scientists paid no attention on metal oxide, when I started this work in 1985. Surface chemistry on well-defined metal oxides, therefore, must be challenging but promises new fruitful fields in surface science.

1.3. Chemisorption on single crystal metal oxide

The first part of this work relates chemical adsorption with microscopic structure on metal oxide. It is reasonable to expect that roughness or defect plays an important role in catalysis, because these open structures cause reactive electronic states located in band gap region [1-6].

Microfacets are used to introduce coordinative unsaturation on MgO, while a stepped surface with high index is employed on TiO_2(rutile). Recently, this approach was extended on faceted TiO_2(001) to find that four-fold Ti^{4+} cations with multiple coordination vacancy is capable of C-C bond formation [15].

1.3.1. MgO(100) and faceted MgO(111)

Magnesium oxide is a typical basic oxide which catalyzes the hydrogenation of 1,3-butadiene [16], the H_2-D_2 exchange reaction [17] and the dehydrogenation of formic acid [9] and alcohols [10]. The structure of active sites on MgO catalyst is still open to discussion. A photoluminescence study [18] has suggested that active sites are poorly coordinated Mg-O pairs on stepped sites or high-index planes. Indeed, MgO smoke exclusively exposing (100) plane was found to be inert for the isomerization reaction of 1,3-butadiene [16]. Theoretical studies based on DV-Xα calculation support this suggestion [6,19,20].

Little has been investigated concerning the interactions of atoms and molecules with single crystal surfaces of MgO. Nonpolar (100) plane is stable, while polar ideal (111) planes with Mg or O toplayer are unstable. Argon sputtering and thermal annealing result in faceting on a MgO(111) surface [21], as shown Fig.1-1. The effect of local coordination environment on chemical adsorption is examined, comparing faceted (111) and flat (100) surfaces. Chemisorption of atomic Na and small molecules such as H_2O, CH_3OH, CO_2, HCOOH and $HCOOCH_3$ are studied in Chapter 3 to reveal enhanced reactivity of edge-sites on the facets.

1.3.2. TiO_2(110) and stepped TiO_2(441)

Titanium dioxide is a famous photoelectrode [22]. It is not an insulator and hence suitable for electron spectroscopy. Large crystal is available only for rutile at present, though titanium dioxide has two other crystal structures, anatase and brookite, both of which are slightly distorted from the structure of rutile [23]. Several pioneering works revealed structure and elctronic states at surfaces of rutile with LEED, UPS and ELS [1-6,24]. Oxygen anion is readily sputtered off by argon ion beam. Resulted vacancy reduces adjacent two Ti^{4+} cations into Ti^{3+} state. The twin-Ti^{3+} site dissociates water molecule, while molecularly adsorbed water is observed on the stoichiometric surface [24]. A more recent study on $Ti_2O_3(10\bar{1}2)$ showed that d^1 state on an isolated cation site is not sufficient to dissociate water [1,2,25].

(110) plane is most stable surface on rutile. Facets on (001) surface [26,27] and (1x3)-reconstructed structure on (100) surface [28] consist of (110) microplanes. The largest stability results from the best coordination on (110) surface. A half of Ti cations maintain six-fold coordination; the other half are five-fold coordinated [1-5,24]. TiO_2(110) has also an anisotropic structure. Figure 1-2 illustrates ridges of oxygen atoms run along the [001] direction. The five-fold cations sit on the valleys.

In Chapter 4, a TiO_2(441) surface is prepared and compared with a (110) surface in chemisorption. LEED shows that (441) surface has a regular step structure indexed as 3(110)x(111); (110) terrace with 3-unit width and (111) step with 1-unit height are regularly arranged. Chemical adsorption of CH_3OH and SO_2 is studied with XPS, UPS and LEED. The molecules are adsorbed in the same way on the (110) surface and on the stepped (441) surface. The two oriented surfaces are equivalent in local coordination environment against (111) steps; Ti cations hold five- or six-fold coordination. Hence it is reasonable that the molecules cannot distinguish stepped structure on (441) surface.

1.4. Catalytic reaction on single crystal metal oxide

Previous studies on metal oxide single crystals, including my work in Chapter 3 and 4, have been mainly focused on characterization of adsorbates and their reaction at surface, applying electron spectroscopy and thermal desorption spectroscopy. I attack more dynamic and catalytic phenomena in Chapter 5. This is the first successful observation of catalytic reaction on well-defined single crystal metal oxide in a steady state, to my knowledge [29]. A kinetic study on MoO_3 supported on graphite powder suggested that Mo_3O(100) plane catalyzes partial oxidation reaction of propylene to acrolein, while MoO_3(010) cannot [30]. But they employed a statistic analysis to deduce crystallographic dependence and remained some uncertainty.

Adsorption and catalytic decomposition reaction of formic acid are studied in Chapter 5, in order to consider traditional acid-base concept in the light of microscopic structure of reaction site. Acid-base character is one of the most typical properties that plays an important role in wide range of catalytic performance on metal oxide. Selectivity in the decomposition reaction of formic acid has been employed as a scale for acid-base property.

TiO_2(110) remains an ideal surface structure under the catalytic decomposition reaction of formic acid as demonstrated in Chapter 5. Strong ionic construction in metal oxides denies reconstruction under reaction conditions, whereas metals often reconstructs and forms surface compounds with adsorbed species [31]. This conservative property is an advantage for metal oxide to estimate reacting structures, since it is difficult to directly determine surface structure under atmosphere of reactants.

1.5. Surface modification by metal adatoms

Metal/metal-oxide interface plays an important role in heterogeneous catalysis. Catalytic properties of metal particles supported on metal oxides are often markedly affected by

oxide supports [7] as well as particle size of metals [8]. The effects have been attributed to interaction through metal and metal oxide interface. Less investigations [32-43], however, were performed with well-characterized metal-insulator interface, though metal-metal and metal-semiconductor (Si, Ge, GaAs, etc.) [44] interface have been extensively studied.

Physical and chemical properties of sodium adlayers on TiO_2(110) are studied in Chapter 6 and 7. Na adatoms provide a model for charge transfer between metal adatoms and metal oxide substrate. Nickel adlayers are examined over TiO_2(110) in Chapter 7, as a more realistic case for supported-metal catalyst.

1.5.1. Sodium adatoms on TiO_2(110)

Alkali additives play an important role in adsorption and catalysis over solid surfaces. Alkali adatoms on transition metal surfaces have been an intense subject of surface science in connection with catalytic promotion and adsorbate-adsorbate interaction [45]. Bonding of alkali adatoms with substrate is also a fundamental issue in surface physics [46]. In addition, alkali adlayers exhibit interesting behaviors such as, insulator-conductor transition [47] and overlayer plasmon excitation [48].

On the other hand, alkali dopants remarkably enhance basic character on metal oxide catalysts. Polycrystalline magnesium oxide deposited with sodium exhibits so strong-base catalysis that is called "super-base" [49]. Oxidative dimerization of methane through methyl radical intermediate was reported on Li-doped [50] and Na-doped [51] MgO catalysts. Li or Cs on MgO [52] and ZnO [53,54] were studied in relation to electron emitters.

Chapter 6 deals with Na adatoms on TiO_2(110) surface. Na adatoms interact with oxygen anions and affect surface electronic states through a large charge transfer on TiO_2(110). Na adatoms give a c(4x2) ordered overlayer composed of ensembles of four Na adatoms and two oxygen anions, named as "Na2O-dimer" unit. The ensembles promote the substrate to react with carbon dioxide to form carbonate and to dissociate nitric monoxide to

form nitride. The mechanisms for the genesis of the reactivities are discussed in Chapter 7.

1.5.2. Ni adatoms on TiO_2(110)

Nickel particles supported on TiO_2 powder exhibit a higher activity for CO hydrogenation reaction than those on other supports [55]. The structure and the electronic states of Ni adatoms are discussed in Chapter 8. Chemisorbed states of CO on the adlayers are also examined, as a prototype of interfaces of transition metal and metal oxide.

1.6. References

1. V.E.Henrich, Rept.Prog.Phys.48(1985)1481.
2. V.E.Henrich, Progr.Surf.Sci.14(1983)175.
3. V.E.Henrich, Progr.Surf.Sci.9(1979)143.
4. W.Göpel, Progr.Surf.Sci.20(1985)9.
5. G.Heiland and H.Lüth, in: The Chemical Physics of Solid Surfaces and Heterogeneous Catalysis, Vol.3, Elsevier,Amsterdam(1984), Chap.4.
6. M.Tsukada, H.Adachi and C.Satoko, Progr.Surf.Sci.14(1979)113.
7. G.L.Haller and D.E.Resasco, Adv.Catal.36(1989)173.
8. M.Che and C.O.Bennett, Adv.Catal.36(1989)55.
9. P.Mars,J.J.F.Scholten and P.Zwietering, Adv.Catal.14(1963)35.
10. J.J.F.Scholten,P.Mars,P.G.Menon and R.van Hardereld, Proc.3rd Intern.Congr.Catal. Vol.2, Wiley, New York(1965), p.881.
11. Z.G.Szabo, J.Catal.6(1966)458.
12. J.C.Volta,J.M.Taitbouet,C.Phichitkul and J.E.Germain, Proc.8th Intern.Congr.Catal., Vol.IV, Springer, Berlin(1984), p.451.
13. B.C.Gates, in: Chemistry in Catalytic processes, McGraw-Hill, New York(1979), Chap.1.
14. G.A.Somorjai, in: Chemistry in Two Dimensions: Surfaces, Cornell University Press, Ithka(1981)
15. H.Idriss,M.Libby and M.A.Barteau, Catal.Lett.,in press.
16. K.Miyahara, Y.Murata, I.Toyoshima, Y.Tanaka and T.Yokoyama, J.Catal.68(1981)186.
17. M.Boudart, A.Delbouille, E.G.Derouane, V.Indovina and A.B.Walters, J.Am.Chem.Soc.94(1973)6622.
18. S.Coluccia and A.J.Tench, Proc.7th.Intern.Congr.Catal., Kodansha/Elsevier, Tokyo(1981), B1154.
19. C.Satoko, M.Tsukada and H.Adachi, J.Phys.Soc.Jpn.45(1978)1333.
20. M.Tsukada and T.Hoshino, J.Phys.Soc.Jpn.,51(1982)2562.
21. V.E.Henrich, Surf.Sci.57(1976)385.
22. A.Fujishima and K.Honda, Nature 238(1972)37.

23. R.G.W.Wyckoff, in: Crystal Structure 2nd edition, Wiley, New York(1966).
24. W.J.Lo, Y.W.Chung and G.A.Somorjai, Surf.Sci.71(1978)199.
25. R.L.Kurtz and V.E.Henrich, Phys.Rev.B26(1982)6682.
26. L.E.Firment, Surf.Sci.116(1982)205.
27. K.S.Kim and M.A.Barteau, J.Catal.125(1990)353(1990).
28. P.Zschck,J.B.Cohen and Y.W.Chung, Surf.Sci.262(1992)395.
29. J.A.Rodriguez and D.W.Goodman, Surf.Sci.Rept.14(1991)1.
30. R.J.Kokes, Proc.5th Intern.Congr.Catal., Elsevier, Amsterdam,(1973), A-1.
31. for example; carbon adlayer forms stable surface carbide in p(2x2)-p4g symmetry. see J.H.Onuferko, D.P.Woodruff and B.W.Holland, Surf.Sci.87(1978)357.
32. C.C.Kao, S.C.Tsai, M.K.Bahl, Y.W.Chung and W.J.Lo, Surf.Sci.95(1980)1.
33. H.R.Sadeghi and V.E.Henrich, Appl.Surf.Sci.19(1984)330.
34. M.C.Wu and P.J.Mϕller, Surf.Sci.235(1990)228.
35. H.R.Sadeghi and V.E.Henrich, J.Catal.109(1988)1.
36. G.Rocker and W.Göpel, Surf.Sci.181(1987)530.
37. G.L.Haller and D.E.Resasco, Adv.Catal.36(1989)173.
38. K.Tamura, U.Bardi and Y.Nihei, Surf.Sci.216(1989)209.
39. S.Fuentes, A.Vázquez, J.G.Perez and M.J.Yacamán, J.Catal.99(1986)492.
40. H.R.Sadeghi, D.E.Resasco, V.E.Henrich and G.L.Haller, J.Catal.104(1987)252.
41. P.Dolle, K.Markert, W.Heichler, N.R.Armstrong, K.Wandelt, K.S.Kim and R.A.Fiato, J.Vac.Sci.Technol.A4(1986)1465.
42. T.Asakawa, K.Tanaka and I.Toyoshima, Langmuir 4(1988)521.
43. E.I.Altman and R.J.Gorte, Surf.Sci.172(1986)71.
44. H.Yasunaga and A.Natori, Surf.Sci.Rept.15(1992).
45. H.P.Bonzel, Surf.Sci.Rept.8(1987)43.
46. T.Aruga and Y.Murata, Prog.Surf.Sci.31(1989)61.
47. T.Aruga, H.Tochihara and Y.Murata, Surf.Sci.158(1985)490.
48. T.Aruga, H.Tochihara and Y.Murata, Phys.Rev.Lett.53(1984)372.
49. J.Kijenski and S.Marinowski, Bull.Acad.Polonaise Sci.25(1977)428.

50. D.J.Driscoll, W.Martir, J.X.Wang and J.H.Lunsford, J.Am.Chem.Soc.107(1985)58.
51. T.Moriyama, N.Takasaki, E.Iwamatsu and K.Aika, Chem.Lett.(1986)1165.
52. N.T.Bagraev and V.L.Vorisov, Appl.Surf.Sci.4(1980)145.
53. R.A.Powell and W.E.Spicer, J.Appl.Phys.48(1977)4311.
54. R.Leysen, B.J.Hopkins and P.A.Taylor, J.Phys.C8(1975)907.
55. M.A.Vannice and R.L.Garten, J.Catal.56(1979)236.

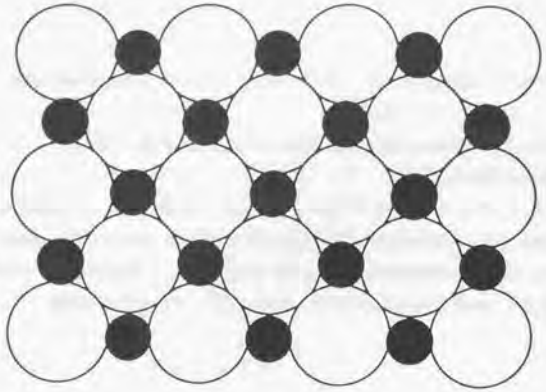

MgO(100) surface

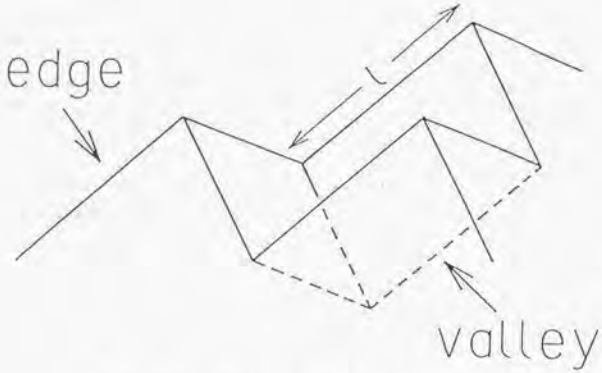

faceted MgO(111) surface

Trigonal pyramids are composed of
a set of (100), (010) and (001) planes.

Fig.1-1 Illustration for single crystal surfaces of MgO.
filled circle: Mg cation, open circle: O anion.

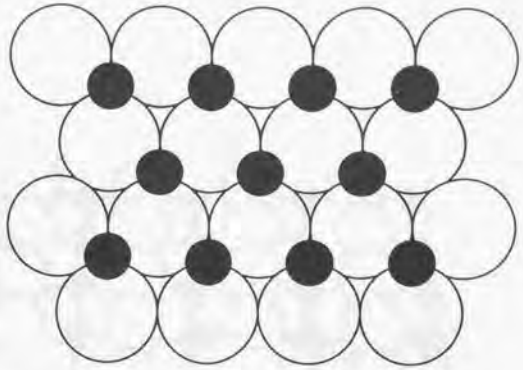

Ideal MgO(111)-Mg surface

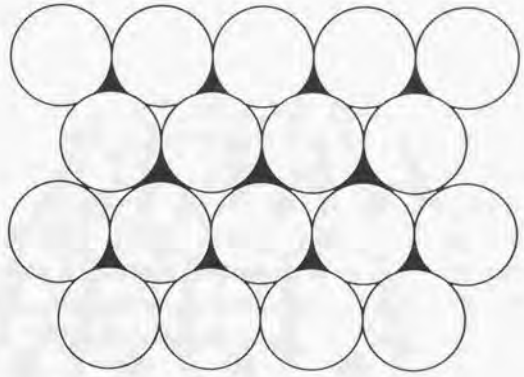

Ideal MgO(111)-O surface

(Fig.1-1. continued.)

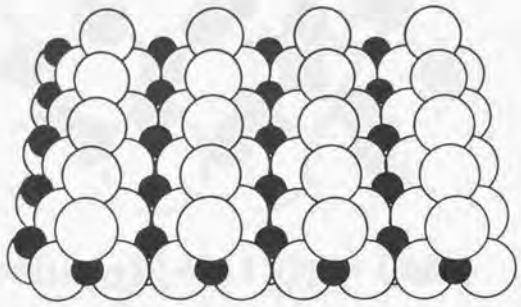

TiO_2(110) surface

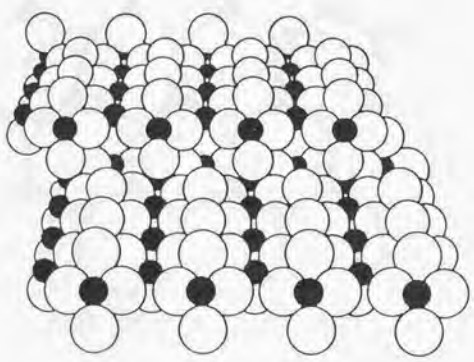

stepped TiO_2(441) surface

Fig.1-2 Illustration for single crystal surfaces of TiO_2. filled circle: Ti cation, open circle: O anion.

Chapter 2

Experimental

2.1. Outlook

The experiments were carried out in a commercial chamber (VG-ESCALAB) capable of AES, LEED, XPS and UPS measurments with a base pressure of 6×10^{-11} Torr. I made the following devices to perform this work: (1) a manipulator and a sample holding device to heat and cool metal oxide crystal, (2) a multimass TDS system, (3) a data processing system for electron spectrum, and (4) a flood electron gun for charge compensation in UPS measurement. They are briefly mentioned below. See also the experimental sections in the following chapters.

2.2. Holding device

A holding device was designed to cool and heat sample wafer linearly through 100-900 K; the wafer and a MgO crystal were tightly bound each other with tantalum wire (0.1 mmϕ), sandwiching a gold plated tungusten mesh (0.03 mmϕ, 100 mesh). The mesh is welded on a couple of feedthrus and resistively heated, while the feedthrus were attached to a liq. N_2 reservoir to be cooled.

The rare face of the wafer was coated with gold to promise a good contact. A chromel-alumel thermocouple was fixed at an edge on the sample surface with ceramic glue (Aronceramic-C). This device allowed a ramping rate of 5 K/s during TDS measurement with electric power below 20 W. Good contact and small power for heating minimize desorption from the holder itself. The holder stood on an end of the horizontal rod of a manipulator. The manipulator allowed X,Y,Z-motion and rotation around the X-axis.

When the device was not available, crystal was fixed on a standard nickel holder of VG. The crystal was thereby heated with electron bombardment. It was difficult to control temperature precisely on VG-holder, though which was convenient to exchange samples.

2.3. Electron spectroscopy

XPS was available even on insulating crystals of MgO. Mg-Kα or Al-Kα line was used for excitation. The photoelectrons could escape out of the surface, due to large kinetic energy and small yield. There still remained small shifts in kinetic energy by several eV. The binding energy was hence referred to an internal reference to caribrate the shifts in kinetic energy scale. Oxygen 1s levels of oxygen anion in substrate lattice were employed as the references after the first standard of Au(4f7/2) level of 83.8 eV in gold film deposited on substrate. Surface density of adsorbate was estimated on the intensity in XPS emission normalized to that of lattice oxygen anions. Relative cross section, escape depths and transmission of the analyzer were considered.

UPS measurement needed a flood electron gun [1] to compensate charge-up on MgO. The photoelectrons excited by HeII radiation have kinetic energy smaller than 40 eV. They could not leave away from surface of MgO. The flood gun was composed of filament, extractor, shade and focus electrode. The filament is grouded and extracted electrons flue to the sample pulled by the accumulated charge. Beam current was 1 μA or less on crystal. The binding energy in UPS were referred to the upper

edge of valence band on MgO. On the other hand, UPS and AES were available on TiO_2 crystals without compensation. The work function was obtained from the cut-off of secondary electrons in HeI UPS spectrum on TiO_2 [2].

LEED pattern was observed with a usual four grid optics. Electron energy loss spectrum (ELS) was recorded with primary electron beam supplied by the electron gun in the optics. A hemispherical spectrometer analyzed the kinetic energy of inelastically scattered electrons.

The data acquisition system for electron spectroscopy consists of a signal averager 1170 (Nicolet) and a microcomputer FM-8 (Fujitsu) or PC-9801 (NEC). Output pulses of a channeltron were counted with the averager and obtained spectrum was sent into the computer In analyzing mode, spectrum was deconvoluted and fitted with Gaussian or Lorentzian functions.

2.4. Thermal desorption spectroscopy

A computer (NEC PC-9801) drove sample temperature through a PID controller. A quadrupole mass filter (UTI-200) was also operated by the computer. Combined with the holding device, TDS spectra of 8 mass numbers were recorded at the same time with heating rate among 0.1-5 K/s on metal oxide.

2.5. Sample preparation

Single crystal rods of MgO and TiO_2 were obtained from Murakami Engineering Co. or Earth Jewellery Co. in Japan. Oriented wafers were cut out with a diamond wheel saw and polished over 0.05 μm Al_2O_3 powder. Mechanically damaged layer was removed by chemical etching. H_3PO_4 solution [3] and 5N NaOH [4] were employed for MgO and TiO_2 after literature, respectively. The wafers were annealed in air above 1000 K before cleaning under vacuum. This high temperature annealing promised good quality in crystallization without deviation from stoichiometry. High temperature treatment under vacuum often leads to release of oxygen. Subsequently, argon ion sputtering and moderate

annealing were repeated in the chamber, until contamination was removed. Detailed procedure on individual material is described in the following chapters.

2.6. Metal deposition

Commercial sources (SAES Getters) were used for alkali deposition. A couple of feedthrus held the sources and a liq. N_2 reservoir cooled them, so that pressure was maintained below 6×10^{-10} Torr during deposition. Nickel was evaporated from a Ni drop welded on tungusten wire in the same way. The rate of deposition was constant in a course of experiments.

2.7. Gas exposure

Reactant gases of research grade were out-gassed with trap-thaw cycles. A capillary doser (ca.0.2 mmϕ) introduced the gases in front of sample surface. The doser was separately calibrated in dosing CO on a Pd surface. Effective pressure over the surface could be estimated as 20 times larger than the scale on the gauge.

2.8. Kinetic measurement

A pressure jump method was adopted to measure the rate of catalytic reaction over a single crystal in a steady state; the crystal maintained at reaction temperature slides into a stream of reactant molecules down the doser. Catalytic reaction occurs over the surface to give jumps in the partial pressure of products. Idearlly, the reaction rate corresponds to the jumping height for individual product. See Chapter 5 in detail.

2.9. References

1. D.A.Huchital and R.T.Mckeon, Appl.Phys.Lett.20(1972)158.
2. S.Evans, Chem.Phys.Lett.23(1973)134.
3. V.E.Henrich, Surf.Sci.57(1976)385.
4. Y.W.Chung, W.J.Lo and G.A.Somorjai, Surf.Sci.64(1977)588.

Chapter 3

Adsorption of atomic Na and oxygenated molecules on MgO(100) and faceted (111) surface

3.1. Abstract

Adsorption of atomic Na and oxygen-containing molecules such as H_2O, CH_3OH, CO_2, HCOOH and $HCOOCH_3$ are studied on annealed MgO(100) and (111) surfaces by means of XPS, UPS and LEED. The (111) surface annealed to 1000 K under vacuum yields trigonal microfacets ca. 2 nm across. The faceted (111) surface composed of (100) microplanes is more reactive than the annealed (100) surface. The observed promotion on the faceted (111) surface suggests that cation-anion pair with coordinative vacancy on edges of facets is reactive site for chemisorption.

3.2. Introduction

Magnesium oxide is a typical basic oxide which catalyzes the hydrogenation of 1,3-butadiene [1], the H_2-D_2 exchange reaction [2] and the dehydrogenation of formic acid or methanol [3]. Na additives increase the strength of basic character on MgO catalyst [4]. Li [5] or Na [6] dopants promote the CH_4 coupling reaction to $C_2H_6+C_2H_4$ through methyl radical intermediate on MgO [5]. Many experiments with polycrystalline powder of MgO have been carried out on catalytic interests. The structure of active site and the origin of basic character, however, still remain to be resolved on MgO catalyst. A recent photoluminescence study [7] suggested that active sites are poorly coordinated Mg-O pairs on step structure or high-index plane. Theoretical studies based on DV-Xα calculations for surface electronic states support this suggestion [8-10].

Little has been investigated concerning chemisorbed atoms and molecules on single crystal surface of MgO. Magunesium oxide has a NaCl structure. Non-polar MgO(100) plane is stable, while polar MgO(111) plane with Mg or O toplayer is unstable. Argon sputtering and thermal annealing result in trigonal facets on MgO(111) [11]. Here, the faceting is utilized to introduce well-defined edge structure on a MgO(111) surface. Adsorption of atomic Na and oxygen-containing molecules such as H_2O, CH_3OH, CO_2, HCOOH and $HCOOCH_3$ are compared on a faceted (111) and a (100) surface with XPS, UPS and LEED.

3.3. Experimental

The experiments were carried out in an ultra high vacuum chamber (VG-ESCALAB) with a base pressure of 6×10^{-11} Torr. XPS and UPS signal obtained with a hemispherical analyzer were processed by a microcomputer. The binding energy in XPS excited by Mg-Kα or Al-Kα were referred to the Au(4f7/2) level of 83.8 eV in gold film deposited on the MgO crystals. A flood electron gun was employed against charge-up in UPS measurement excited by HeII radiation [12]. The binding energy in UPS were referred to the upper edge of valence band (Ev). Work function could not be measured, because flood electrons were scattered to superpose over lower cutoff region of photoelectrons.

Reactant gases of research grade were purified by molecular sieves and repeated trap-thaw cycles. Their purity was checked by gas chromatography. They were admitted on sample through a variable leak valve. Pressure was estimated ca. 10^{-6} Torr on the sample surfaces. A commercial source (SAES

Getters) was used in Na deposition. Pressure was maintained below 6×10^{-10} Torr during deposition.

A single crystal rod of MgO was obtained from Murakami Engineering Ltd. Wafers of (100) and (111) orientations, determined by the Laue method, were cut out with a diamond wheel saw. They were mechanically polished over 0.05 μm Al_2O_3 powder and then chemically etched in H_3PO_4 (85%) at 373 K for 30 s [11]. In the UHV chamber the wafers were sputtered with Ar^+ ion at 3 keV and 10 μA for 2 min, followed by annealing with electron bombardment. Temperature was estimated from color during annealing.

3.4. Results

3.4.1. Clean surface

Chemical etching gave a highly reflecting surface for the (100) wafer, whereas the (111) crystal took on a milky hue due to scratches. Carbon was a main contaminant and was readily swept out by Ar^+ sputtering. Subsequent annealing under vacuum to 1000 K for 2 min gave a good (1x1) pattern on the (100) sample. Diffraction on the similarly annealed (111) wafer was diffuse, but exhibited an apparent three-fold symmetry. Figure 3-1 shows the LEED patterns recorded on the (111) crystal with primary electron of 95, 100 and 105 eV. When the primary energy was slightly changed, the spots were splitted and some diffuse streaks appeared in non-radial directions. These behavior depicts a characteristic feature of trigonally pyramidal facets composed of (100), (010) and (001) planes inclined by 54.7° from the original (111) plane [11]. The dimension of facets was estimated about 2 nm on spread of the diffuse streaks; the spot diameter $\delta\psi$ is inversely proportional to the diameter of the ordered region d [13],

$$\delta\psi \simeq \lambda/(2d\cos\psi) \quad (1)$$

where λ and ψ are wave length of electron and angle of diffraction, respectively. Figure 3-1c gave $\delta\psi$ of 3° with

Ep=95 eV and ψ=54.7°. The faceted surface was stable against the cleaning cycles.

HeII UPS spectra on MgO(100) and (111) surface are shown in Fig.3-2. Valence bands mainly composed of O(2p) orbitals were observed. These spectra are consistent with a theoretical calculation for (100) plane [9] and UPS results on MgO film [14] and MgO(100) [15]. A theoretical study predicted occupied states in the band gap region on an ideal MgO(111) polar plane [10]. The absence of the predicted emission is reasonable on faceted structure. Small peaks located in the band gap are assigned to satellites excited by HeIIβ emission ($h\nu$=48.4 eV).

3.4.2. Na deposition

(a) MgO(100) surface

Na deposition on the MgO(100) surface was monitored with Na(1s) and Mg(1s) levels in XPS. Intensity, $I_{Na(1s)}$ and $I_{Mg(1s)}$, was normalized on that of Mg(2s) peak, $I_{Mg(2s)}$, to minimize instrumental fluctuations. The escape depth for Na(1s), Mg(1s) and Mg(2s) electrons is estimated as 1, 0.6 and 2.4 nm, respectively. The intensity of Na(1s) and Mg(1s) emissions is plotted with exposure time to Na vapor in Fig.3-3a. A break was observed on Na(1s) at 1 min followed by a gentle slope, while the intensity of Mg(1s) remained constant. Surface density of Na, σ_{Na}, was estimated as 1×10^{18} m^{-2} at the break, taking account of the escape depths, cross sections and relative transmission of the spectrometer.

The up-take plot indicates that Na atoms are adsorbed on MgO(100) forming three-dimensional islands around nuclei seeded in the early stage of exposure within 1 min. This is compatible with the fact that no significant change was observed in LEED through deposition. Furthermore, the binding energy of Na(1s) showed negligible shift as shown in Fig.3-3b, and UPS spectra showed no change at various stages of deposition. These results suggest negligible chemical interaction between Na adatoms and MgO(100) substrate.

When Na adlayers on MgO(100) with $I_{Na(1s)}/I_{Mg(2s)}$=1.7 was

exposed to 10^3 L O_2 at 298 K, new three peaks appeared in UPS as shown in Fig.3-4a (1 L=10^{-6} Torr.s). They are regarded as a fingerprint of Na atoms bound with oxygen anions, probably forming sodium oxide.

(b) faceted MgO(111) surface

Normalized intensity $I_{Na(1s)}/I_{Mg(2s)}$ linearly increased with exposure time on the faceted (111) wafer. A break was observed at 5 min in Fig.3-3a. The rate of increase becomes parallel to that on (100) after the break. Mg(1s) level linearly decreased to saturate after the break, coinciding with the initial increase in Na(1s). The results suggest atomic layer growth of Na on the faceted MgO(111) surface and subsequent three-dimensional nucleation. Surface density was estimated as 5×10^{18} m^{-2} at the break. No change was observed in LEED during exposure.

As the first Na layer grew, the binding energy of Na(1s) decreased by 0.7 eV as shown in Fig.3b. An ionization shift of 0.7 eV was reported on Na_2O film [16]. The observed shift demonstrates partial ionization of Na adatoms in the initial stage of atomic layer growth. Valence orbitals are also markedly affected by Na adatoms. Difference spectrum for the completed first layer (t=5 min.) has characteristic three peaks in Fig.3-4b. They are quite similar to those in curve a which is assigned to sodium adatoms interacting with oxygen atoms. Thus Na adatoms in the atomic layer interact with oxygen anions on the facets to be partly ionized.

Figure 3-5 shows Na(1s) emission in XPS with increasing exposure. Satellite emissions at higher binding energy gained intensity, after the first layer was completed. They are assigned into plasmon losses, demonstrating metallic property of nucleated multilayer. Exposure of 18 min caused satellites with loss of 3.9 and 5.2 eV in Fig.3-5c. They correspond to reported values of surface and bulk plasmon over sodium metal, 4.1 and 5.8 eV, respectively [16]. The plasmon peaks disappeared on subsequent oxidation with 10^3 L O_2 at 298 K, increasing $I_{Na(1s)}/I_{Mg(2s)}$ from 1.0 to 1.4. These results suggest that metallic islands of Na are readily oxidized with molecular

oxygen and resultant sodium oxide spreads over the MgO substrate.

3.4.3. Gas adsorption

Adsorption of H_2O, CH_3OH, CO_2, HCOOH, $HCOOCH_3$, O_2, H_2, N_2O, CO, C_2H_4 and 1,3-C_4H_6 were examined with 10^3 L exposure at 298 K on the (100) and the faceted (111) crystals. O_2, H_2, N_2O, CO, C_2H_4 and 1,3-C_4H_6 were not adsorbed on both the surfaces. Exposure to H_2O, CH_3OH, CO_2, HCOOH and $HCOOCH_3$ gave rise to new peaks in XPS. Table 3-1 summarizes binding energy and calculated surface density of target atoms in adsorbate. The amount of adsorbate other than formic acid is larger on the faceted (111) than on the (100) surface. UPS difference spectra on the (111) surface are shown in Figs.3-6 to 3-10. The spectra recorded on the (100) surface were similar to them. Uniform background in LEED increased in intensity upon adsorption. The adsorbed species were stable up to 365 K under UHV conditions.

(a) Water

The UPS difference spectrum in Fig.3-6a for adsorbed water on the MgO surfaces gave a two-peak structure characteristic of hydroxide anion in Fig.3-6b [17]. Fuggle et al. [18] reported a shift of 2.4 eV in binding energy of O(1s) level for hydroxyl anion based on oxide anion. XPS data in Table 3-1 are consistent with the reported shift. Hence it is concluded that water is dissociated to form hydroxyl anions on the MgO surfaces.

(b) Methanol

The UPS difference spectrum on methanol adsorbed MgO(111) is shown in Fig.3-7a, where three peaks were observed. The methoxide on Cu(110) exhibited similar three peaks as shown in Fig.3-7b [19]. Thus methanol is dissociatively adsorbed on the MgO surfaces. Hydrogen atoms dissociated from methanol are trapped on surface oxygen anions to form hydroxyl groups, because surface density of hydroxyl groups with shifted binding energy in O(1s) is larger by a factor of about two than the density of

carbon. Oxygen atom in methoxide and hydroxide cannot be distinguished in XPS.

(c) Carbon dioxide

Three peaks were observed in UPS of Fig.3-8a after CO_2 adsorption. They are assigned to carbonate ion, CO_3^{2-}, in comparison with UPS spectrum of K_2CO_3 film shown in Fig.3-8b [20].

(d) Formic acid

Adsorption of formic acid on MgO(111) yielded intense peaks in UPS difference spectrum in Fig.3-9a. They are assigned to formate, compared with a reference spectrum of formate on Cu film [21]. Note that the amount of adsorbed formate was same on the (100) and the faceted (111) surfaces in Table 3-1.

(e) Methylformate

Three peaks were observed in UPS difference spectrum in Fig.3-10a upon methylformate exposure on MgO(111). Molecular methylformate gives different features as shown in Fig.3-10b [19]. The observed signal is interpreted as a superposition of emissions from methoxide (Fig.3-7a) and formate (Fig.3-9a). This indicates that the MgO surfaces dissociate methylformate into formate and methoxyl group.

Two emissions of C(1s) are listed in Table 3-1 at 286.5 and 289.4 eV. The former corresponds to methoxyl carbon, while the latter is assigned to the carbon in formate. The latter value is higher by 0.5 eV than the binding energy observed upon adsorption of formic acid. The shift reflects difference of formate species in configuration at surface. Formate originated from $HCOOCH_3$ should employ oxygen anion of substrate. A part of formates decomposed at 298 K, because the density of formate carbon was smaller than that of the methoxyl carbon.

3.5. Discussion

MgO(100) surface is a stable surface, whereas MgO(111)

surface cannot maintain the ideal structure. The split and streaks in non-radial directions observed in LEED indicate trigonal facets composed of (100), (010) and (001) microplanes on the faceted (111) surface, as illustrated in Fig.3-11. The Dimension of facets, I, was estimated about 2 nm on the basis of the spot diameters in LEED. There is no evidence for ideal (111) plane resident on the annealed (111) wafer in LEED nor UPS results.

Henrich reported that a MgO(111) surface was reconstructed to give microfacets with several nm across by Ar^+ bombardment at room temperature. Subsequent annealing to 900-1400 K resulted in thorough faceting up to 1 μm across, accompanied with a drastic change in LEED [11]. Such a great facet, however, could not be observed even with annealing at 1000 K for 2 min in the present study. The difference might be ascribed to quality of bulk crystals employed.

Figure 3-3 demonstrates that Na adatoms are initially adsorbed on small amounts of defects over the (100) wafer; multilayered islands then grow around the incipient nuclei. This suggests that ideal (100) plane cannot adsorb Na atom at 300 K, though a XPS study reported Na_2O-like species on a Na-deposited CaO(100) surface [22]. The density of the nuclei was estimated to be 1×10^{18} m^{-2} on the density of Na at the break in Fig.3-3a. On the other hand, atomic layer growth and subsequent nucleation are suggested on the faceted (111) surface in Fig.3-3. The completed first layer yields surface plasmon losses as shown in Fig.3-5b. Bulk plasmon losses in Fig.3-5c reflects three-dimensional nucleation of metallic Na.

There are two possible adsorption sites for Na adatoms in the atomic layer on the faceted (111) surface. One is coordinatively unsaturated edge-site; the other is multicentered valley-site. The edge-sites with multiple coordination vacancy is plausible for Na adsorption, having most different environment in local coordination from inert (100) plane. If regular microfacets of 2 nm across cover whole surface, density of cation-anion pairs on edge site is 2×10^{18} m^{-2}. Surface density of the first layer of Na was 5×10^{18} m^{-2}. Hence two Na adatoms

are bonded per edge site.

The similar curves of Fig.3-4a and 3-4b suggest a strong interaction of Na adatoms with oxygen anions on the faceted (111) substrate. The observed shift in Na(1s) binding energy also indicates some transfer of electron from Na adatoms to the substrate. Those behaviour must result from local bonds at adsorption site. MgO has a large negative electron affinity and the conduction band consists of Mg orbitals. 3s electron of Na cannot directly hop into the conduction band. Mg(1s) nor Mg(2s) levels was not affected by Na adatoms at all.

Water, methanol, methylformate and carbon dioxide were dissociatively or reactively adsorbed on both the MgO surfaces with UPS spectra in Figs.3-6, 3-7, 3-8 and 3-10. On the faceted (111) surface the amount of adsorbed water, methanol or methylformate are $2\text{-}3\times10^{18}$ m^{-2}. They are almost the same as the calculated surface density of reactive Mg-O pairs at edge of microfacets of 2 nm across. In addition, a theoretical study for edge structure [8] found that an unoccupied state mainly composed of Mg(3s) and Mg(3p) orbitals shifts into the band gap region; it is expected to interact with the orbitals of adsorbed molecules. Hence it is suggested that the dissociative adsorption of these molecules takes place preferentially on coordinatively unsaturated Mg-O pairs on edge of facets. Similarly reactive adsorption of CO_2 forming carbonate occurs on basic oxygen anion at edge site. Fukuda et al. [23] reported carbonate formation with CO_2 exposure on MgO film. There can be dense population of unsaturated oxygen sites on oxide film.

The coverages of the four reactants were below 1×10^{18} m^{-2} on the (100) wafer. It is thus likely that these molecules are adsorbed on the residual defects. In contrast, (100) plane adsorbs formic acid to saturate formate. No difference between the (100) and the faceted (111) wafers was observed in adsorption of formic acid. Formic acid alone has a large affinity with metal oxide to form formate.

3.6. Conclusions

An annealed MgO(111) surface facets into trigonal pyramids of (100), (010) and (001) microplanes. The dimension of the facets is ca.2 nm upon annealing to 1000 K. Atomic Na is selectively adsorbed on coordinatively unsaturated edge-sites on the faceted (111) surface at 300 K interacting with oxygen anions, while an annealed MgO(100) gives negligible interaction with Na adatoms. Water, Methanol and methylformate are dissociatively adsorbed on the faceted (111) surface. Carbon dioxide form carbonate on the faceted surface. Formic acid is dissociated even on (100) surface.

3.7. References

1. K.Miyahara, Y.Murata, I.Toyoshima, Y.Tanaka and T.Yokoyama, J.Catal.68(1981)186.
2. M.Boudart, A.Delbouille, E.G.Derouane, V.Indovina and A.B.Walters, J.Am.Chem.Soc.94(1973)6622.
3. P.Mars, J.J.F.Scholten and P.Zwietering, Adv.Catal.14(1963)35.
4. J.Kijenski and S.Marinowski, Bull.Acad.Polonaise Sci.25(1977)428.
5. D.J.Driscoll, W.Martir, J.X.Wang and J.H.Lunsford, J.Am.Chem.Soc.107(1985)58.
6. T.Moriyama, N.Takasaki, E.Iwamatsu and K.Aika, Chem.Lett.(1986)1165.
7. S.Coluccia and A.J.Tench, Proc.7th.Intern.Congr.Catal.,Kodansha/Elsevier(1981),B1154.
8. M.Tsukada, H.Adachi and C.Satoko, Progr.Surf.Sci.9(1979)143.
9 C.Satoko, M.Tsukada and H.Adachi, J.Phys.Soc.Jpn.45(1978)1333.
10. M.Tsukada and T.Hoshino, J.Phys.Soc.Jpn.51(1982)2562.
11. V.E.Henrich, Surf.Sci.57(1976)385.
12. D.A.Huchital and R.T.Mckeon, Appl.Phys.Lett.20(1972)158.
13. G.Ertl and J.Küppers, in: Low Energy Electrons and Surface Chemistry, Verlag Chemie, Weinheim(1974), p.155.
14. J.C.Fuggle, Surf.Sci.69(1977)581.
15. H.Daimon, A.Saito and Y.Murata, Activity Report of Synchrotron Radiation Laboratory, Institute of Solid State Physics, The University of Tokyo, (1980)62.
16. A.Barrie and F.J.Street, J.Electrn.Spectrosc.Related Phenomena 7(1975)1.
17. J.A.Conner, M.Considine, I.H.Hiller and D.Briggs, J.Electrn.Spectrosc.Related Phenomena 12(1977)143.
18. J.C.Fuggle, L.M.Watson, D.J.Fabian and S.Affrossman, Surf.Sci.49(1975)61.
19. B.A.Sexton, A.E.Hughes and N.R.Avery, Surf.Sci.155(1985)366.

20. J.A.Conner, M.Considine and I.H.Hiller, J.Chem.Soc.Faraday Trans.II 74(1978)1285.
21. R.W.Joyner and M.W.Roberts, Proc.R.Soc.Lond.A350(1976)107.
22. Y.C.Lee, P.A.Montano and J.M.Cook, Surf.Sci.143(1984)423.
23. Y.Fukuda and I.Toyoshima, Surf.Sci.158(1985)482.

Table 3-1. Binding energy in XPS and estimated surface density of target atoms.

reactant	MgO wafer	B.E. / eV O(1s)	B.E. / eV C(1s)	surface density[b] /10^{18} m^{-2} σ_O	surface density[b] /10^{18} m^{-2} σ_C
none [a]	(100)	529.9			
	(111)	529.9			
H_2O	(100)	532.3		1.5	
	(111)	532.3		4	
CH_3OH	(100)	532.3	286.4	1.5	0.7
	(111)	532.4	286.4	5	3
CO_2	(100)	532.6	290.0	2	0.3
	(111)	532.6	290.1	5	1
HCOOH	(100)	532.4	289.0	11	3
	(111)	532.3	288.8	11	3
$HCOOCH_3$	(100)	532.9	286.3	1.5	0.5
			289.5		0.3
	(111)	532.7	286.5	7	3
			289.4		2

[a] lattice oxygen.

[b] $\pm 0.7 \times 10^{18}$ m^{-2}.

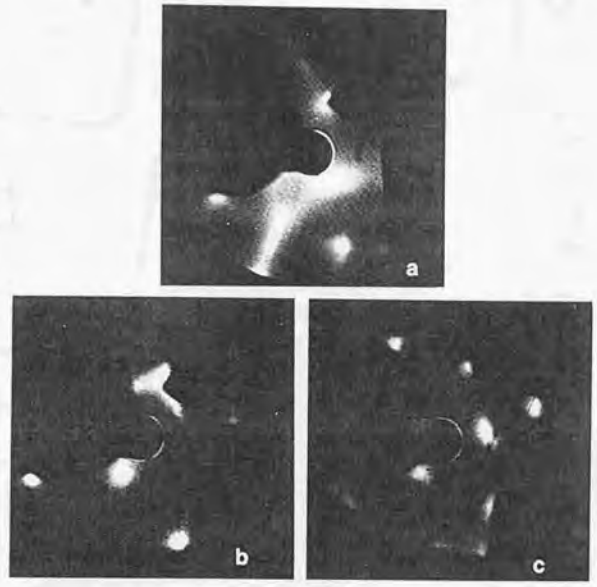

Fig.3-1. LEED patterns on an annealed MgO(111) surface with (a) Ep=95 eV, (b) Ep=100 eV and (c) Ep=105 eV.

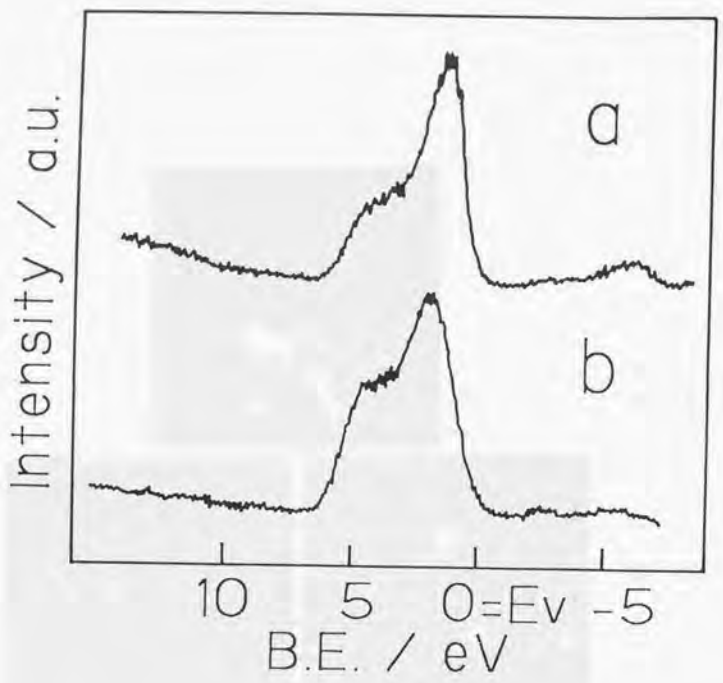

Fig.3-2. HeII UPS spectra on (a) a MgO(100) surface and (b) a faceted MgO(111) surface.

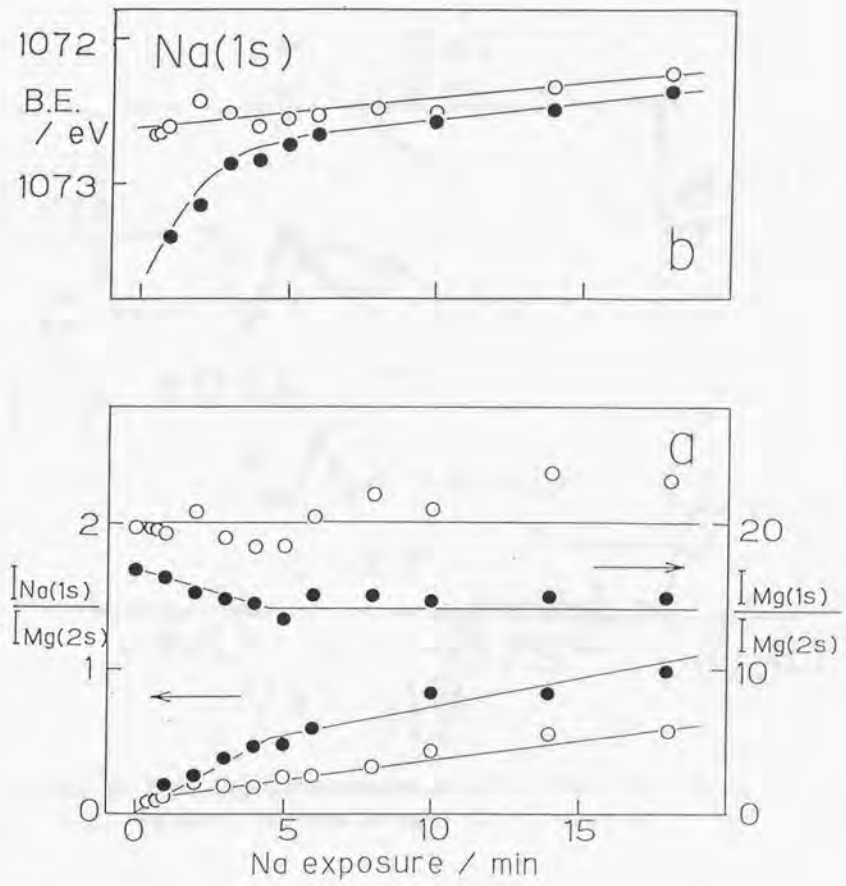

Fig.3-3. Na(1s) and Mg(1s) emissions with Na exposure.
(a):normalized intensity of Na(1s) and Mg(1s) emissions;
(b):binding energy of Na(1s) level
where, ○:MgO(100), ●:MgO(111).

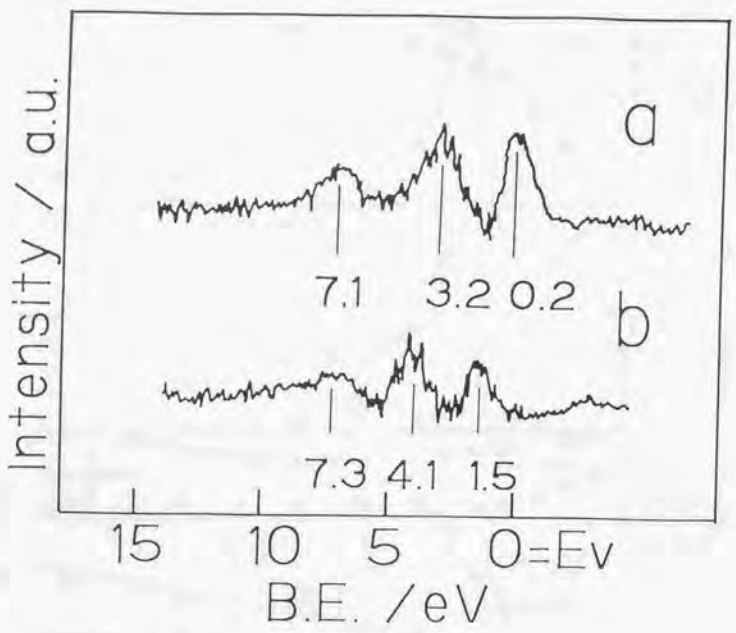

Fig.3-4. HeII UPS difference spectra on (a) 10^3 L O_2 exposed Na/MgO(100); and (b) Na/MgO(111) without oxygen exposure.

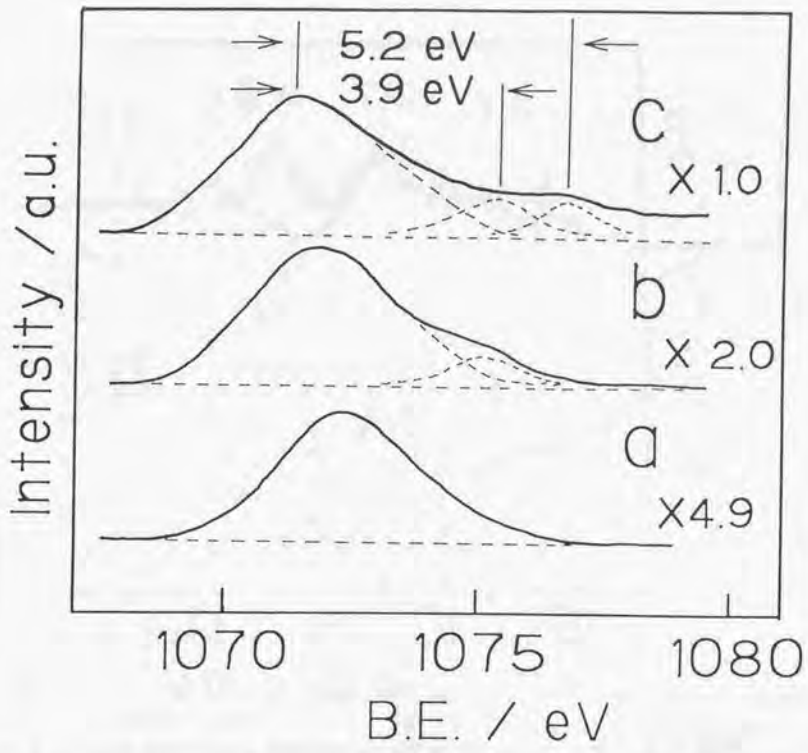

Fig.3-5. Na(1s) XPS spectra of Na adatoms deposited on a faceted MgO(111) surface for (a) 1 min, (b) 5 min and (c) 18 min.

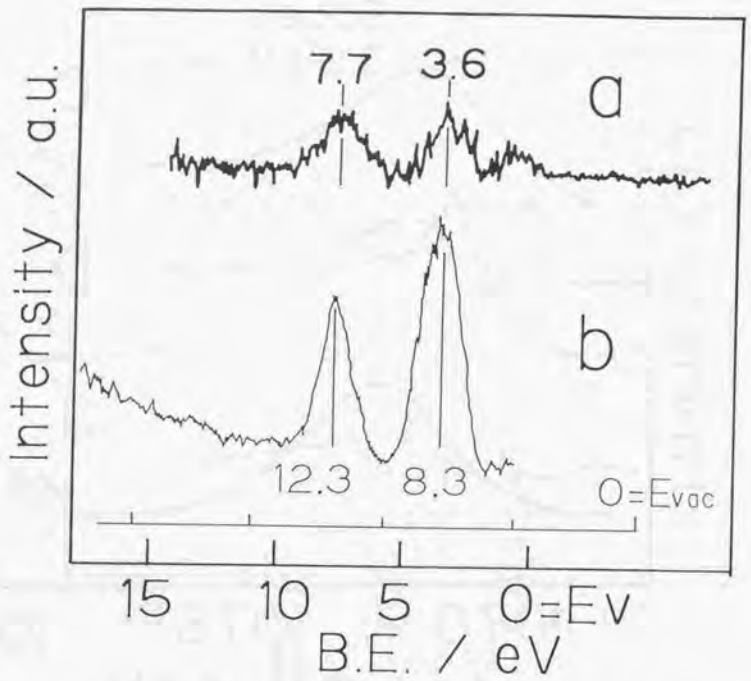

Fig.3-6. (a) HeII UPS difference spectrum for 10^3 L H_2O-expos faceted MgO(111) and (b) HeII UPS of solid NaOH [17] where binding energy is referred to the vacuum level E

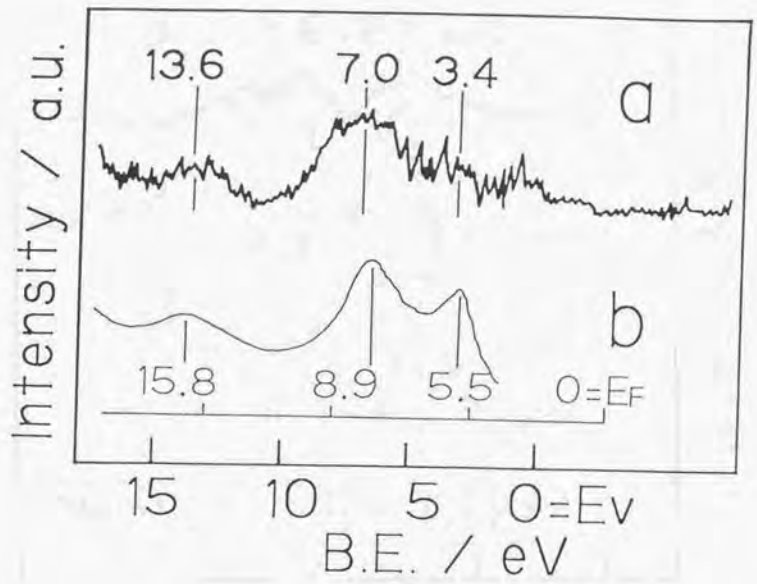

Fig.3-7. (a) HeII UPS difference spectrum for 10^3 L CH_3OH-exposed faceted MgO(111) and (b) HeII UPS from methoxide on Cu(110) [19] where binding energy is referred to the Fermi level E_F.

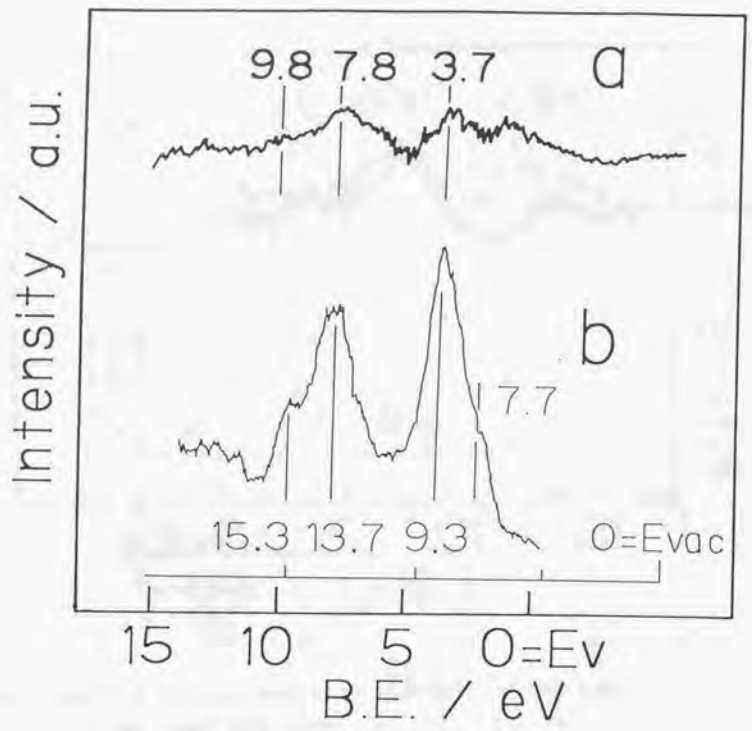

Fig.3-8. (a) HeII UPS difference spectrum for 10^3 L CO_2-exposed faceted MgO(111) and (b) HeII UPS of solid K_2CO_3 [20] where binding energy is referred to the vacuum level E_{vac}.

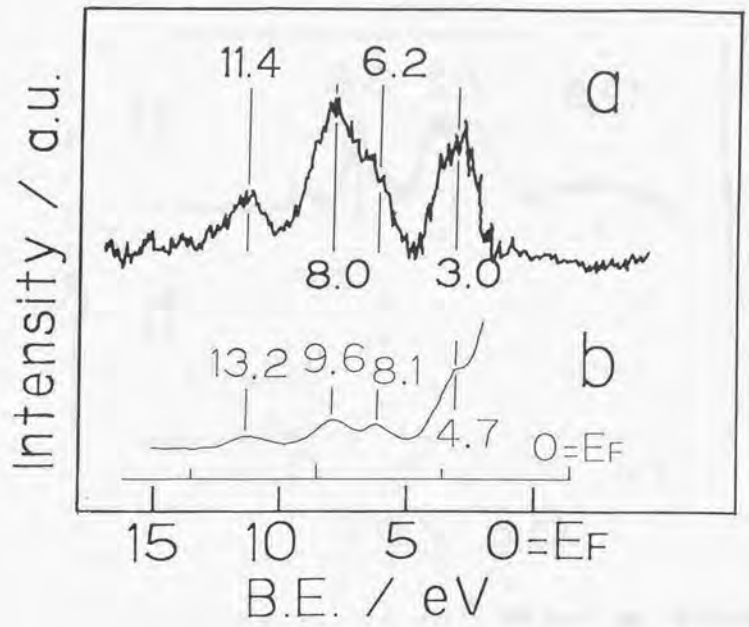

Fig.3-9. (a) HeII UPS difference spectrum for 10^3 L HCOOH-exposed faceted MgO(111) and (b) HeII UPS of formate adsorbed on a Cu film [21] where binding energy is referred to the Fermi level E_F.

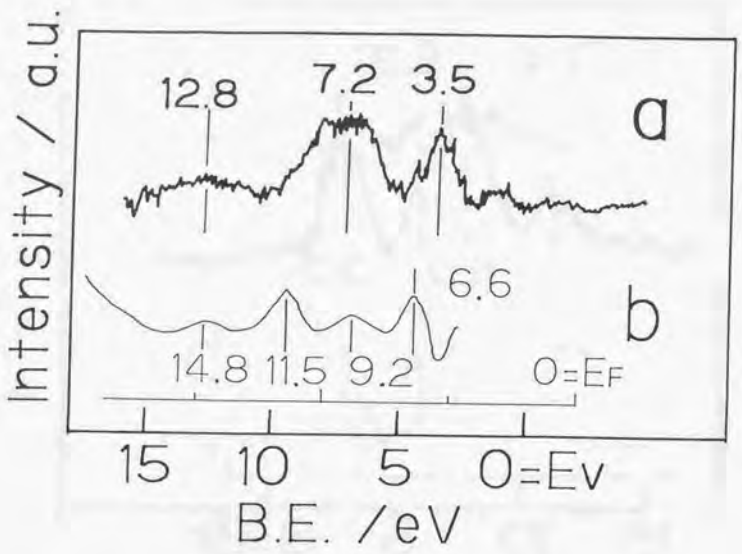

Fig.3-10. (a) HeII UPS difference spectrum for 10^3 L $HCOOCH_3$-exposed faceted MgO(111) and (b) HeII UPS of molecularly adsorbed $HCOOCH_3$ on Cu(110) [19] where binding energy is referred to the Fermi level E_F.

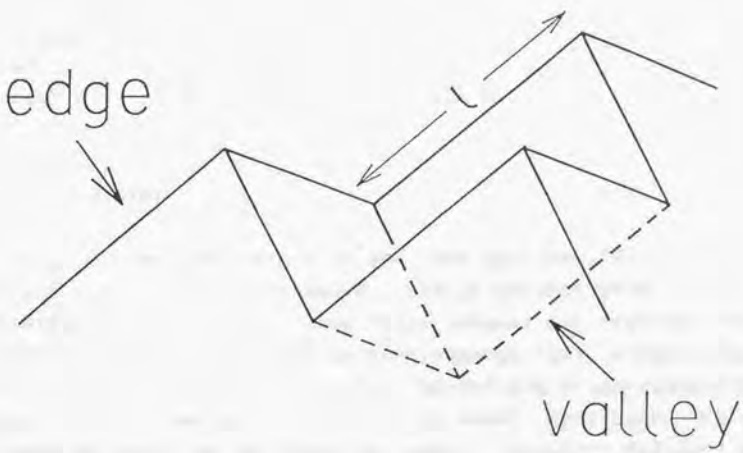

Fig.3-11. A Model for faceted MgO (111) surface with edge dimension of 1.

Chapter 4

Adsorption of CH_3OH and SO_2 on TiO_2(110) and stepped TiO_2(441) surfaces

4.1. Abstract

TiO_2(110) and TiO_2(441) surfaces are compared in chemisorption of CH_3OH and SO_2 at 298 K by means of XPS, UPS and LEED. (441) surface has regular steps and indexed as [3(110)x(111)]. Small amount Ti^{3+} species on step sites pin the Fermi level. The work function is smaller by 0.7 eV than that on (110) surface due to the pinned Fermi level. CH_3OH is molecularly adsorbed on both the surfaces. SO_2 is adsorbed on (441) forming SO_3^{2-} and also oxidized Ti^{3+} at step sites to form S^{2-}, while only SO_3^{2-} was detected on (110) surface.

4.2. Introduction

It is expected that roughness or defects on oxide surfaces play an important role in adsorption and catalysis, because the open surface structures with multiple coordination vacancy generate the surface states which expand to band gap region [1]. In fact, polycrystalline powders of MgO are active catalysts for the isomerization reaction of 1,3-butadiene,

whereas a (100) plane of MgO is catalytically inert [2].

Here, two kinds surface structure of TiO_2 (rutile), a more acidic oxide, are prepared: (110) surface without step structure, and (441) surface with regular steps. Chemisorption of CH_3OH and SO_2 is compared on the surfaces with XPS, UPS and LEED. CH_3OH is a fundamental oxygenated compound in C_1-chemistry [3]. SO_2 has strong acidic and oxidative character to be expected certain interaction with metal oxide.

Surface structure and electronic states were related to chemisorption properties for O_2, H_2 and H_2O on TiO_2 by means of UPS and ELS [4-8]. Twin-Ti^{3+} (d^1) ensemble was reported to dissociate water [4,7]. A more recent study on $Ti_2O_3(10\bar{1}2)$ showed that an isolated Ti^{3+} cation in d^1 state is inadequate for the dissociation of water. Geometry of cation-cation pair is important [4,9]. Effect of step structure is thus interesting on TiO_2.

4.3. Experimental

The experiments were carried out in an ultra high vacuum chamber (VG-ESCALAB) which has facilities for XPS, UPS and LEED measurements with a base pressure of 6×10^{-11} Torr (1 Torr=133.3 Pa). Photoelectron spectrum was taken with emission along the [110] direction. Binding energy in XPS excited by Mg-Kα radiation was referred to an internal reference, O(1s) level of 530.3 eV for lattice oxygen anion, which was calibrated after Au(4f7/2) level of 83.8 eV in gold film deposited on crystals. Surface density of adsorbed species was estimated on the intensity of XPS peak, considering relative cross sections and escape depths. The work function was measured from cut-off in HeI UPS.

A TiO_2 single crystal rod was obtained from Murakami Engineering Co. A diamond wheel saw cut out two wafers oriented by the Laue method. The surface normal of (441) sample was tilted by 16.2° from the [110] axis to the [001] direction. They were mechanically polished over 0.05 mm Al_2O_3 powder and then chemically etched in 5N NaOH at 323 K for

30 min, followed by wash with distilled water. Subsequently, they were annealed in air at 1073 K for 5 h before cleaning under vacuum. Argon sputtering at 4 KeV and 15 μA for 6 min. and annealing with electron bombardment to 900 K were repeated in the chamber.

Gases of research grade were purified by repeated trap-thaw cycles. They were introduced onto crystal through a capillary doser at 298 K. Pressure of exposed reactants was estimated ca.10^{-6} Torr on sample surface.

4.4. Results

4.4.1. Clean surfaces

The sputter-anneal cycles gave deep blue crystals because they were slightly reduced. The resistivity was about 2 Ωm. While the annealed (110) surface exhibited a sharp (1x1) rectangular structure in LEED, the (441) surface showed a split pattern as shown in Fig.4-1. Figure 4-2 shows the corresponding unit cell in real space. All spots moved toward the [110] direction repeating split, when the primary energy E_p was increased. The splitting behavior demonstrates a regular step structure with (110) terraces. A kinetic theory of diffraction [10] formulates the characteristic energy of splitting E_c for the (0,0) spot with the step height d.

$$(E_c+U_i)/eV=0.376d^{-2}s^2nm^2 \quad (1)$$

where U_i is inner potential and s has integer or half integer values corresponding to single or double spot, respectively. The observed E_c are plotted with s^2 in Fig.4-3. A step height of 33±1 pm fits the plot.

Figure 4-4 shows HeI UPS on the (110) and (441) surfaces. The spectrum of the (110) surface has a pronounced peak at 5.4 eV and small shoulders at 3.7, 6.6 and 7.5 eV below the Fermi level E_F. The emission near E_F is negligible. They are in agreement with previous studies [5,11,12]. The (441) surface gave a

broader feature: peaks at 4.0, 5.9, and 8.4 eV. In addition there is a small peak at 1.0 eV just below the Fermi level. The work function on the (110) surface was 5.3±0.1 eV, which is consistent with the reported value [11]. The (441) surface gave a smaller value of 4.6±0.1 eV.

4.4.2. Gas adsorption

(a) CH_3OH

10^3 L (1 L=10^{-6} Torr.s) of CH_3OH was admitted to the two surfaces at 298 K. HeI UPS difference spectra in Fig.4-5 have a similar four-peak feature at 4.5, 6.1, 7.6 and 9.7-10.6 eV. The change in work function $\Delta\phi$ is listed in Table 4-1 together with the results in XPS. The surface density of adsorbed species is almost the same, but $\Delta\phi$ is smaller by 0.4 eV on the (441) surface. The background in LEED gained intensity without new spot upon the methanol exposure.

(b) SO_2

The crystals were exposed to 10^3 L of SO_2 at 298 K. HeI UPS difference spectra in Fig.4-6 exhibited four peaks at 4.0-4.5, 6.2, 7.8 and 10.8 eV. Two peaks were observed in S(2p) region on the (441) surface, while only one peak was detected on the (110) surface as shown in Table 4-2.

4.5. Discussion

4.5.1. Structure and electronic states on TiO_2(110) and (441) surfaces

It is well established that TiO_2(110) has a stable but highly anisotropic surface structure as illustrated in Fig.4-7a [4]. There are two kinds of Ti cations on (110) plane. A half of Ti cations are located in an optimum six-fold coordination and the other half have a five-fold coordination. Similarly $^2/_3$ of surface oxygen anions is coordinated by three Ti cations as in the bulk, while the rest have only two neighboring cations.

Assuming this geometry, Tsukada et al. [1.13] performed a DV-Xα calculation and found an empty surface state localized on a five-fold coordinated Ti cation and a filled surface state on a two-fold coordinated O atom; they are labeled as A' and C', respectively in Fig.4-4c. The latter state is seen at 3.7 eV in Fig.4-4a.

A model for (441) surface is proposed in Fig.4-7b, considering surface stoichiometry. The regular step structure is indexed as [3(110)x(111)]. Four-fold coordinated Ti cation is avoided, because unfavorable Ti sites with four-fold coordination results in faceting on TiO_2(001) surface [14]. The model in Fig.4-7b has an oblique unit cell, two vectors of which are 649 and 1270 pm long with the crossing angle of 74.7°. The step height of 325 pm corresponds to the half of the periodicity in the [110] direction. They are in good agreement with the observed structure in Fig.4-2. Generally step structure leads to reduced coordination. There two more five-fold coordinated Ti cations are introduced per unit cell on the model of Fig.4-7b, as compared with (110) plane of Fig.4-7a.

Large Madelung potential avoids coordinative unsaturation to bring facets on MgO, as demonstrated on faceted (111) surface in Chapter 3. In contrast, the (441) stepped surface was stable after repeated cycles of Ar^+ bombardment and annealing. A ESDIAD (electron stimulated desorption ion angular distribution) study on rutile proposed some models of step structure for intermediate structures during thermal annealing process [15]. The stability results from the fact that (111) step site can avoid unfavorable four-fold cation without reconstruction.

HeI UPS spectrum on (441) surface in Fig.4-4b exhibited valence bands similar to those of (110) surface. But all the features shifted to higher binding energy by 0.7 eV on (441) surface. The pinned Fermi level and a resultant downward band bending cause the shift. surface Ti^{3+} species, which results in a downward band bending toward the surface. The small peak at 1.0 eV observed in Fig.4-4b is assigned to Ti^{3+} species [11]. The occupied d states pin the Fermi level. A rough estimation on the amount of the Ti^{3+} species is possible on the intensity. The

intensity of the d emission was 0.5% of that of O(2p) valence bands. Equal matrix elements for O(2p) and Ti(3d) emissions were proposed on $Ti_2O_3(10\bar{1}2)$ [16]. If angular dependence of emission is averaged out, the observed intensity gives a density of 1×10^{18} m^{-2} in Ti^{3+}. It corresponds to 0.8 Ti^{3+} cation in the oblique unit cell.

There are two possible sources for the Ti^{3+} species; one is an intrinsic property of the step structure. Wandelt applied photoelectron spectroscopy of adsorbed xenon (PAX) on Pt(111) surface [17] and revealed that step site has a local surface potential lower by 1.0 eV than that of terrace. One can expect a similar effect of step on rutile. The other possibility is oxygen vacancy induced on the steps. Oxygen anions at the steps have poorer coordination than at (110) terrace, and would be stripped more easily in the cleaning processes.

4.5.2. Adsorption of CH_3OH

The UPS spectra in Fig.4-5 indicate that CH_3OH is molecularly adsorbed on (110) and (441) surfaces at 298 K, compared with molecular adsorbate on Cu(110) at 150 K [18]. The peaks at 6.1 and 7.6 eV are assigned to 2a" and 7a' orbitals, respectively. They exhibit a relative shift of 0.5 eV to higher binding energy compared with a free molecule. The relative shift demonstrates a bonding configuration of CH_3OH to a five-fold coordinated Ti cation via a lone pair of the oxygen atom [18]. The binding energy in C(1s) and O(1s) also supports molecular adsorption. The reported values on Cu(110) are in agreement on Table 4-1 [18]. Molecularly adsorbed CH_3OH is stable on ZnO($10\bar{1}0$) up to 300 K [19]. Low indexed planes on metal oxide are often less active than surfaces of transition metal due to band gaps.

Dissociated species was not detected on (441) surface. The step structure with Ti^{3+} species cannot dissociate CH_3OH, though edge sites on faceted MgO(111) dissociate CH_3OH as shown in Chapter 3. This is consistent with the fact that Ti^{3+} (d^1) state on $Ti_2O_3(10\bar{1}2)$ surface is inadequate for the dissociation of water [9].

The change in work function in Table 4-1 results from an upward dipole moment of adsorbed methanol. A free CH_3OH has a large dipole of 1.69 Debye. When the dipole axis is oriented normal to surface with a density of 3×10^{19} m^{-2}, the work function decreases by 1.9 eV. The observed $\Delta\phi$ on the (110) surface, -1.1 eV, is an acceptable value. (441) surface gave a smaller decrease in work function, though the surface density of the adsorbates was same. This demonstrates that CH_3OH adsorbed on (111) step sites gives a smaller dipole than on (110) terrace.

4.5.3. Adsorption of SO_2

S(2p) binding energy in Table 4-2 shows that SO_2 is adsorbed to form SO_3^{2-} on TiO_2(110), comparing with the values in standard materials [20]. HeI UPS difference spectrum in Fig.4-6a has four peaks at 4.5, 6.2, 7.8 and 10.8 eV. They are consistent with valence spectrum of Li_2SO_3 in Mg-Kα XPS [21], considering the difference in resolution. SO_2 is adsorbed on a CaO(100) surface to form SO_4^{2-} [22]. The reactivity to SO_2 is related to acid-base property of the oxides. More basic oxygen anions on CaO coordinate to acidic SO_2 to form SO_4^{2-} more easily.

Two S(2p) levels were observed on (441) at 167.2 and 162.1 eV. They are assigned into SO_3^{2-} and S^{2-} species, respectively. Sulfur dioxide, a Ti^{3+} scavenger, oxidizes $Ti_2O_3(10\bar{1}2)$ forming TiO_2 and TiS_2 [23]. Exposure to SO_2 swept out Ti(3d) emission at 1.0 eV in Fig.4-6b, together with a four-peak feature identical to Fig.4-6a. Consequently, the resulted S^{2-} species are located on the step sites.

4.6. Conclusion

An TiO_2(441) surface gives a stable regular step structure indexed as [3(110)x(111)]. Work function is smaller by 0.7 eV on the (441) surface than that on a TiO_2(110) due to the pinned Fermi level and a downward band bending toward the surface. A small amount of Ti^{3+} species, less than 1×10^{18} m^{-2}, pin the Fermi level.

CH_3OH is molecularly adsorbed on TiO_2(441) and (110) surfaces at 298 K. Step sites with Ti^{3+} cations are inadequate to dissociate methanol on the (441) surface. The (110) surface adsorbs sulfur dioxide to form SO_3^{2-}, while SO_2 is dissociatively adsorbed on the (441) surface oxidizing Ti^{3+} species, in addition to sulfite formation.

4.7. References

1. M.Tsukada, H.Adachi and C.Satoko, Progr.Surf.Sci.9(1979)143.
2. K.Miyahara, Y.Murata, I.Toyoshima, Y.Tanaka and T.Yokoyama, J. Catal.68(1981)186.
3. R.G.Harman, K.Klier, G.W.Simmons, B.D.Finn, J.B.Gulko and T.P.Kobylinski, J.Catal.56(1979)407.
4. V.E.Henrich, Progr.Surf.Sci.14(1983)175.
5. V.E.Henrich, Progr.Surf.Sci.9(1979)143.
6. W.Göpel, Progr.Surf.Sci.20(1985)9.
7. G.Heiland and H.Lüth, in: The Chemical Physics of Solid Surfaces and Heterogeneous Catalysis,vol.3, Elsevier,Amsterdam(1984),chap.4.
8. W.J.Lo, Y.W.Chung and G.A.Somorjai,Surf.Sci.71(1978)199.
9. R.L.Kurtz and V.E.Henrich, Phys.Rev.B26(1982)6682.
10. G.Ertl and J.Küppers, in: Low Energy Electrons and Surface Chemistry, Verlag Chemie,Weinheim(1974),p.169.
11. Y.W.Chung, W.J.Lo and G.A.Somorjai, Surf.Sci.64(1977)588.
12. R.H.Tait and R.V.Kasowski, Phys.Rev.B20(1979)5178.
13. M.Tsukada, C.Satoko and H.Adachi, J.Phys.Soc.Jpn.47(1979)1610.
14. L.E.Firment, Surf.Sci.116(1982)205
15. R.L.Kurtz, Surf.Sci.177(1986)526.
16. R.L.Kurtz and V.E.Henrich, Phys.Rev.B25(1982)3563.
17. K.Wandelt, J.Vac.Sci.Technol.A2(1984)802.
18. M.Bowker and R.J.Madix, Surf.Sci.95(1980)190.
19. G.W.Rubloff, H.Lüth and W.D.Grobman, Chem.Phys.Lett.39(1976)493.
20. B.J.Lindberg, K.Hamrin, U.Gelius and K.Siegbahn, Phys.Scr.1(1970)286.
21. A.Calabrese and R.G.Hayes, J.Electrn.Spectrosc.Related Phenomena 12(1977)143.
22. C.D.Stinespring and J.M.Cook, J.Electrn.Spectrosc.Related Phenomena 32(1983)113.
23. K.E.Smith and V.E.Henrich, Phys.Rev.B32(1985)5384.

Table 4-1. XPS and $\Delta\phi$ results for CH_3OH adsorption.

	B.E./eV		surface density[a] /10^{18} m^{-2}		$\Delta\phi$ /eV
	C(1s)	O(1s)	C(1s)	O(1s)	
CH_3OH/TiO_2(110)	286.4	532.3	3	3	-1.1
CH_3OH/TiO_2(441)	286.2	532.2	3	4	-0.7

a) $\pm 1 \times 10^{18}$ m^{-2}

Table 4-2. XPS and $\Delta\phi$ results for SO_2 adsorption.

	B.E./eV		surface density[a] /10^{18} m^{-2}		$\Delta\phi$ /eV
	S(2p)	O(1s)	S(2p)	O(1s)	
SO_2 /TiO_2(110)	167.0	532.4	1	1	+0.3
SO_2 /TiO_2(441)	167.2 162.1	532.7	1 0.2	1	+0.4
Na_2S [b]	162.0	-	-	-	-
Na_2SO_3 [b]	166.7	531.9	-	-	-
Na_2SO_4 [b]	168.9	532.3	-	-	-

a) $\pm 1 \times 10^{18}$ m^{-2}

b) standard materials [20].

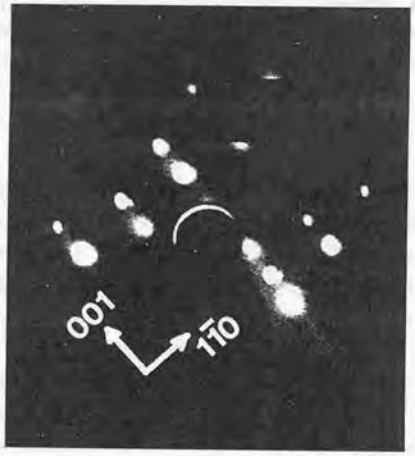

Fig.4-1. LEED pattern on an annealed TiO_2(441) surface with E_p=60 eV.

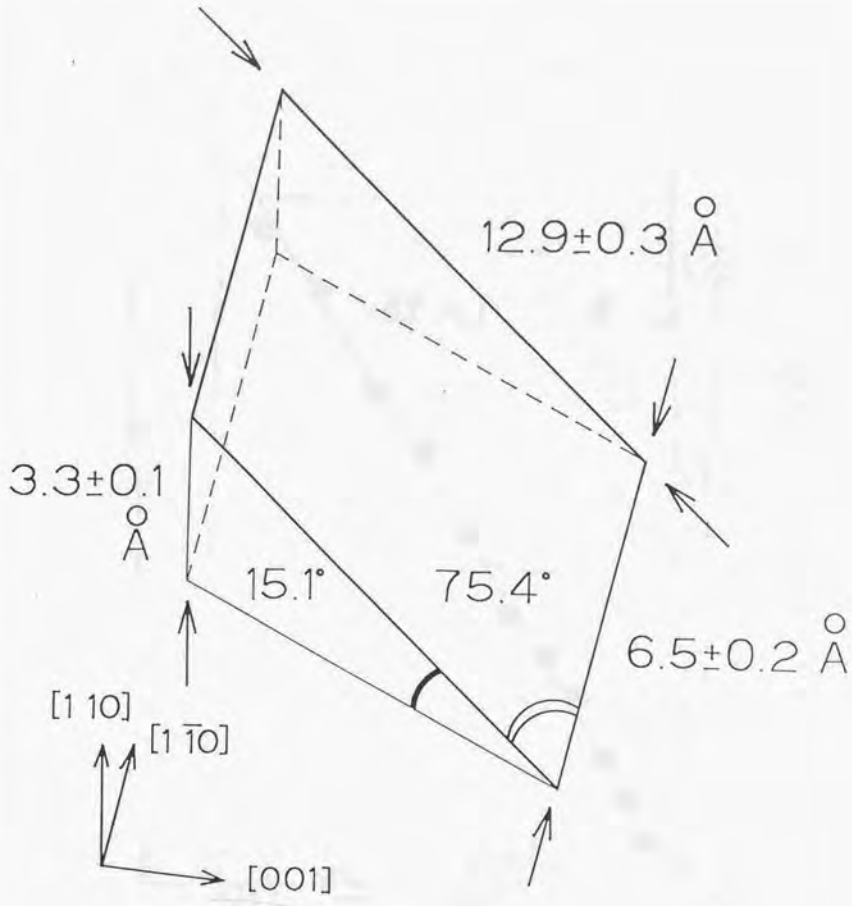

Fig.4-2. A schematic drawing of the unit cell observed on TiO_2(441) surface.

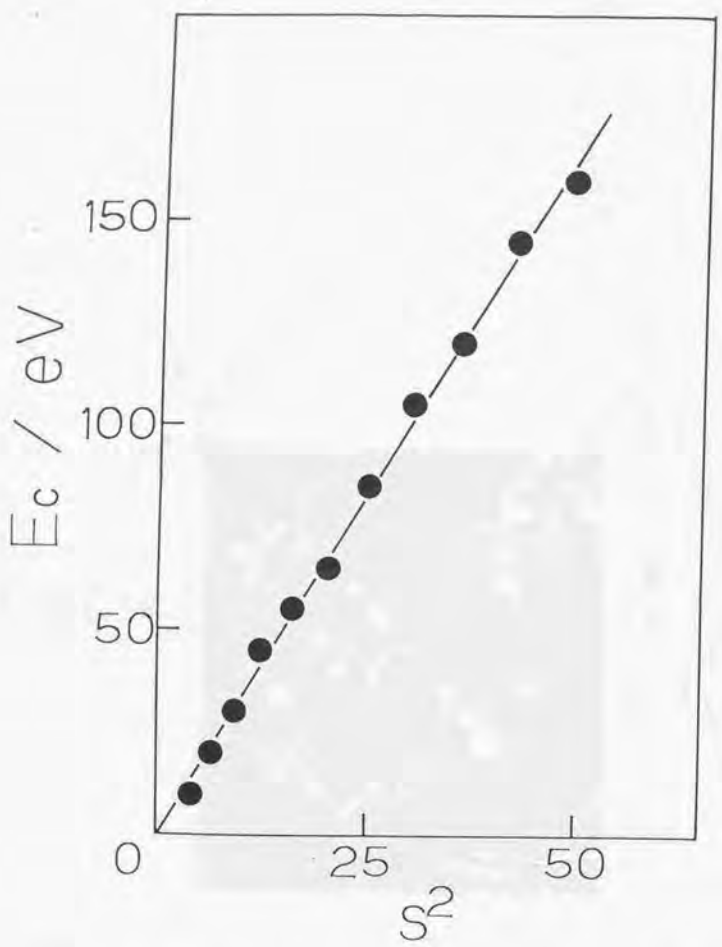

Fig.4-3. The characteristic energy E_c for splitting on stepped TiO_2(441) surface.

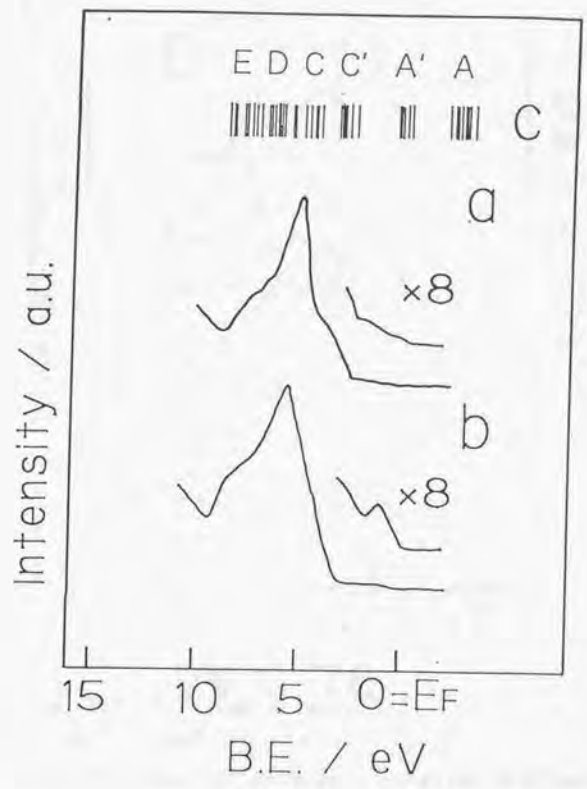

Fig.4-4. HeI UPS spectra on (a) TiO_2(110) and (b) TiO_2(441) surfaces. Calculated levels for a cluster representing TiO_2(110) surface are also shown in (c) [13].

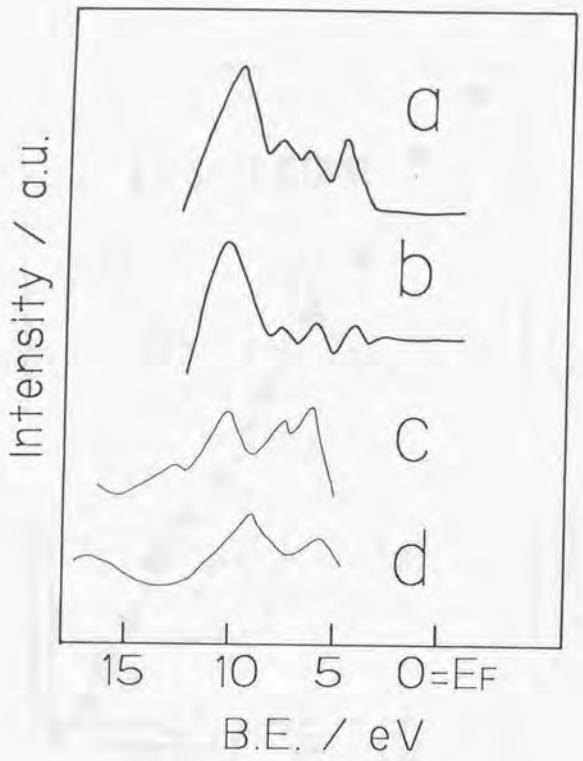

Fig.4-5. HeI UPS difference spectra for 10^3 L CH_3OH-exposed (a) TiO_2(110) and (b) TiO_2(441) surfaces. HeII UPS spectra of CH_3OH adsorbed on Cu(110) at (c) 150 K and (d) 240 K are also shown, which are assigned to molecular and dissociated species, respectively [18].

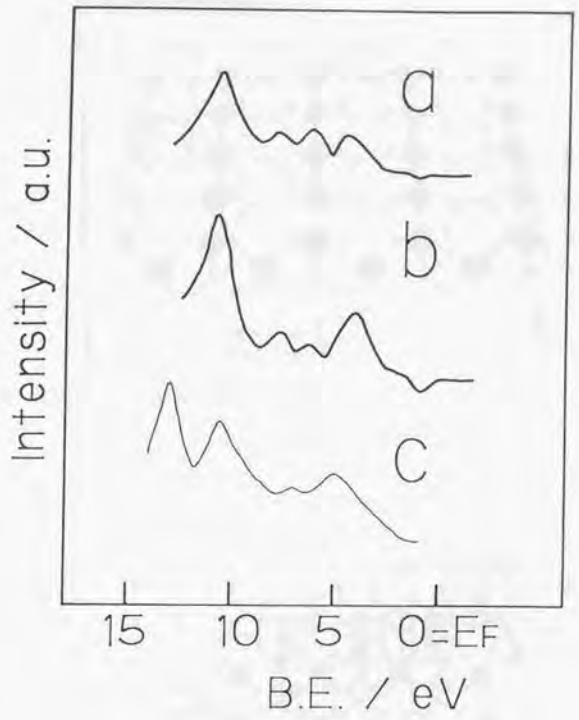

Fig.4-6. HeI UPS difference spectra for 10^3 L SO_2-exposed (a) TiO_2(110) and (b) TiO_2(441) surfaces, together with (c) valence states of Li_2SO_3 in Mg-Kα XPS [21].

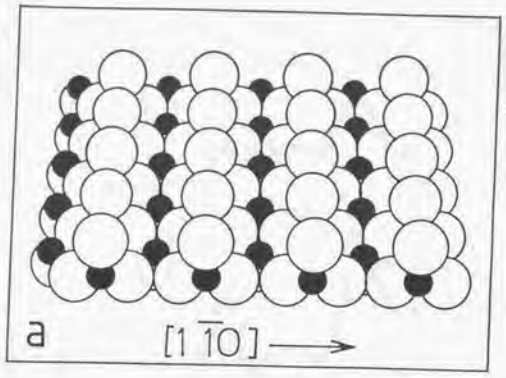

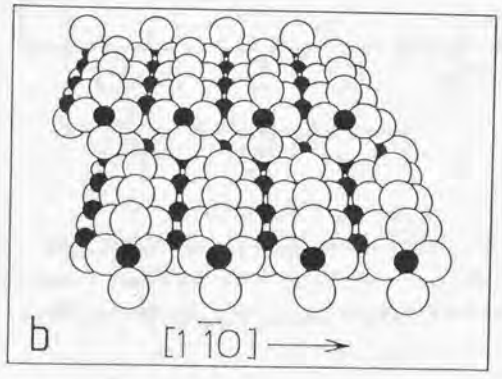

Fig.4-7. Models for (a) TiO_2(110) and (b) stepped TiO_2(441) surfaces; filled and open circles represent Ti^{4+} and O^{2-} atoms, respectively.

Chapter 5

Adsorption and catalytic decomposition of formic acid on TiO_2(110) surface

5.1. Abstract

Adsorption and catalytic decomposition reaction of formic acid (DCOOD) is examined on TiO_2(110) surface. The kinetic behavior in catalysis is recorded under DCOOD atmosphere of 10^{-8}-10^{-5} Torr at 500-800 K, while TDS, LEED, AES, XPS and UPS characterize adsorbate and reaction under vacuum. TiO_2(110) dissociates formic acid at 250 K to form a (2x1) ordered overlayer with 0.5 ML of formate and hydroxyl group. The ordered formates become unstable above 350 K under vacuum; 0.1 ML of formates desorb to relax the ordered overlayer. Remaining hydroxyl group recombines into D_2 around 400 K. Formate unimolecularly decomposes at 570 K with an activation energy of 120±10 kJ/mol and a pre-exponential factor of $2x10^{9\pm1}$ s^{-1}, releasing a mixture of CO, CO_2, D_2, D_2O and DCOOD in TDS. On the other hand, TiO_2(110) separately catalyzes two selective reactions: dehydration and dehydrogenation. The rate of dehydration increases with surface temperature below 700 K; an activation energy of 120±10 kJ/mol is observed again, being independent on the pressure of formic acid. The coincident activation energy

suggests that the true products in the decomposition of formate are CO and OD(a); the OD(a) rapidly reacts with a second DCOOD molecule to form D_2O in steady state conditions. CO_2 and D_2 observed in TDS result from branching reactions subsequent to the decomposition step. Formates decomposes so fast above 700 K that the whole reaction is limited by short supply of DCOOD. The rate of catalytic dehydrogenation reaction depends on both the coverage of formate and the pressure of DCOOD with a small activation energy of 20±10 kJ/mol, for which a bimolecular process between formate and DCOOD molecule is proposed on a kinetic simulation. These results are discussed with previous works on powdery and single crystal metal oxides.

5.2. Introduction

Metal oxide is popular material in catalytic chemistry. Many studies on polycrystalline powder have revealed that catalytic properties strongly depends on the preparation and the history of catalyst. In recent years chemistry on well-defined surface of metal oxide attracts attention in surface science community. Experimental [1,2] and theoretical [3] studies on single crystal surface pointed out that local coordination environment at surface controls the dissociation of water on metal oxide.

These studies, however, were mainly focused on characterization of adsorbates and their reaction at surface, applying photoelectron spectroscopy and thermal desorption spectroscopy. More dynamic and catalytic phenomena are attacked here. This is the first successful observation of catalytic reaction on well-defined single crystal metal oxide in a steady state, to my knowledge [4].

Acid-base character is one of the most typical properties that plays an important role in wide range of catalytic performance on metal oxide, such as cracking, isomerization and polymerization reactions [8]. Selectivity in the decomposition reaction of formic acid has been employed as a scale for acid-base property: dehydration for acidic oxide, and dehydrogenation for basic oxide [5,6]. Parallel behaviour is seen in the

decomposition of alcohols [7]. Water-gas shift reaction is catalyzed through formate intermediate over metal oxide [6]. A better understanding of traditional acid-base concept is needed in the light of microscopic structure of reaction site on oxide surface.

In this chapter, the decomposition reaction of formic acid over TiO_2(110) is characterized with and without formic acid molecules in gas phase. The mechanisms for catalytic dehydration and dehydrogenation reaction are discussed on kinetics, referring to reaction processes under vacuum. Formic acid gives a (2x1) order on TiO_2(110), stability of which phase is also discussed.

5.3. Experimental

The experiments were carried out in a VG-ESCALAB chamber capable of AES, LEED, XPS, UPS and TDS measurements with a base pressure of $1x10^{-10}$ Torr. The binding energy in Mg-Kα XPS was referred of the O(1s) level of the substrate as 530.3 eV. UPS spectrum was excited with HeI or HeII radiation. A computer (NEC PC-9801) drove a quadrupole mass filter (UTI-200) to record TDS spectrum.

A polished TiO_2(110) wafer (8x8x1 mm) obtained from Earth Jewellery Co.Ltd. was annealed to 1100 K in air for 1 hour, before cleaning under UHV. A holding device was built to cool and heat the crystal linearly through 100-900 K; the wafer and a MgO crystal were tightly bound each other with tantalum wire (0.1 mmϕ), sandwiching a gold plated tungusten mesh (0.03 mmϕ, 100 mesh). The mesh is welded on a couple of feedthrus and resistively heated. The feedthrus were attached to a liq. N_2 reservoir to be cooled. The rare face of the wafer was coated with gold to promise a good contact. A chromel-alumel thermocouple was fixed at an edge on the sample surface with ceramic glue (Aronceramic-C). This device allowed a ramping rate of 5 K/s during TDS measurement, with electric power below 20 W.

The TiO_2(110) surface was sputtered with Ar^+ ions of 5 KeV and annealed to 800 K under UHV. A sharp (1x1) pattern was observed in LEED after several cleaning cycles. No inpurity was

detected in AES nor XPS. HeI UPS confirmed the stoichiometry at the surface, though the crystal turned into deep blue after tens of the cycles due to slight reduction of the bulk. No Ti(3d) emission was detected. Oxygen deficiency would result in observable population in Ti(3d) levels [1,9].

DCOOD was used to avoid the background of H_2. DCOOD in NMR grade (Merck) was out-gassed with trap-thaw cycles. A capillary doser (ca.0.2 mmϕ) introduced the reactant in front of sample surface. Effective pressure over the surface was estimated as 20 times larger than the scale on the gauge. The doser was calibrated previously in dosing CO on a Pd(100) crystal.

A pressure jump method was adopted to measure rate of catalytic reaction in a steady state. When the crystal maintained at reaction temperature slides into a stream of formic acid molecules down the doser, catalytic reaction starts over the surface to give jumps in the partial pressure of products. Ideally, the reaction rate would correspond to the jumping height for the individual product. Negative jump, however, was often observed. Figure 5-1 shows typical records in this method. The crystal was brought into the flow at t=60 s and stayed until t=240 s. Negative jumps observed in D_2, D_2O and CO_2 resulted from the adsorption of formic acid on cold parts of the holder. The background levels recorded before and after reaction period were padded by fragmentation of DCOOD in the mass filter. Thus, the true rate for each product is deduced from the gap between two jumps, recorded at a reaction temperature and at 250 K. No catalytic reaction is expected at 250 K.

5.4. Results

5.4.1. Surface reaction under vacuum

(a) TDS

Figure 5-2 shows a TDS spectrum recorded after 3 L DCOOD exposure at 230 K, where a (2x1) overlayer was completed as mentioned below. The relative amount of products is listed in Table 5-1; the sensitivity of the mass filter has been calibrated. The products are classified into three groups with desorption temperature. DCOOD and D_2O were detected at 300-350 K, followed by a broad desorption peak of D_2 around 400 K. Finally, a mixture of CO, D_2O, CO_2, D_2 and DCOOD were observed at 570 K.

The kinetics of the last event were analyzed. The peak temperature T_p was recorded with heating rate β varied among 0.5-4 K/s. The five products are simultaneously released at the decomposition of a unique adsorbate, since they shifted together in temperature. The results in XPS and UPS will assign the intermediate into formate. The peak temperature of the decomposition products exhibited no shift against the initial coverage of formic acid. Thus, the intermediates unimolecularly decompose on first-order kinetics. Activation energy E and pre-exponential factor ν for a first order process have the following relation to T_p and β [10]:

$$\ln(T_p^2/\beta)=E/(RT_p) + \ln[E/(R\nu)], \quad (1)$$

where R represents the gas constant. A straight line with E=120±10 kJ/mol and $\nu=2\times10^{9\pm1}$ s-1 fits the observed data in Fig.5-3.

(b) LEED

Clean TiO_2(110) surface gave a (1x1) pattern in LEED. An exposure of 3 L DCOOD at 180 K increased uniform background in intensity, keeping the (1x1) diffraction. The background was decreased with annealing to 200 K. The fractional spots in a (2x1) pattern then appeared at 230 K. Further heating to 350 K transformed the (2x1) diffraction into another (1x1) pattern, accompanied by the desorption of DCOOD and D_2O. The resulted (1x1) diffraction was maintained above 800 K. The transition was irreversible; the (2x1) pattern was not recovered, when the (1x1) surface transformed at 350 K was cooled down again under UHV. In contrast, a small additional exposure to DCOOD easily restored the (2x1) order on the (1x1) surface at 300 K.

Under an atmosphere of 1×10^{-7} Torr formic acid, the (2x1) order persisted up to 400 K. This shift in transition temperature

demonstrates that the ordered overlayer is equilibrated with DCOOD molecules in gas phase.

(c) UPS and XPS

Figure 5-4 shows typical HeII UPS spectra on TiO_2(110). Clean (110) surface has a couple of intense emissions at 6 and 8 eV in curve a; they are assigned to O(2p) valence bands with bonding or non-bonding character [3]. 3 L exposure of DCOOD at 180 K gave additional features. Successive annealing to 270, 400 and 650 K were traced in curve c to e. These spectra were differenciated to detect detailed changes upon heating and hence to distinguish contribution of molecular and dissociated species.

Curve c-d and d-e have three peaks at 5.0, 10.6 and 14.2 eV; they represent $1a_2+6a_1+4b_2$, $1b_1+3b_2+5a_1$ and $4a_1$ orbitals of dissociated formates in a rather high symmetry, C_{2v}. The assignment is based on formate on Cu film [11] and Cu(110) [12]. This indicates that formates covered the surface above 270 K arranging the (2x1) order. The emission of formates gave no change in feature but decreased in intensity, when the (2x1) order disappeared at 350 K.

Curve b-c consists of four peaks at 6.0, 9.5, 11.9 and 15.9 eV; they are assigned to 10a+2a", 9a+1a", 8a+7a and 6a levels of formic acid adsorbed molecularly [11,12]. They were superimposed on stronger peaks of formate in curve b. Hence, formic acid gives a mixed multilayer of molecular and dissociated species at 180 K. Molecularly condensed DCOOD sublimates leaving formate on the surface.

No other adsorbates could be distinguished in UPS, though dissociated hydrogen atoms stay on the surface at 270 K and probably form hydroxide with oxygen anions of the substrate. Its emission may be much weaker than the contribution of formate.

Carbon (1s) emission was observed at 288.9 eV in XPS on a saturated (2x1)-formate overlayer at 247 K. This value is acceptable for the carbon atom in a formate. The intensity relative to that of O(1s) level of lattice oxygen anion allows estimation on surface density of carbon atom. The orbital cross section, escape depth of the photoelectrons and the transmission of the spectrometer should be considered. As a result, a density of 0.5 ML is obtained for the (2x1)-formate overlayer. Here, density is referred to the surface unit cell on clean (110): 1 ML corresponds to 5.21×10^{18} m^{-2} [13]. When the (2x1) surface was annealed at 353 K to lose the order, the C(1s) intensity decreased to 80% of the original value without a shift in binding energy. It means that formate overlayer of 0.4 ML cannot maintain the (2x1) order. No emission was detected in C(1s) region after annealing to 650 K.

The work function was measured on the cutoff in secondary electrons in UPS spectrum. A completed (2x1)-formate surface had 4.2±0.1 eV, while a clean (110) gave 5.3±0.1 eV. The decrease of 1.1 eV corresponds an upward dipole of 0.9 Debye.

5.4.2. Catalytic reaction

(a) Reaction rate and activation energy

Applying the jump method described, four products were detected in catalytic decomposition reaction above 500 K: CO, D_2O, CO_2 and D_2. Neither formaldehyde nor methylformate was observed. The jumping measurement was repeated varying surface temperature and the pressure of DCOOD. Figure 5-5 summarizes the rate of production in a set of Arrhenius plots. The pumping rate and the sensitivity of the mass filter have been calibrated for each product, by dosing a given mixture of the products under reaction conditions. Every product exhibited no induction period; the time courses in partial pressure always gave plateus as shown in Fig.5-1.

There are two selective reactions separately catalyzed on TiO_2(110): dehydration and dehydrogenation reactions. Stoichiometry is balanced in the products of each catalytic reaction. Their response to surface temperature is entirely different. Dehydration dominates at elevated temperature, while lower temperature favors dehydrogenation reaction. The rates for dehydrated CO and D_2O are rapidly accelerated with surface temperature to saturate above 700 K in Fig.5-5. An activation energy of 120±10 kJ/mol fits the data below saturation. Saturation temperature shifts

higher with increasing pressure of DCOOD. On the other hand, the rates in CO_2 and D_2 production increase slowly with an activation energy of 20±10 kJ/mol to have maximum around 700 K, just below saturation temperature for dehydration. The origin of the maximum will be discussed in relation to reaction mechanism. The evolution of CO_2 remained a slight increase beyond the maximum in D_2 production.

(b) Pressure dependence

Figure 5-6 shows the influence of the pressure of the acid, P_{DCOOD}, on the dehydration rate at constant temperature. The rates for CO and D_2O are nearly independent on pressure below saturation temperature; a small order of 0.2 is obtained at 650 K. On the contrary, the saturated rates are strong positive order of 0.8. The switch in reaction order suggests that the rate determining step shifts from one elementary step to another. The dehydrogenation reaction is high order of 0.9 at 650 K, as shown in Fig.5-7.

(c) Post-reaction LEED

A (2x1) super-structure was observed in post-reaction analysis by LEED, when the sample was cooled down under DCOOD flow after prolonged reaction. The observed diffraction seemed equivalent to the (2x1)-formate pattern seen under vacuum. It is hence suggested that TiO_2(110) maintains the original structure throughout reaction; absorption of formic acid and subsequent formation of titanium formate bulk is excluded.

5.5. Discussion

In the first part of discussion, surface reaction of adsorbed formic acid under vacuum is dealt with. The mechanism of catalytic dehydration reaction is then discussed on kinetic results, compared with the decomposition process observed in TDS. Finally, a bimolecular mechanism is proposed for catalytic dehydrogenation reaction.

5.5.1. Surface reaction under vacuum

Formic acid exposed at 180 K gives mixed adlayer of molecular and dissociated species on TiO_2(110). Molecular DCOOD sublimates below 270 K, leaving formate on the surface according to the results in UPS. The yielded atomic hydrogen is likely trapped on oxygen anion on the substrate, O(s), to form hydroxide. Oxygen anions on ridges are to have larger affinity to hydrogen than the planer ones have.

at 180 K;
DCOOD(a) → DCOO(a) + D(a): dissociation
D(a) + O(s) → OD(a): hydroxide formation
DCOOD(g) → DCOOD(a): condensation

at 200-230 K;
DCOOD(a) → DCOOD(g): sublimation

A model for the (2x1) overlayer is proposed in Fig.5-8: all the five-fold Ti^{4+} cations are covered by bridging formates. The three-peak feature observed in UPS is assigned to formate with C_{2v} symmetry. Bridging or bidentate configuration satisfies the symmetry. Unidentate form, the other possible style, belongs to C_s symmetry and would hence result in more complicated spectrum. Bidentate form would distort the coordination around titanium cation into seven-fold coordination. It is thus concluded that formate bridges on two Ti cations along valleys on TiO_2(110). The five-fold Ti cations to be bridged are separated by 296 pm [13], while the oxygen-oxygen distance is 220-227 pm in formate compounds, $Ca(HCOO)_2$, $Sr(HCOO)_2$ $Ba(HCOO)_2$ and $Pb(HCOO)_2$ [14]. A HREELS study reported unidentate formate on ZnO(0001)-Zn; a larger separation of 325 pm between Zn cations prefers unidentate form to bridging coordination [15]. The evaluated dipole of 0.9 Debye is a reasonable value for bridging formate with its axis normal to the surface.

Adsorbed formate has never given an ordered overlayer on MgO(100) [21,22], ZnO(0001)-Zn [15], faceted TiO_2(001) [17].

Remember that TiO_2(110) has an anisotropic structure [1,16], where ridges of oxygen atoms run along the [001] direction. The ridges are able to arrange the formates in rows. Each line of formates must match in phase in a (2x1) order. The phasing process requires a thermal activation: it corresponds to the lower limit of 230 K for the ordering. Hydroxyl group resulted from dissociation of formic acid can anchor the formate in phase through hydrogen bonds, though the location and the structure of the hydroxyls is not known.

The (2x1) order disappeared at 350 K, when DCOOD and D_2O desorbed. The recombination of formate and the disproportionation of hydroxide are responsible for the desorption.

at 350 K;
(2x1)-DCOO(a) + OD(a) → DCOOD(g) + O(s): recombination
OD(a) + OD(a) → D_2O(g) + O(s): disproportionation

Similar recombination and disproportionation reactions were reported on faceted TiO_2(001) [17] and ZnO(0001)-Zn [18], where local stability of the O-D bond in hydroxyl group was concerned about; they mentioned that liberated proton trigers off the reactions. However, the irreversible disordering coincident with the desorption suggests that the stability of the whole overlayer plays a more important role. The adsorbates in the (2x1) layer have no freedom of diffusion across the surface as illustrated in Fig.5-8. The resulted loss in entropy destabilizes the ordered layer with increasing temperature, combined with dipole repulsion between formates. It is reasonable that a part of formates (0.1 ML) desorb at 350 K to relax the overlayer. The relaxed overlayer contains 0.4 ML of formate and 0.2 ML of vacant five-fold cation, where a formate neighbours a vacant cation on an average. The liberated space promotes diffusion and thereby breaking the long range order. This idea is in line with the fact that a small additional exposure to DCOOD at 300 K could recover the (2x1) order on a relaxed (1x1) surface. It is reasonable to claim surface diffusion of formates at 350 K. Metal formate has low melting points: 526, 441, 374 and 389 K

for NaHCOO, KHCOO, TlHCOO and NH_4HCOO, respectively [19]. If local activation of O-D bond was the only origin of the desorption, all the hydroxyls should disappear at this stage. It is not the case. Desorption of D_2 was observed around 400 K; certain amount of D atoms survives. D_2 likely comes from the recombination of remaining hydroxyl group. Recombinative desorption of hydrogen was observed on H(D)/Cu_2O(100) [20] at similar temperature, while no molecular hydrogen was detected on faceted TiO_2(001) [17], ZnO(0001)-Zn [18] and MgO(100) [21,22] in TDS following exposure of formic acid.

around 400 K;
OD(a) + OD(a) → D_2(g) + 2O(s): recombination

There are 0.4 ML of formates left on the surface after the recombinative desorption. The formates decomposed at 570 K into a mixture of CO, D_2O, CO_2, D_2 and DCOOD.

at 570 K;
DCOO(a) → CO(g) + D_2O(g) + CO_2(g) + D_2(g) + DCOOD(g)

The decomposition is a unimolecular process of adsorbed formate, since it is in first order with the coverage. Every product shifted together in TDS when heating rate was varied. This means that uniform formates decompose into the products. If there were two kinds of sites on the surface specific for dehydration or dehydrogenation with different activation energy, the products would shift separately.

The decomposition of formate is a popular process on metal oxide, as shown in Table 5-2 and 5-3. The observed E and ν agree with the reported values in Table 5-2. Contrary to the accordance in the kinetic parameters, the selectivity in the decomposition products spreads over in Table 5-3. MgO(100) selectively yields CO, while CO_2 is a dominant product on ZnO(0001)-Zn. The selectivity on (110) and faceted (001) surfaces of rutile sit among the two extreme cases. Interestingly, the selectivity in TDS is not in accordance with catalytic properties of these

oxides. Both MgO and ZnO catalyze selective dehydrogenation reaction, hence to be classified as basic oxide. TiO_2 is more acidic one to perform dehydration reaction [5]. This contradiction tells that acid-base character in catalysis should be distinguished from surface reaction observed in TDS, even on single crystal surface. This point will be discussed again relating to the mechanism of catalytic reaction.

Apart from dehydration/dehydrogenation selectivity, formaldehyde is a characteristic product on (114)-faceted TiO_2(001) surface; two formates disproportionate on a Ti^{4+} cation with multiple coordination vacancies [17]. The absence of DCDO is reasonable on TiO_2(110), because the ideal (110) plane contains no four-fold coordinated cation capable of the disproportionation.

All the results in AES, LEED, XPS and UPS show that formate completely decomposes at 570 K to leave a clean (1x1) surface of TiO_2(110). The disproportionation of OD(a) to D_2O at 350 K leads loss of oxygen atoms on the substrate. Atomic ratio in the desorption products at 570 K is summed up in Table 5-1 as D:C:O=40:39:67. Comparing the composition of DCOO, certain amount of oxygen is consumed to restore stoichiometry on the surface.

5.5.2. Mechanism of catalytic dehydration reaction

The rate determining step for catalytic dehydration reaction switched around 700 K. The reaction rate increased with an activation energy of 120 kJ/mol in low temperature region, being 0.2 order on the pressure of DCOOD. The small order satisfies a picture where intermediates thoroughly cover the surface and its decomposition determines the rate. Indeed, formate decomposes with an activation energy of 120 kJ/mol in TDS. The equivalent values assign the intermediate into formate.

The decomposition of formate on TiO_2(110) gives, however, CO_2 and D_2 in TDS, in addition to the dehydrated products. Of course, dehydrogenation reaction also occurred in a steady state, but it has entirely different kinetics and should be separately considered. Recalling the decomposition is a

unimolecular process of adsorbed formate, a second molecule of DCOOD from gas phase cannot participate in the decomposition step itself even in a steady state. The second molecule perturbs reactions following the decomposition. It is thus proposed that the unimolecular decomposition of formate selectively yields CO(g) and surface hydroxyl group OD(a). Some successive reactions are responsible for the by-products seen in TDS. If a second DCOOD reacts with the resulted OD fast enough to give D_2O, a dehydrating cycle works well.

$$DCOO(a) \rightarrow CO(g) + OD(a)$$
$$OD(a) + DCOOD(g) \rightarrow D_2O(g) + DCOO(a)$$

The decomposition step is rate limiting below the saturation temperature. When temperature is raised, the decomposition becomes so fast that the rate of the whole reaction is determined by short supply of DCOOD. The production of dehydrated species saturates with temperature, and turns in first order on the pressure of DCOOD. It is just what was observed.

Check the proposed scheme again in turn over frequency. TOF for dehydration approaches the collision frequency of DCOOD molecules in the high temperature limit. Take an example; the rate for CO started to saturate at 700 K with a DCOOD pressure of $1x10^{-5}$ Torr. A TOF of 9 $s^{-1}site^{-1}$ is estimated at 700 K for the decomposition of formate, on the basis of the kinetic parameters obtained in TDS. On the other hand, the collision frequency f is approximately given as follows;

$$f=P_{DCOOD}/(2\pi mRT)^{1/2}, \quad (2)$$

where m and T are mass and temperature of formic acid. Assuming $P_{DCOOD}=1x10^{-5}$ Torr and T=300 K, the frequency is estimated as f=10 $s^{-1}site^{-1}$. The agreement in TOF with f supports the scheme.

The dehydration cycle works under higher pressure of formic acid. Polycrystalline TiO_2 is known to be a dehydration catalyst [5,23,24]. Munuera [24] studied the catalytic decomposition on TiO_2 powder above 630 K with a HCOOH pressure of 6 Torr,

observing a selectivity near 90% for dehydration under zeroth order kinetics. An activation energy of 105 kJ/mol and a pre-exponential factor of 2×10^{27} molecules $m^{-2} s^{-1}$ were also reported. The latter corresponds to 7×10^{8} molecules $site^{-1} s^{-1}$. These values are compatible with mine. It is thus suggested that dehydration reaction on the polycrystalline catalyst is catalyzed by the same mechanism as on rutile (110), though Munuera proposed that the formation of water from hydroxyls limits the rate [24].

How about other metal oxides? This issue opens discussion on traditional acid-base properties in a microscopic level. Selective decomposition of formate seems a general process in Table 5-2 and 5-3, including "basic" oxide such as ZnO(0001) and MgO. Catalytic dehydration can be expected through the decomposition of formate on those "basic" metal oxide. Low selectivity for dehydration observed on "basic" catalyst can result from change in structure and composition on substrate under reaction conditions. Polycrystalline powder of MgO and ZnO readily absorbs formic acid to form three-dimensional metal formate [26]. Adsorbed formic acid performs no reaction on a O-terminated polar surface, $ZnO(000\bar{1})$-O; only desorption of molecular species was observed in TDS [18]. Formic acid cannot find cation on the O-terminated surface. Another path for dehydration, protonation mechanism, might be possible on such an inert surface. Fukuda et al. proposed that proton transfer from substrate to formic acid initiates catalytic dehydration reaction on Al_2O_3 and SiO_2 [25]; it is an analogue of acidic catalysis in liquid phase. Anyhow, more experimental work on well-defined catalyst is required to address this issue.

Formate on transition metal surface mainly decomposes into carbon dioxide and hydrogen [5]. The hydrogen atom in a formate readily moves on the substrate breaking the C-H bond. Large affinity for hydrogen seems the origin of this step on transition metal. The present study shows that formate cannot decompose in this way on TiO_2(110). An acceptable reason for this fact is that TiO_2(110) has small affinity to hydrogen. The hydrogen atom is intra-molecularly transferred to one of the oxygen atoms yielding CO and OD, as an alternative path. If one regards

TiO_2(110) as a prototype of metal oxide, the picture of small affinity is generally drawn on metal oxides.

The following reactions can produce the observed by-products under vacuum;

$$OD(a) + DCOO(a) \rightarrow DCOOD(g) + O(a)$$
$$OD(a) + DCOO(a) \rightarrow D_2(g) + CO_2(g) + O(a)$$
$$OD(a) + OD(a) \rightarrow D_2O(g) + O(a)$$
$$OD(a) + OD(a) \rightarrow D_2(g) + 2O(a)$$
$$O(a) + DCOO(a) \rightarrow CO_2(g) + OD(a)$$

The coverage of reactive O(a) or OD(a) is related to redox property of substrate. Peng et al. pointed out that the dehydration/dehydrogenation selectivity in TDS reflects redox property of substrates; net dehydration does not require reduction of substrate but oxidative dehydrogenation does [22].

5.5.3. Mechanism of catalytic dehydrogenation reaction

The rate of dehydrogenation reaction has maximum in the Arrhenius plots of Fig.5-5, accompanied with the saturation in dehydration. This characteristic behaviour leads to a bimolecular mechanism. Formates decomposes so fast that the coverage goes down at elevated temperature. The observed maximum thus suggests that dehydrogenation reaction requires surface formate. The formate, however, decomposes by itself to the dehydrated products. Dehydrogenation reaction needs another participant.

Figure 5-7 shows first order kinetics in dehydrogenation reaction. Hence, a DCOOD molecule from gas phase participates in the reaction. This idea is numerically tested by simulation on the following model; Formic acid is adsorbed on vacant site with a rate of $f(1-\theta)$ where θ is the coverage of formate.

$$DCOOD(g) \xrightarrow{f(1-\theta)} DCOO(a)$$

Formate unimolecularly decomposes into the dehydrated products

with a rate v_1.

$$DCOO(a) \xrightarrow{v_1} CO+OD(a)$$

where,

$$v_1 = \nu_1 \exp[-E_1/(RT)]\theta, \quad (3)$$

Otherwise, formate reacts with a DCOOD molecule to give the dehydrogenated products.

$$DCOO(a) + DCOOD(g) \xrightarrow{v_2} CO_2 + D_2 + DCOO(a)$$

The rate in dehydrogenation v_2 is thereby given by the product of the collision frequency and the coverage with an Arrhenius type dependence on surface temperature;

$$v_2 = f\theta\exp[-E_2/(RT)], \quad (4)$$

This model is calculated on the observed parameters: $\nu_1 = 2\times10^9$ s^{-1}, $E_1 = 120$ kJ/mol and $E_2 = 20$ kJ/mol. A typical result in Fig.5-9 successfully represents the observed kinetics, assuming $f = 1$ s^{-1}.

In Fig.5-5, CO_2 still increases beyond the maxima in D_2 production. Collision limiting situation at elevated temperature leads to CO_2 production through the branching reactions following the decomposition of formate. The secondary contribution is added on the true production by the proposed mechanism.

Dehydrogenation reaction usually has a higher activation energy than that of dehydration reaction on a metal oxide catalyst [5]. It is not the case in the present study. The observed activation energy, 20 kJ/mol, is too small for a barrier in cleavage of a chemical bond, and suggests that the rate limiting step is coordination of a DCOOD molecule at a formate to form reaction complex. Otherwise, a formate reacts with a weakly bound DCOOD molecule equilibrated with gas phase. The apparent activation energy is then smaller than the true barrier

by the heat of adsorption of the molecular species.

Although powdery TiO_2 is a selective catalyst for dehydration [5,23,24], TiO_2(110) favors dehydrogenation at 500 K. There are two ways to consider this discrepancy. If dehydrogenation is characteristic reaction on (110) plane of rutile, polycrystalline catalyst can be unfavorable. However, crystallographic studies on faceted (001) [27,28] and reconstructed (100)-(1x3) surfaces [29] revealed that (110) is most stable surface of rutile. It is less plausible that (110) plane is a minority on rutile powders. Another crystal form, anatase, further complicates the situation, which structure becomes favourable depending on history of catalyst. The other possible origin is reactivity of formate overlayer. If an accessible cation and/or certain space is required around a formate to form reaction complex, complete (2x1)-formate phase suppresses the dehydrogenation process. There is no accessible cation left on the (2x1) surface, whereas 0.2 ML of 5-fold cations remain vacant in the relaxed overlayer. According to LEED observation, the (2x1) phase cannot persist in the reaction conditions here. Higher pressure, employed in usual catalytic studies, is capable of forming close-packed overlayers, since the (2x1) phase is equilibrated with formic acid in gas phase. Catalytic study under higher pressure will distinguish the two possibilities on TiO_2(110).

Several studies have reported bimolecular processes in dehydrogenation reaction. A co-adsorbed water molecule assists dehydrogenating decomposition of a formate on MgO powder [30]. Bimolecular reaction of a formate with an impinging formic acid molecule was proposed for selective dehydrogenation reaction on ZnO and MgO powder [26]. It is interesting to relate the bimolecular dehydrogenation on TiO_2(110) to the reported processes. Further studies in catalysis on well-defined surfaces, such as MgO(100) and ZnO(0001)-Zn, are needed to address this point.

5.6. Conclusions

On TiO_2(110);

(1) Unimolecular decomposition of surface formate is a selective process to CO and OD(a), though CO_2 and D_2 are apparent in TDS. The latter products come from branching reactions under vacuum following the decomposition step.

(2) A selective dehydration reaction is catalyzed in a steady state by the cycle of two steps: the unimolecular decomposition of formate and subsequent production of water.

(3) A bimolecular process between a formate and a formic acid molecule catalyzes a selective dehydrogenation reaction.

(4) Saturated formate layer with a (2x1) order becomes unstable above 350 K under vacuum. Recombinative desorption of 0.1 ML of formates relaxes the overlayer to allow diffusion across the surface.

(5) Hydrogen atoms adsorbed on TiO_2(110) recombines to desorb around 400 K.

5.7. references

1. V.E.Henrich, Prog.Surf.Sci.9(1979)143;
   V.E.Henrich, Prog.Surf.Sci.14(1983)175;
   V.E.Henrich, Rep.Prog.Phys.48(1985)1481;
   G.Heiland and H.Lüth, in: The Chemical Physics of Solid Surfaces and Heterogeneous Catalysis, Vol.3, Elsevier,Amsterdam(1984), chap.4.
2. H.Idriss, M.Libby and M.A.Barteau, Catal.Lett.,in press.
3. M.Tsukada, H.Adachi and C.Satoko, Prog.Surf.Sci.14(1983)113.
4. J.A.Rodriguez and D.W.Goodman, Surf.Sci.Rept.14(1991)1.
5. P.Mars, J.J.F.Scholten and P.Zwietering, Advan.Catal.14(1963)35.
6. J.J.F.Scholten, P.Mars, P.G.Menon and R.van Hardereld, in: Proc.3rd Intern.Congr.Catal., Vol.2, Wiley, New York(1965), p.881.
7. Z.G.Szabo, J.Catal.6(1966)458.
8. B.C.Gates, in: Chemistry in Catalytic Processes, Mcgraw-Hill, New York(1979).
9. Y.W.Chung, W.J.Lo and G.A.Somorjai, Surf.Sci.64(1977)588.
10. P.A.Redhead, Vacuum 12(1962)203.
11. R.W.Joyner and M.W.Roberts, Proc.R.Soc.Lond.A350(1976)107.
12. M.Bowker and R.J.Madix, Surf.Sci.102(1981)542.
13. R.W.G.Wyckoff, in: Crystal Structure 2nd edition, Vol.1, Wiley, New York(1965), p.251.
14. R.W.G.Wyckoff, in :Crystal Structure 2nd edition, Vol.5, Wiley, New York(1966), p.121.
15. W.T.Petrie and J.M.Vohs, Surf.Sci.245(1991)315.
16. V.E.Henrich and R.L.Kurtz, Phys.Rev.B23(1981)6280.
17. K.S.Kim and M.A.Barteau, Langmuir 6(1990)1485.
18. J.M.Vohs and M.A.Barteau, Surf.Sci.176(1986)91.
19. CRC Handbook of Chemistry and Physics 63rd edition, CRC Press, Boca Raton(1982).
20. K.H.Schulz and D.F.Cox, Surf.Sci.278(1992)9.
21. Y.Yamamoto, N.Akamatu, A.Wada, K.Domen and C.Hirose, to be submitted.
22. X.D.Peng and M.A.Barteau, Catal.Lett.7(1990)395.

23. J.M.Trillo, G.Munuera and J.M.Criado, Catal.Rev.7(1972)51.
24. G.Munuera, J.Catal.18(1970)19.
25. K.Fukuda, Y.Noto, T.Onishi and K.Tamaru, Trans.Faraday Soc.63(1967)3072.
26. Y.Noto, K.Fukuda, T.Onishi and K.Tamaru, Trans.Faraday Soc.63(1967)3081.
27. L.E.Firment, Surf.Sci.116(1982)205.
28. K.S.Kim and M.A.Barteau, J.Catal.125(1990)353.
29. P.Zschck, J.B.Cohen and Y.W.Chung, Surf.Sci.262(1992)395.
30. T.Shido, K.Asakura and Y.Iwasawa, J.Catal.122(1990)55.
31. T.Shido and Y.Iwasawa, J.Catal.129(1991)343.

Table 5-1. The relative amount of desorption species on (2x1)-formate overlayer on TiO_2(110). The sensitivity of the mass filter was corrected.

Temperature	Product	Relative amount
350 K	DCOOD	12
	D_2O	10
400 K	D_2	2
570 K	CO	16
	CO_2	11
	D_2O	5
	D_2	3
	DCOOD	12

Table 5-2. Kinetic parameters for the decomposition of adsorbed formate under vacuum.

Substrate	Activation energy / kJ/mol	Pre-exponential factor / s^{-1}	Reference
TiO_2(110)	120±10	$2x10^{9\pm1}$	this work
TiO_2 powder	105	$3x10^{8}$	24
MgO powder	155	$5x10^{12}$	30
ZnO powder	155	$1x10^{12}$	31

Table 5-3. Selectivity in the decomposition of formate under vacuum.

Substrate	T_p[a]/K	Relative amount of products[b] CO	CO_2	D_2 (H_2)	D_2O (H_2O)	DCOOD (HCOOH)	DCDO (HCHO)	Reference
TiO_2(110)	570	10	7	2	3	8	0	this work
TiO_2(001)-(011) faceted	560	10	4	(trace)	0	(4)	0	17
TiO_2(001)-(114) faceted	570	10	5	0	0	(3)	(2)	17
MgO(001)	520	10	0	0	(c)	0	0	22
MgO powder	560	10	0	0	0	0	0	30
ZnO(0001)-Zn	575	10	39	9	0	0	0	18
ZnO powder	550	10	0	4	0	0	0	31

[a] peak temperature in TDS
[b] relative to CO
[c] not qualified

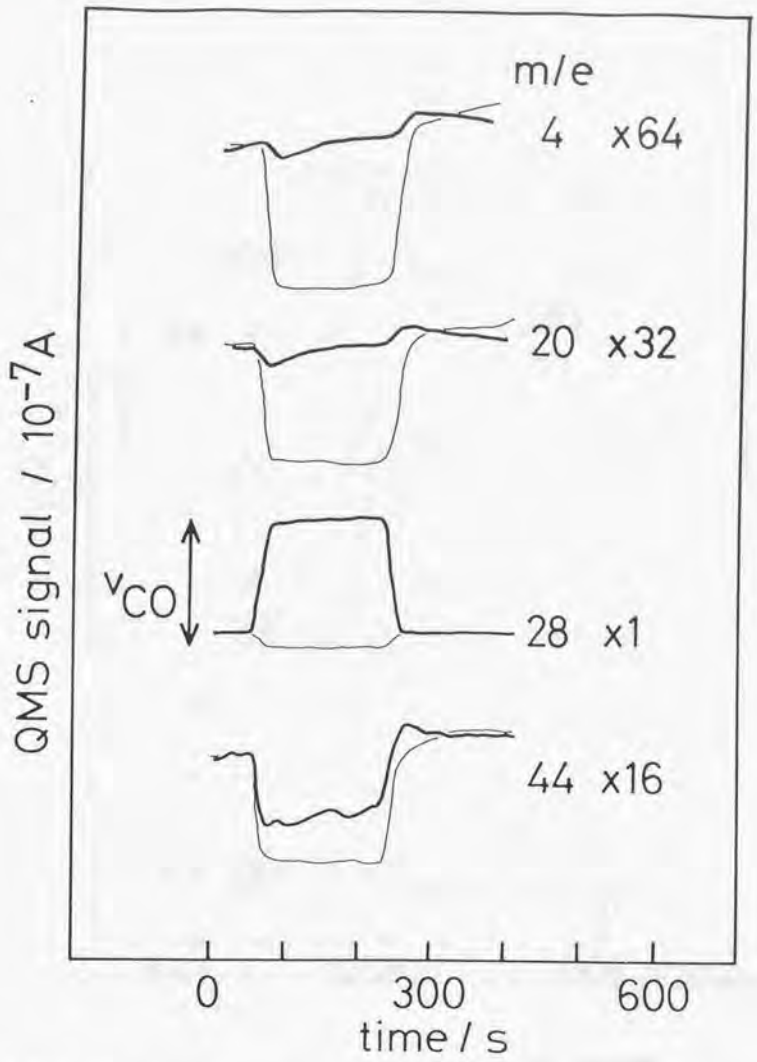

Fig.5-1. Response in the pressure jump method. Solid line: recorded on the sample at 800 K; thin line: recorded at 250 K as a reference. An effective pressure of DCOOD was estimated as $4x10^{-7}$ Torr over the crystal. v_{CO} corresponds to the rate for CO production. See text in detail.

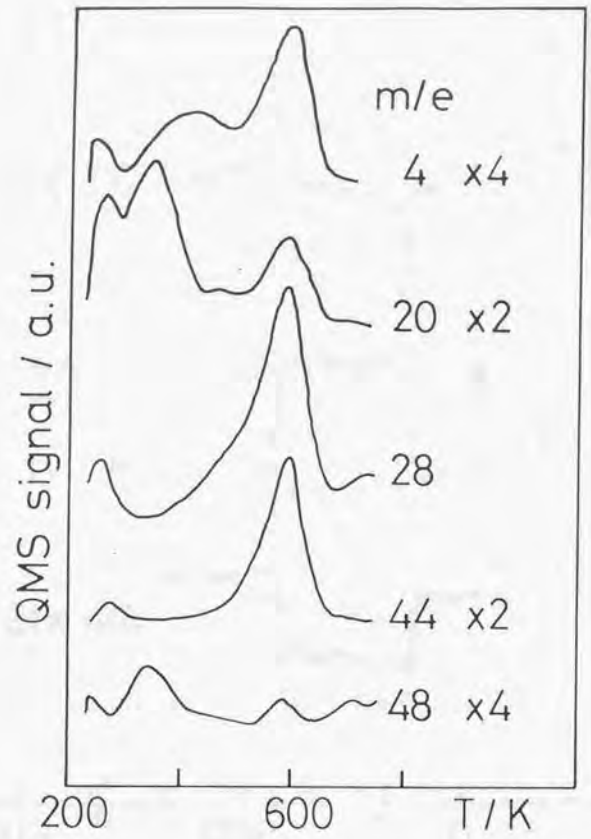

Fig.5-2. Thermal desorption spectrum following 3 L DCOOD exposure at 230 K on TiO_2(110) surface. A (2x1)-DCOO overlayer was completed. Heating rate was 2 K/s.

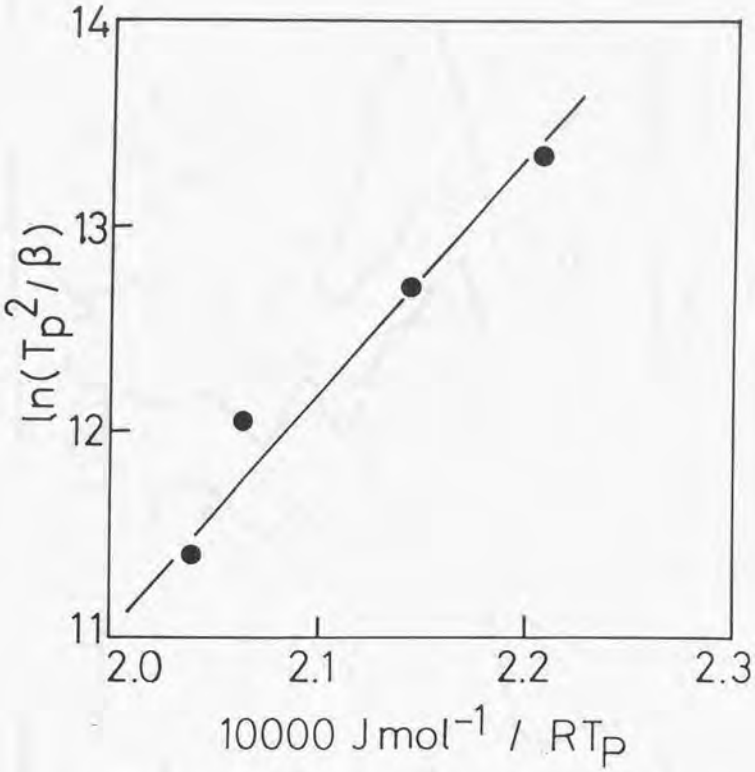

Fig.5-3. Peak temperature of the decomposition of formate with heating rate.

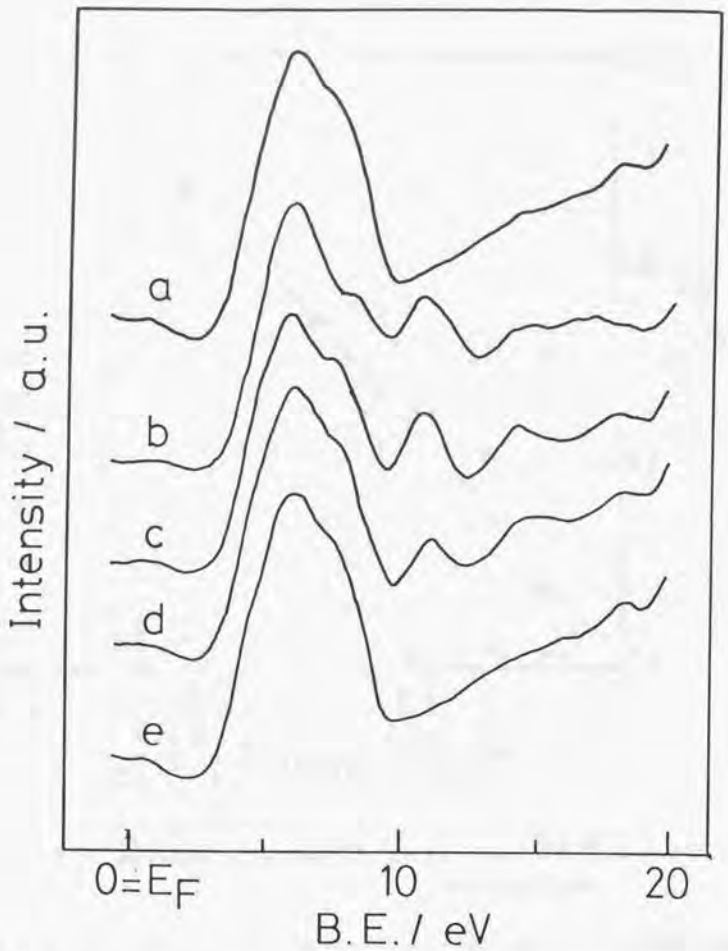

Fig.5-4. HeII UPS spectra of formate on TiO_2(110):
a, TiO_2(110); b, exposed to 3 L formic acid at 180 K;
c, d, e, successively annealed to 270, 400 and 650 K, respectively. The spectra were taken on surface cooled down to 180 K.

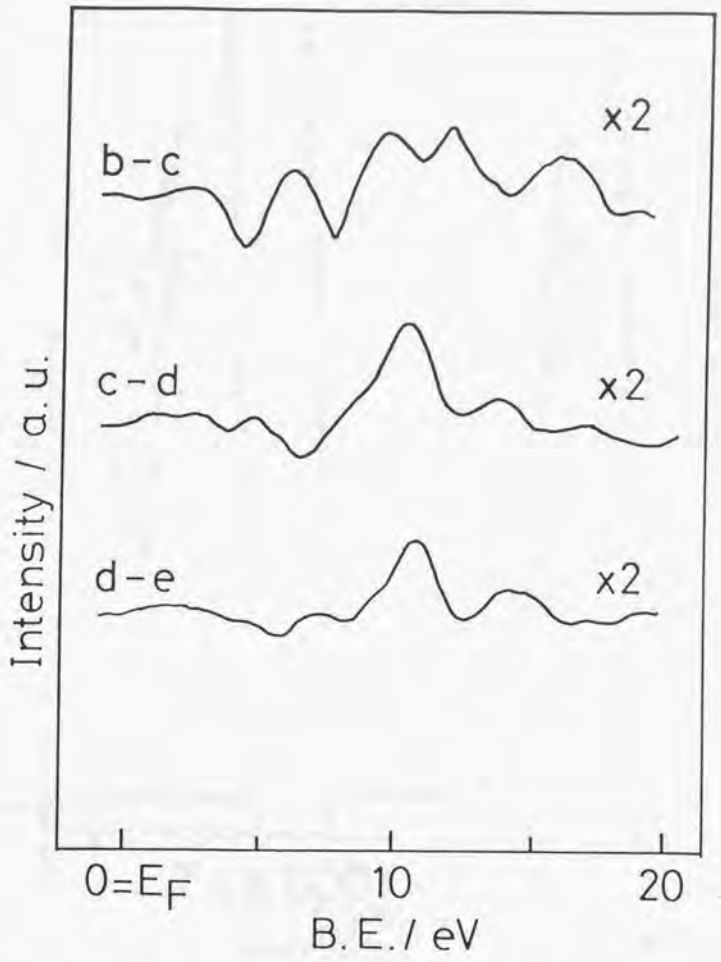

Fig.5-4. continued.

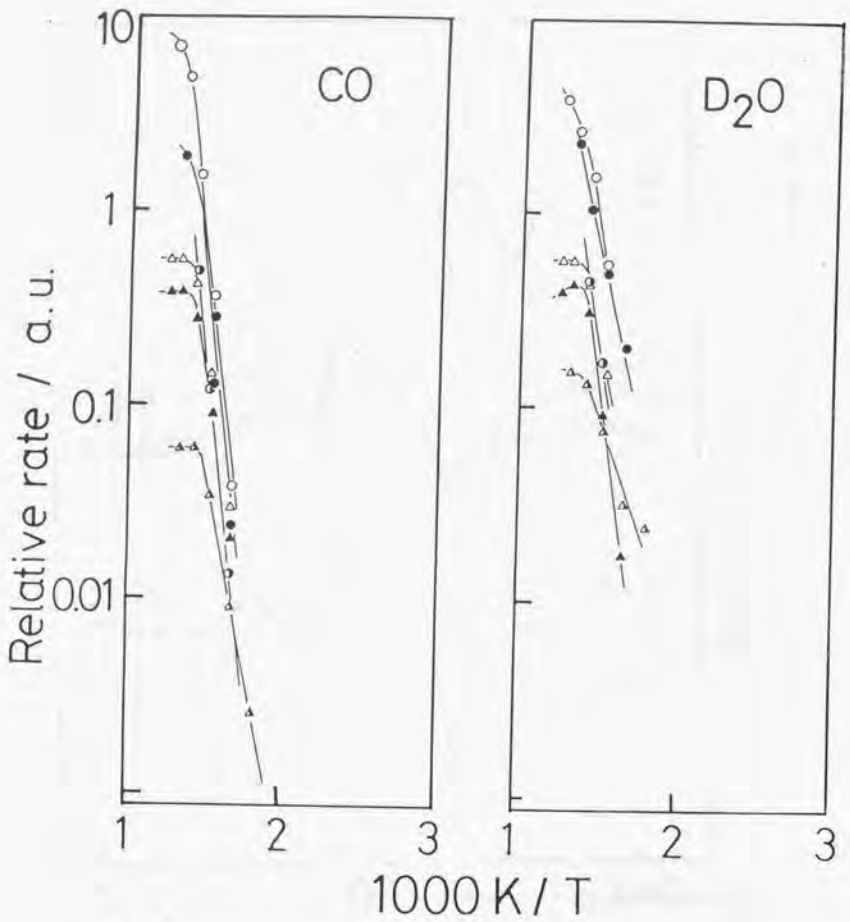

Fig.5-5. Rates for catalytic decomposition of formic acid on TiO_2(110) with different pressure of formic acid: ○, $1x10^{-5}$; ●, $5x10^{-6}$; ◑, $1x10^{-6}$; △, $4x10^{-7}$; ▲, $2x10^{-7}$; ▲, $3x10^{-8}$ Torr.

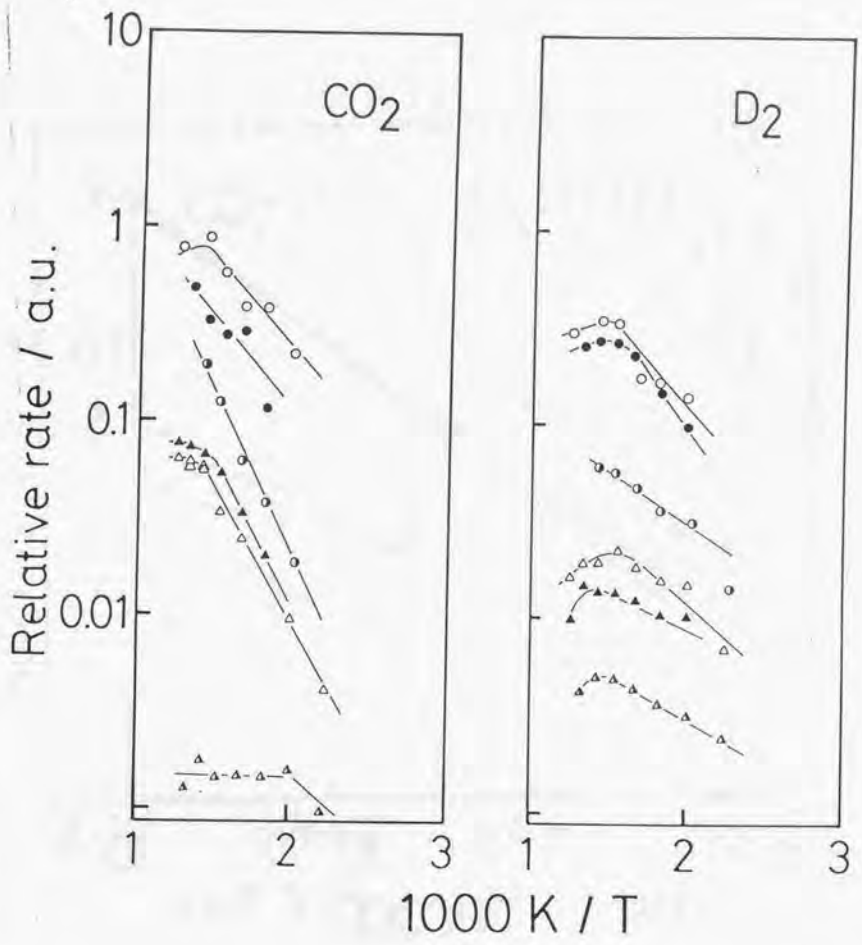

Fig.5-5. continued.

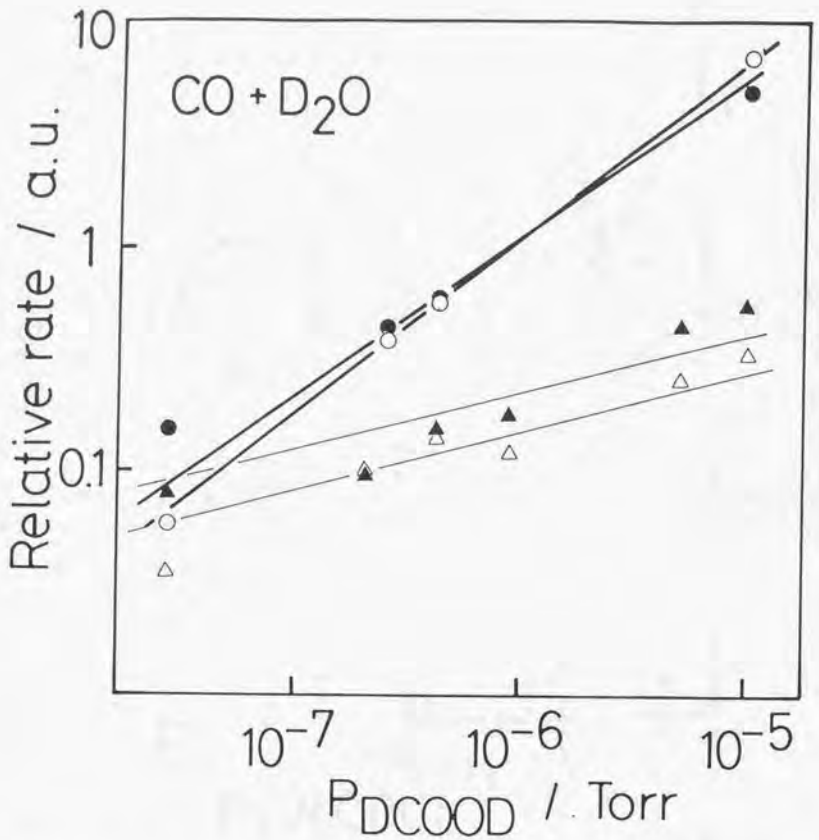

Fig.5-6. Reaction rate for dehydration with pressure of formic acid.
△:CO(650 K),▲:D_2O(650 K),
○:CO(saturated),●:D_2O(saturated)

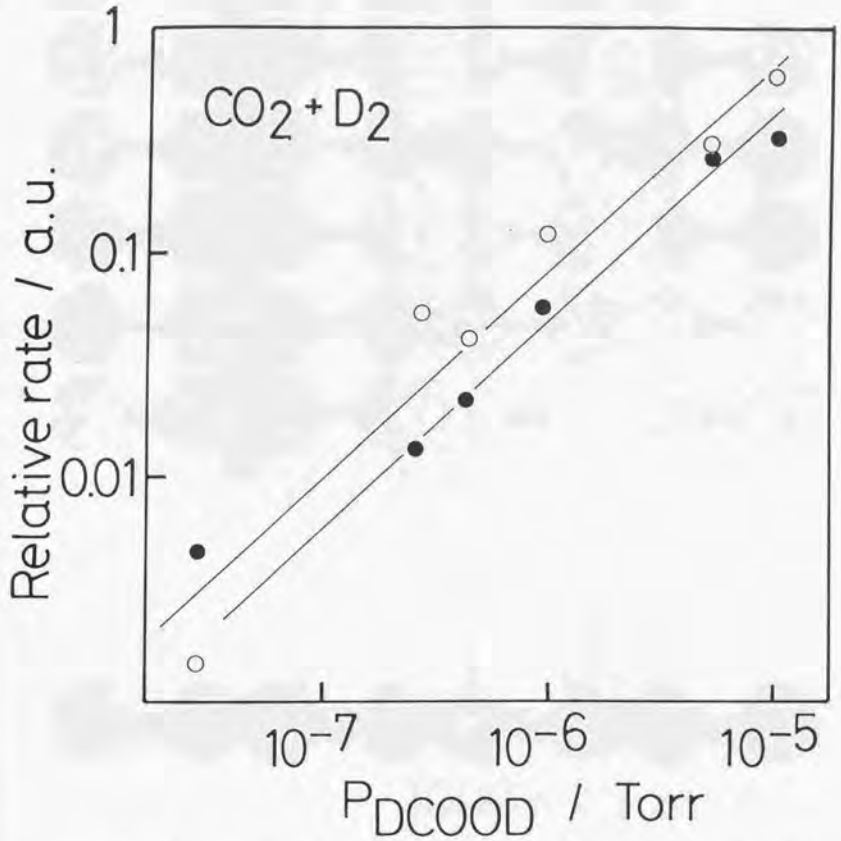

Fig.5-7. Reaction rate for dehydrogenation with pressure of formic acid.
○:CO_2(650 K), ●:D_2(650 K)

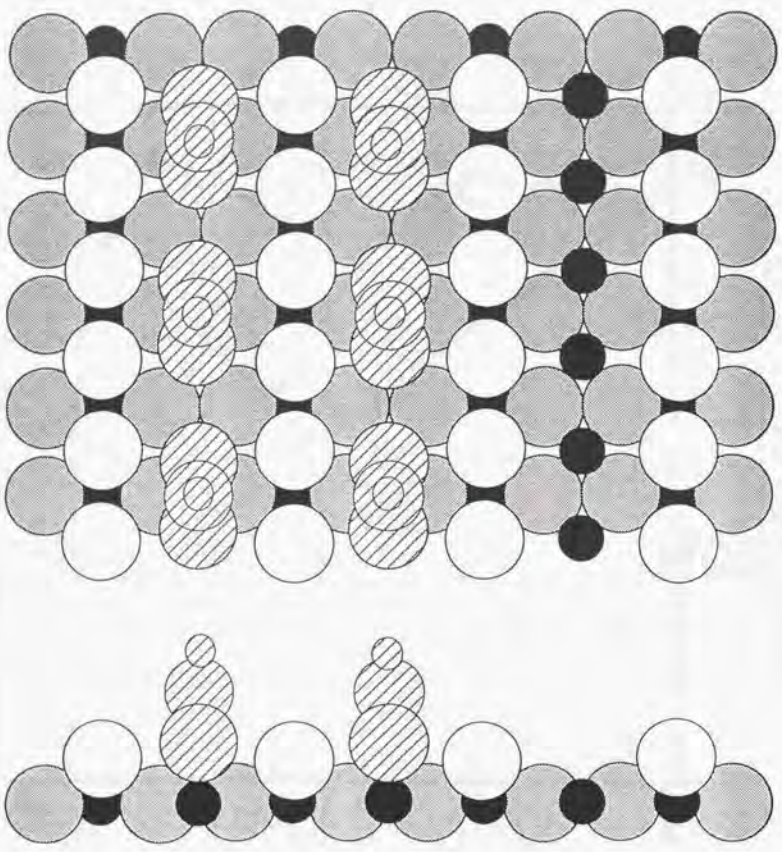

Fig.5-8. A model for the TiO_2(110)-(2x1)-DCOO overlayer. open and shaded circle: O^{2-}, filled circle: Ti^{4+}, hatched circles: bridging formate. Formates cover the left side for illustration. Hydroxyl groups are not shown.

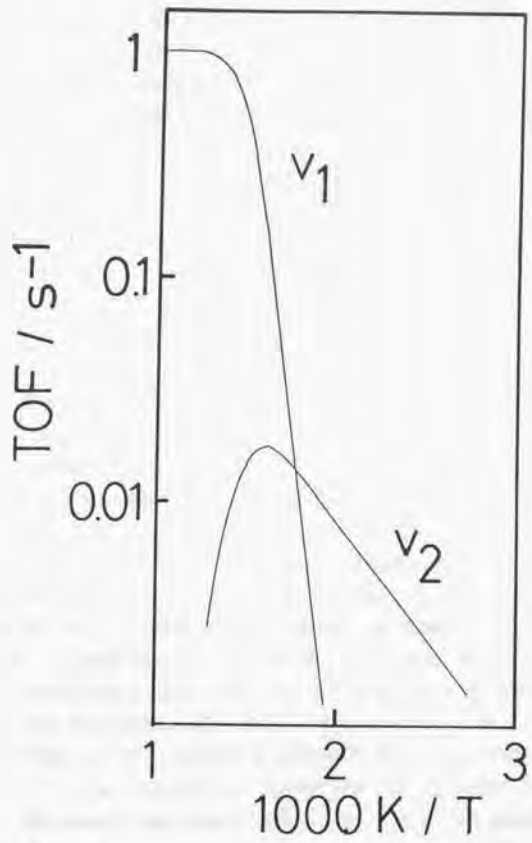

Fig.5-9. Reaction rates simulated on the proposed mechanism with a collision frequency of 1 s^{-1}. v_1 :dehydration, v_2 :dehydrogenation.

Chapter 6

Modification of surface electronic states on TiO_2(110) and (441) by Na adatoms

6-1. Abstract

Sodium adatoms deposited on (110) and stepped (441) surfaces of TiO_2(rutile) are examined with XPS, UPS, XAES (X-ray excited Auger electron spectroscopy), EELS and LEED. Na adatoms form an atomic layer at 298 K interacting with oxygen anions on TiO_2(110). A c(4x2) ordered structure appears at 0.5 ML, for which a model of ordered "Na_2O-dimer"s is proposed. The "Na_2O-dimer" units complete arrays along the [001] direction in (1x1) periodicity at 1 ML. Na adatoms give electrons to the substrate, resulting in a downward band bending toward the surface. When the Fermi level crosses an unfilled surface state localized on five-fold coordinated Ti^{4+} cations, they are reduced to Ti^{3+} state. The observed interaction of Na adatoms is ascribed to open structure and reactive surface states of oxygen anions on TiO_2(110). The adatoms on step structure over (441) surface give almost the same picture as on (110) plane.

6-2. Introduction

Metal oxide is indispensable substrate for metal supported catalyst. However, few studies have been performed on well-defined single crystal surface of metal oxide [1-5]. One of the reasons why oxide is disregarded so far in surface chemistry is the inertia on stable low-index planes having large band gaps. Recently several investigations is revealing reactivity on defect sites over metal oxide, such as steps, corners and oxygen vacancies. Kurtz and Henrich [6,7] ascribed the dissociation of water to oxygen vacancy with less screened Ti^{3+} pair on TiO_2. Enhanced reactivity of regular facets on an annealed MgO(111) surface is mentioned in Chapter 3.

Another path to highlight chemical aspects on metal oxide is decoration with metal adatoms. Alkali metal atoms deposited on transition metals give pronounced promotion effects on surface reaction of chemisorbed species [8]. Na additives on MgO powder exhibits a strong basic catalysis called "super-base" [9]. Charge transfer from alkali adatom to substrate plays an important role in those promotion effects. In this chapter, physical properties of Na adatoms on TiO_2(110) surface are examined as a prototype of alkali/metal-oxide interface. Effect of step structure in interaction with the adatoms is also discussed on TiO_2(441) surface. Chemical aspects of the modified surfaces are dealt with in Chapter 7 on the basis of the physical properties here.

6-3. Experimental

The experiments were carried out in an ultrahigh vacuum chamber (VG-ESCALAB). A (110) and a (441) wafers of rutile were prepared through sputter-anneal cycles as described in Chapter 4. Electron spectrum was measured along the (110) direction. The binding energy in XPS excited by Mg-Kα radiation was referred to the lattice O(1s) level of 530.3 eV as an internal reference. Density of Na adatoms was estimated on the normalized intensity of Na(1s) emission, I_{Na}, which was defined as a ratio in

intensity: Na(1s)/O(1s). Relative cross section, escape depth and transmission of the analyzer were considered. Carbon density in a (2x1)-formate overlayer is successfully determined in a this way in Chapter 5. The uncertainty in density is presumed to be $2x10^{18}$ m^{-2}. Work function was measured from cutoff in HeI UPS [10]. LEED was observed with a four grid optics. Electron energy loss spectrum (EELS) was excited with primary electrons from the gun in the optics. The primary energy in EELS was fixed at 100 eV and the FWHM of the elastic peak was 1.1 eV.

Atomic Na was deposited on the sample wafers at 298 K using a commercial source (SAES Getters). Pressure was maintained below $5x10^{-10}$ Torr during deposition.

6.4. Results

6.4.1. Na adatoms on (110) surface

The growth mode of Na adatoms was monitored by Na(1s) emission. The normalized intensity, I_{Na}, is plotted with the exposure time in Fig.6-1 (filled circle). There is a clear break at 38 min, followed by a gentle slope. They demonstrate an atomic layer growth before the break [11]. The first monolayer is completed at the break with I_{Na}=1.2. The surface density of the adatoms is estimated to be $1x10^{19}$ m^{-2} at 1 ML. The binding energy of Na(1s) plotted together in Fig.6-1 (open circle) decreases by 0.9 eV in layer growth region to almost saturate after the break. Na(1s) emission maintained a symmetric shape with increasing FWHM from 1.8 to 2.3 eV.

Na $KL_{2,3}L_{2,3}$ (^1D) emission in XAES was also monitored. In contrast to Na(1s) emission, the KLL emission kept kinetic energy at 989.5 eV in the layer growth region, followed by a shift to greater kinetic energy with broadening. Figure 6-2 illustrates Na KLL spectra normalized to an equal height. The shift with broadening result from the evolution of a new peak around 991.5 eV originated in Na multilayers.

Figure 6-3 shows Ti(2p) emission. A shoulder grew in low binding energy side on curve b at 1.7 ML. A difference spectrum

(curve c) reveals a new peak at 457.4 eV. It is assigned to Ti^{3+} species [12], indicating the reduction of Ti^{4+} cations by Na adatoms.

Figure 6-4 shows HeI UPS spectra at various stages of deposition and also the difference spectra between surfaces with and without Na adatoms. Since there was a band bending as elucidated later, the spectra were aligned to the peak position of the main valence band, E_v, and then differenciated. New peaks in the difference spectra are classified into two groups. Group I consists of three peaks at 4.4, 7.5-6.2 and 9.8 eV, which are observed even at lowest coverage and gradually increases with coverage, accompanied with a shift of the middle peak. They are quite similar to the spectrum on Na overlayer deposited on a faceted MgO(111) surface in Chapter 3, which is inserted in Fig.6-4. The other peak at 1.0 eV is group II. Note that it was not detected below 0.2 ML.

The peak height of group II, h_{II}, starts to increase at 0.2 ML and saturates at 0.6 ML in Fig.6-5 (open circle). Filled circle represents work function, ϕ. A large decrease by 3.4 eV was observed in the layer growth region to be saturated at 2.0 eV. The decrease in work function is related to the dipole induced by the adatoms. Half-filled circle indicates the degree of band bending, E_{bend}, which is evaluated from the shift in E_v with respect to the Fermi level, E_F. A positive E_{bend} value corresponds to a downward shift of E_v relative to the Fermi level and hence demonstrates a downward band bending toward the surface. E_{bend} in Fig.6-5 is saturated at 1.1 eV when the first layer is completed.

EEL spectra on clean and Na-deposited surfaces are shown in Fig.6-6. Clean surface (curve a) gives peaks at 6.4, 10.4 and 13.6 eV which are assigned to interband transitions in an early work [13]. These peaks are attenuated at 0.8 ML (curve b), while a new peak appeared at 1.6 eV. There are three peaks at 1.5, 6 and 10 eV remained at 1.7 ML, giving a shoulder at 3.5 eV (curve c).

A c(4x2) pattern was observed at 0.3-0.7 ML with regularly extincted spots was observed at I_{Na}=0.4-0.8. Figure 6-7 illus-

trates the extinction. The extinction reflects the structure factor in the c(4x2) unit cell, which will be discussed in 6.5.2. The c(4x2) diffraction was followed by a diffuse (1x1) pattern when deposition was continued.

6.4.2. Na adatoms on stepped (441) surface

Almost the same behavior as on TiO_2(110) was observed on a stepped TiO_2(441) surface. The evolution of Na(1s) peak is shown in Fig.6-8, where the first layer is completed at I_{Na}=1.0. Na KLL, HeI UPS and EELS gave spectra similar to those on Na/TiO_2(110). Work function, the intensity of group II emission and E_{bond} are plotted in Fig.6-9. The Work function was reduced by 2.3 eV, which decrease is smaller by 1.1 eV than that on the (110) surface. No new spot was observed in LEED on (441) surface during deposition; the background increased in intensity and diffuse (1x1) spots remained up to 1 ML.

6.5. Discussion

6.5.1. Electronic states on modified (110) surface

Na adatoms interact mainly with surface oxygen anions below 0.3 ML, because the group I emission is quite similar to the valence spectrum on Na overlayer deposited on a faceted MgO(111) as shown in Fig.6-4. No interaction of Na adatom with Mg^{2+} cation is detected in that case. The group I is regarded as a fingerprint of Na adatoms interacting with oxygen anions on metal oxide. The shift in Na(1s) binding energy of 0.9 eV also compares to the oxidation shift of 0.7 eV [20]. Additionally, the observed kinetic energy of Na KLL emission at 989.5 eV is close to the reported value on Na_2O, 990.0 eV [20]. These assignments support Na-O bonding and partial ionization of the adatoms below 0.3 ML.

The decrease in work function in Fig.6-5 is ascribed to electron transfer from adatoms into the substrate. The initial slope of the reduction corresponds to a dipole moment of

4.3 Debye per Na adatom. The induced large dipole leads to dispersed structure of Na adatoms due to mutual repulsion. A similar decrease in work function was reported on Cs deposition on ZnO powder [21].

Direct overlap of Na(3s) wavefunctions between neighboring adatoms plays an important role at higher coverage. The decrease in work function and Na(1s) binding energy is almost saturated above 0.3 ML, indicating that no more charge transfer takes place. This implies that the cohesive interaction between Na adatoms avoids the charge transfer. A similar picture has been drawn on K/Cu(001) [15], where two-dimensional condensation of potassium adatoms is accompanied with the band formation of K(4s) level.

Dense adlayer give a pronounced influence on the valence of titanium cations; all the five-fold coordinated Ti^{4+} cations are reduced to Ti^{3+} state. The transferred electrons from the adatoms cause a downward band bending as much as 1.1 eV at 1 ML. The Fermi level thus rises up relative to the bands near surface. If the rising Fermi level crosses an unfilled state, electrons move into that state. According to a DV-Xα calculation by Tsukada et al. [22], the lowest unfilled state on TiO_2(110), A', is localized on the five-fold coordinated Ti^{4+} cations. Electron transfer to A' state hence results in the selective reduction of the five-fold coordinated cations. The observed E_{bond} is large enough to raise the Fermi level above A' state, since the Fermi level is located just below the A' state on TiO_2(110). The group II emission is located at the predicted position of A' state. Consequently, the group II emission is assigned to the occupied A' state. The evolution of group II corresponds to the reduction of five-fold Ti^{4+} cations. A new peak in Ti(2p) region assigned to Ti^{3+} quantitatively supports the selective reduction. The intensity of Ti^{3+} emission in Fig.6-3c was 10% of that of Ti^{4+} in Fig6-3a. Density of Ti^{3+} is thus estimated to be 5.3×10^{18} m^{-2}, considering the escape depth of photoelectron. This is in a good agreement with the density of the five-fold coordinated Ti cations, 5.21×10^{18} m^{-2}.

The observed band bending is enough to reduce the

five-fold surface cations, but cannot reduce six-fold coordinated cations. The next lowest unfilled state, A, is located at least 2 eV upper than A' state [22], which is localized on six-fold coordinated cations and connected to the conduction band. Figure 6-10 illustrates the proposed picture on the band bending and the selective reduction of Ti^{4+} cations.

EELS spectra in Fig.6-5b and 6-5c give a peak at 1.6 eV; it is assigned to an interband transition from filled A' state to the conduction band. Ar^+-bombarded TiO_2 surface with Ti^{3+} species performs a similar peak [23]. An overlayer plasmon excitation was observed on one-dimensional potassium arrays on Si(001)-(2x1) [24]. One cannot distinguish a loss peak assignable to one-dimensional plasmon excitation in Fig.6-5.

Na adatoms affects surface electronic states on TiO_2(110) in a most drastic and well-controlled manner. Deposited Ni [25] and Pt [26] adatoms induce no reduction of Ti^{4+} cations. Titanium adatoms give a mixture of Ti^{4+}, Ti^{3+}, Ti^{2+} and Ti^0 species on TiO_2(110) [27]. Na adatoms controls the oxidation state of surface cations through the position of the Fermi level. It is expected that these modified surfaces are promoted in chemical reactivity. Chapter 7 deals with the reactivity on Na-modified TiO_2(110) surfaces.

Na overlayers above 1 ML gain metallic property. Surface plasmon losses on Na islands were observed in EELS and KLL spectra. An EELS peak at 3.5 eV in Fig.6-6c and a tail in KLL emission in Fig.6-2d are consistent to the reported loss of 4.1 eV on metallic sodium [20]. On the other hand, multilayered islands give Na KLL emission at 991.5 eV, suggesting that the islands are not equivalent to Na bulk. Na_2O and metallic Na gives emission at 990.0 and 994.5 eV, respectively [20]. The observed value is near the latter.

6.5.2. Structure of Na overlayer on (110) surface

TiO_2(110) surface has an open structure as shown in Fig.6-11a; oxygen anions form one-dimensional rows along the [001] direction, to which the interaction with the adatoms are ascribed. Na adatoms form an atomic layer on TiO_2(110) as demonstrated in Fig.6-1. Deposited Na atoms can be atomically dispersed without long range order below the critical coverage for the c(4x2) order, because the charge transfer and the resultant dipole dominate the adatoms. Dispersed Cs adatoms form a $(\sqrt{3}x\sqrt{3})$ structure on $ZnO(000\bar{1})$-O [14].

A c(4x2) pattern was observed with regular extinction at coverages centered at 0.5 ML. The structure factor of the c(4x2) unit cell is deduced on the regular extinction. A periodic arrangement of two equivalent scatterers in Fig.6-12 answers the observed extinction rule. Na density was estimated to be $5x10^{18}$ m^{-2} at 0.5 ML. Consequently, a model illustrated in Fig.6-11b is proposed for the TiO_2(110)-c(4x2)-Na overlayer. It is based on the extinction, the estimated density of Na and the assumption that Na adatoms contact as many oxygen anions as possible. The unit of the proposed structure consists of four sodium atoms and two protruded oxygen anions, and thus named as "Na_2O-dimer". An oxygen anion on ridge has two Na adatoms, while each Na adatom is coordinated by two protruded and one basal oxygen anions.

What is the origin of the aggregation into "Na_2O-dimer" unit against the dipole repulsion? Cohesive interaction between Na adatoms plays a role. Direct overlap of Na(3s) wave functions between neighboring adatoms avoids the charge transfer, as discussed in 6.5.1. A similar two-dimensional condensation of potassium adatoms is ascribed to the band formation of K(4s) level on Cu(100) [15].

The c(4x2) pattern merged into a diffuse (1x1) at 1 ML. Figure 6-11c shows a proposed structure on the completed monolayer; the "Na_2O-dimer" units cover the substrate in a (1x1) periodicity. The separation between the ridges is 64.9 pm on TiO_2(110), which is large enough for two Na adatoms to sit, considering contraction of the adatoms. Sodium has an atomic radius of 18.3 pm in metal. Partial ionization and polarization of semi-core orbitals [16] contract the radius. A TEM study on impregnated Rh/TiO_2 catalysts [17] reported Rh arrays along the [001] direction on (110) planes. A model was proposed for

the TEM image [18], in which Rh adatoms are drawn up in line on both sides of oxygen anions on the ridges. That model is compatible with the model here. Metal adatoms seem to form one dimensional arrays on TiO_2(110).

The proposed model at 1 ML is very different from the structure in Na_2O bulk. An idearlly truncated (100) surface of Na_2O consists of Na_2O units with square periodicity. The separation of the units, however, 39.2 pm [19], being nearly half of the distance along [1$\bar{1}$0] direction on the model.

Na adatoms form atomic layers on a faceted MgO(111), as described in Chapter 3. The ridges on TiO_2(110) corresponds to coordinatively unsaturated edge sites on the faceted MgO(111). The above discussion gives more detailed information on geometry of Na adatoms bound to active sites on metal oxide.

6.5.3. Na adatoms on stepped (441) surface

TiO_2(441) surface interacts with Na adatoms in a similar manner to (110) surface. The picture drawn on (110) is slightly affected by the steps on (441) surface. Since (110) terrace on (441) surface is too narrow to perform a c(4x2) order, no extra spot was observed in LEED. However, it is reasonable to expect the "Na_2O" units on the terraces. The fact that the decrease in the work function is smaller by 1.0 eV than that on the (110) surface suggests a smaller charge transfer on the step sites.

6.6. Conclusions

Sodium adatoms form an atomic layer interacting with protruded oxygen anions on TiO_2(110). Na adatoms give their 3s electrons to the substrate, leading to a downward band bending toward the surface. When the rising Fermi level crosses an unfilled surface state localized on five-fold coordinated Ti^{4+} cations, the transferred electrons reduce the cations to Ti^{3+} state. A c(4x2) structure is observed at 0.5 ML, for which a "Na_2O-dimer" model is proposed. The "Na_2O" units is proposed to merge into one-dimensional arrays along the [001] direction at 1 ML. Almost the same picture is drawn on stepped TiO_2(441) surface.

6.7. References

1. V.E.Henrich, Progr.Surf.Sci.9(1979)143.
2. V.E.Henrich, Progr.Surf.Sci.14(1983)175.
3. W.Göpel, Progr.Surf.Sci.20(1985)9.
4. M.Tsukada, H.Adachi and C.Satoko,Progr.Surf.Sci.9(1979)143.
5. G.Heiland and H.Lüth, in: The Chemical Physics of Solid Surfaces and Heterogeneous Catalysis, vol.3, Elsevier,Amsterdam(1984),chap.4.
6. R.L.Kurtz and V.E.Henrich, Phys.Rev.B26(1982)6682.
7. V.E.Henrich, Rept.Prog.Phys.48(1985)1481.
8. H.P.Bonzel, J.Vac.Sci.Technol.A2(1984)866.
9. J.Kijenski and S.Marinowski, Bull.Acad.Polonaise Sci.25(1977)428.
10. S.Evans, Chem.Phys.Lett.23(1973)134.
11. G.E.Rhead, J.Vac.Sci.Tecnol.13(1976)603
12. W.Göpel, J.A.Anderson, D.Frankel, M.Jaenig, K.Phillips, J.A.Schafer and G.Rocker, Surf.Sci.139(1984)333.
13. W.J.Lo, Y.W.Chung and G.A.Somorjai, Surf.Sci.71(1978)199.
14. R.Leysen, B.J.Hopkins and P.A.Taylor, J.Phys.C8(1975)907.
15. T.Aruga, H.Tochihara and Y.Murata, Phys.Rev.B34(1986)8237.
16. E.Wimmer, Surf.Sci.134(1983)L487.
17. S.Fuentes, A.Vázquez, J.G.Perez and M.J.Yacamán, J.Catal.99(1986)492.
18. H.R.Sadeghi, D.E.Resasco, V.E.Henrich and G.L.Haller, J.Catal.104(1987)252.
19. R.W.G.Wyckoff, in: Crystal Structure 2nd Ed, vol.1, Whiley, New York(1963)
20. A.Barrie and F.J.Street, J.Electrn.Spectrosc.Related Phenomena 7(1975)1.
21. R.A.Powell and W.E.Spicer, J.Appl.Phys.48(1977)4311
22. M.Tsukada, C.Satoko and H.Adachi, J.Phys.Soc.Jpn.47(1979)1610.
23. Y.W.Chung, W.J.Lo and G.A.Somorjai, Surf.Sci.64(1977)588.
24. T.Aruga, H.Tochihara and Y.Murata, Phys.Rev.Lett.53(1984)372.

25. C.C.Kao, S.C.Tsai, M.K.Bahl, Y.W.Chung and W.J.Lo, Surf.Sci.95(1980)1.
26. Y.M.Sun, D.N.Belton and J.M.White, J.Phys.Chem.90(1986)5178.
27. G.Rocker and W.Göpel, Surf.Sci.181(1987)530.

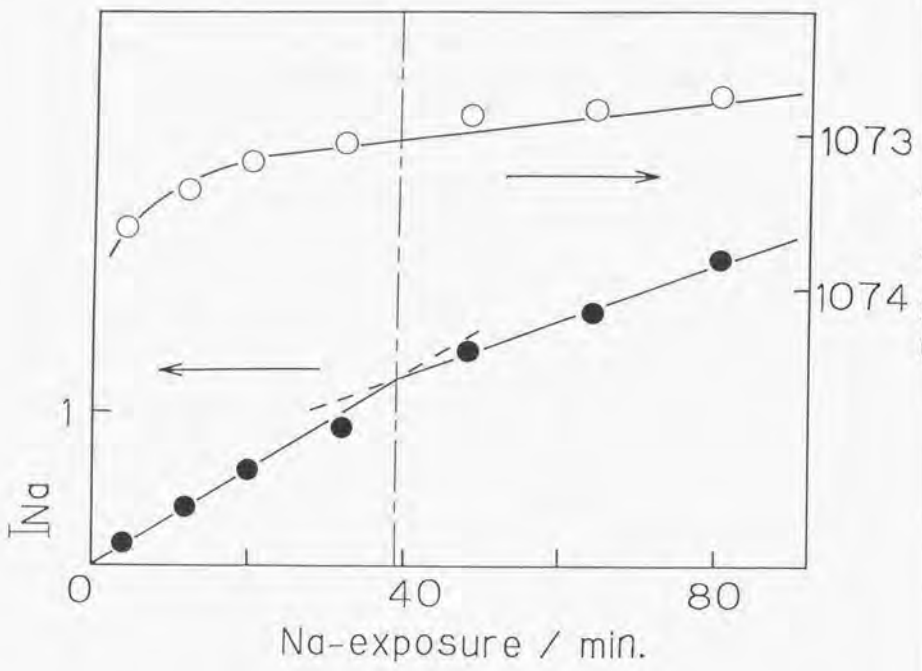

Fig.6-1. The normalized intensity and the binding energy of Na(1s) level with exposure time of Na on TiO_2(110). Filled and open circles represent the intensity and the binding energy, respectively.

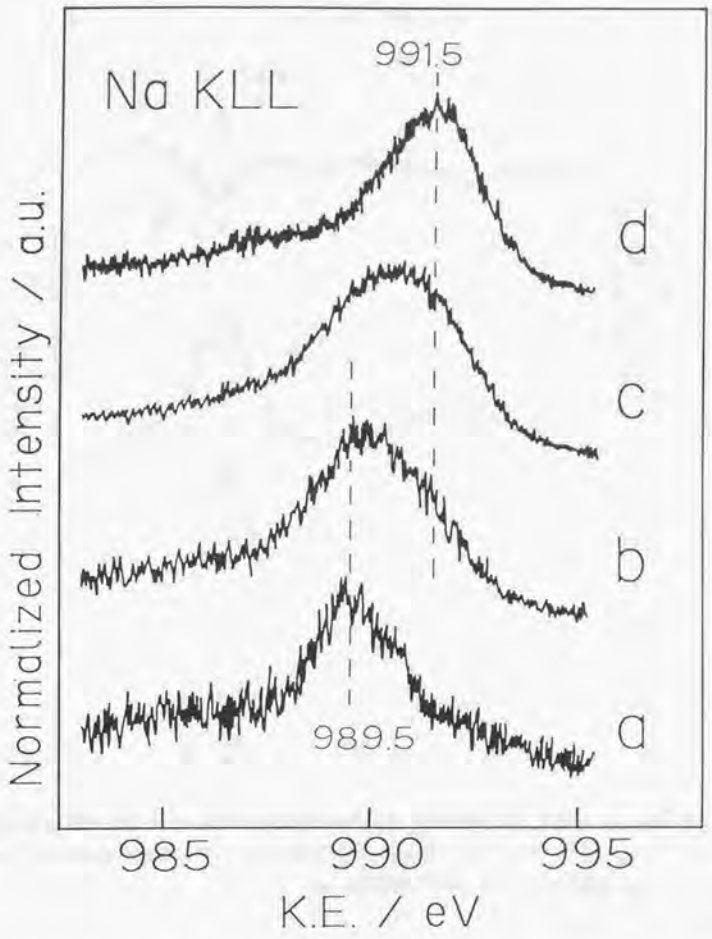

Fig.6-2. Evolution of Na KLL peak on TiO_2(110) at (a): 0.5 ML, (b): 1.0 ML, (c): 1.5 ML, and (d): 2.6 ML.

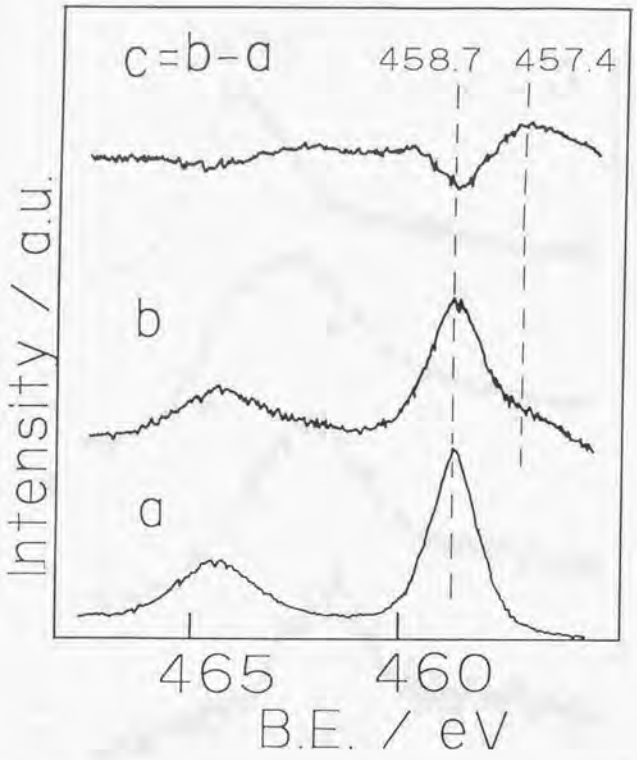

Fig.6-3. Ti(2p) emission on Na/TiO_2(110); (a):clean surface, (b): θ_{Na}=1.7 ML. (c)=(b)-(a). Twin peaks are due to spin-orbit splitting.

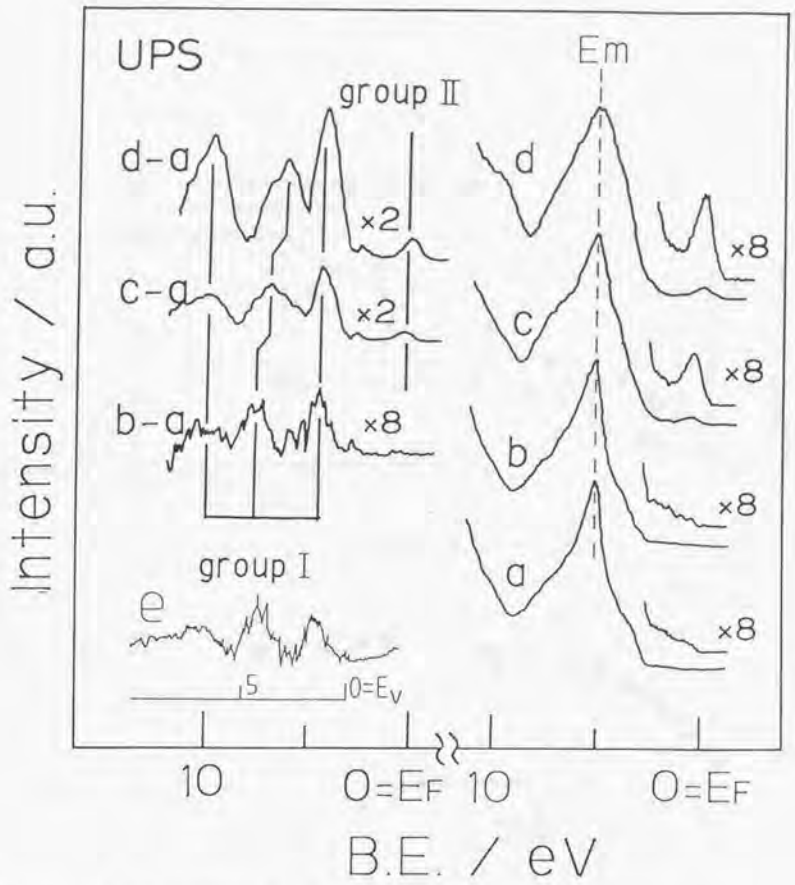

Fig.6-4. HeI UPS spectra at various stages of deposition; (a): clean surface, (b): θ_{Na}=0.08 ML, (c): θ_{Na}=0.3 ML and (d): θ_{Na}=0.9 ML. The origin of binding energy is the Fermi level on the clean surface. The spectra on Na-covered surfaces are shifted to align E_a by 0.1, 0.4 and 1.0 eV, respectively. (e): HeII UPS spectrum on Na overlayers deposited on a faceted MgO(111) surface whose binding energy is referred to the valence band edge E_v.

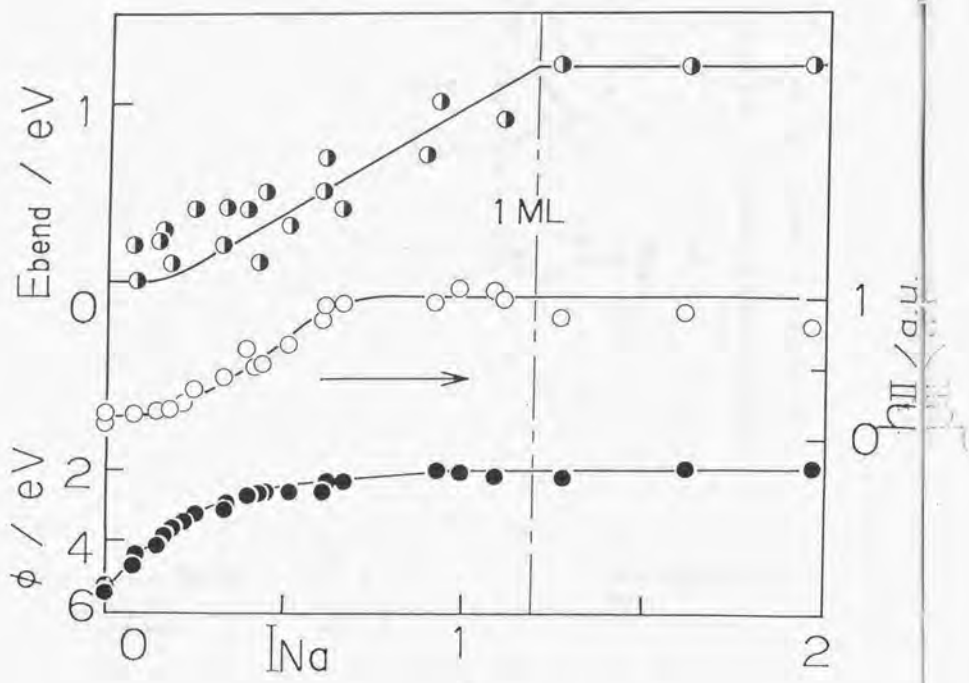

Fig.6-5. Evolution of ϕ, E_{bend} and h_{II} with I_{Na} on TiO_2(110). Full, open and half-filled circles represent ϕ, E_{bend} and h_{II}, respectively. The broken line indicates the completion of monolayer.

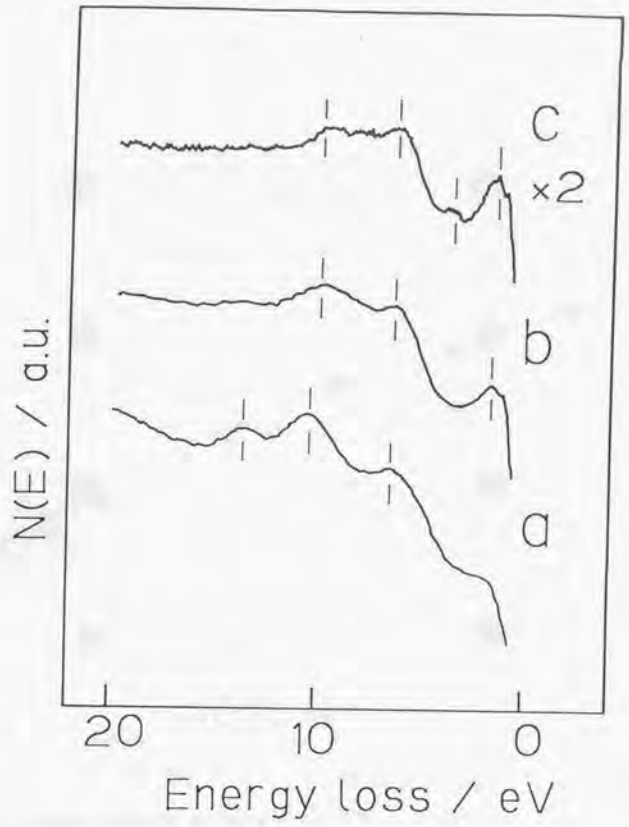

Fig.6-6. EELS spectra on Na/TiO_2(110); (a): clean surface, (b): θ_{Na}=0.8 ML, and (c): θ_{Na}=1.7 ML.

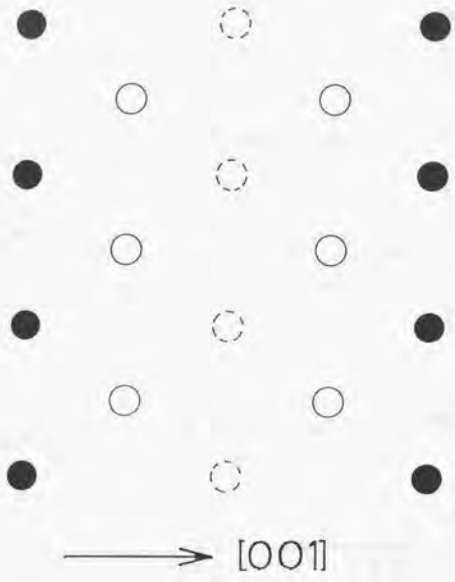

Fig.6-7. A schematic illustration of a c(4x2) pattern on $Na/TiO_2(110)$ with θ_{Na}=0.6 ML. Filled circle is fundamental spot. Open and broken circles represent fractional spots allowed and extincted, respectively.

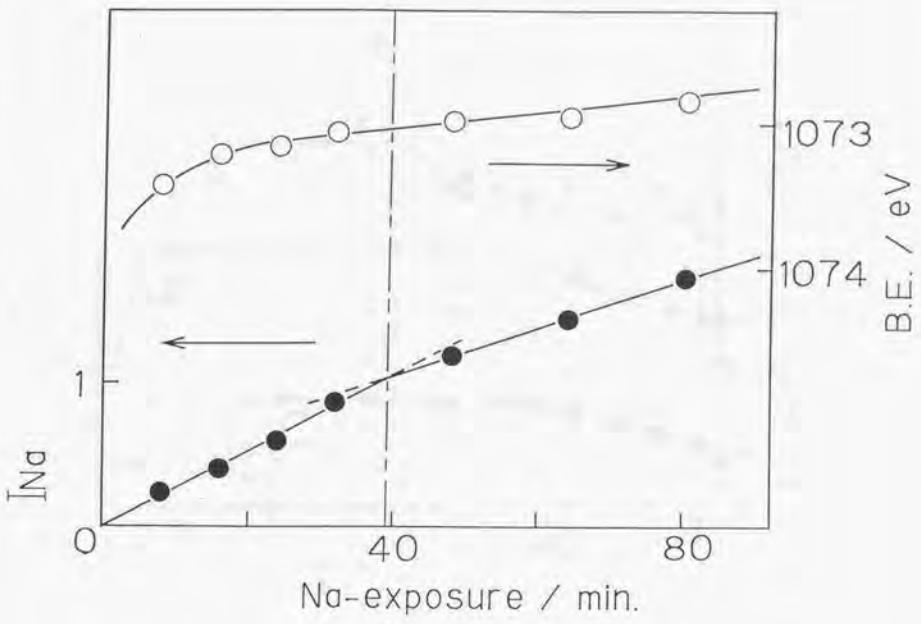

Fig.6-8. The normalized intensity I_{Na} and the binding energy of Na(1s) with the exposure time on $TiO_2(441)$.

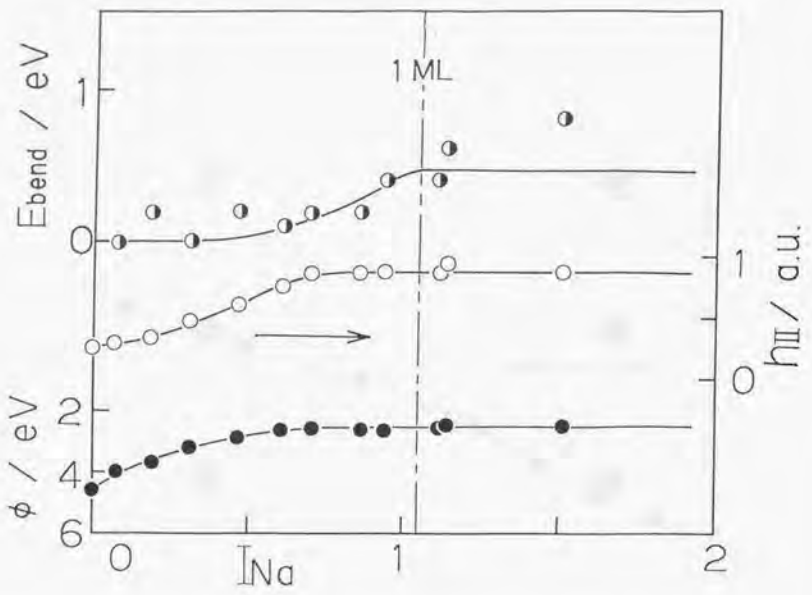

Fig.6-9. Evolution of ϕ, E_{bend} and h_{II} with I_{Na} on TiO_2(441). They are represented by full, open and half-filled circles, respectively.

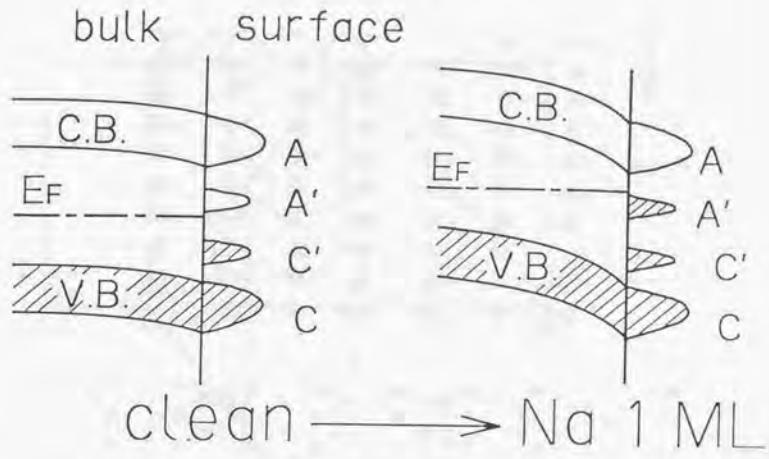

Fig.6-10. An illustration for band bending and reduction at surface with Na adatoms. Hatched states are occupied. A, A', C and C' are the predicted states in a DV-Xα calculation [22]. Prime indicates surface origin.

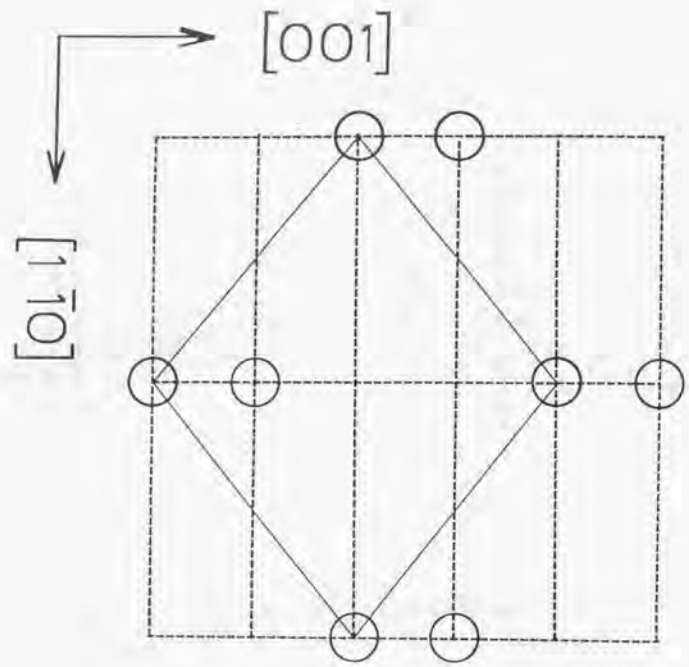

Fig.6-11. Top views of the proposed models for Na adatoms on TiO_2(110); (a): clean surface, (b): "Na_2O-dimer" structure at 0.5 ML in the extincted c(4x2) symmetry, and (c): 1 ML in a (1x1) order. Filled, open and hatched circles represent Ti, O and Na atoms, respectively.

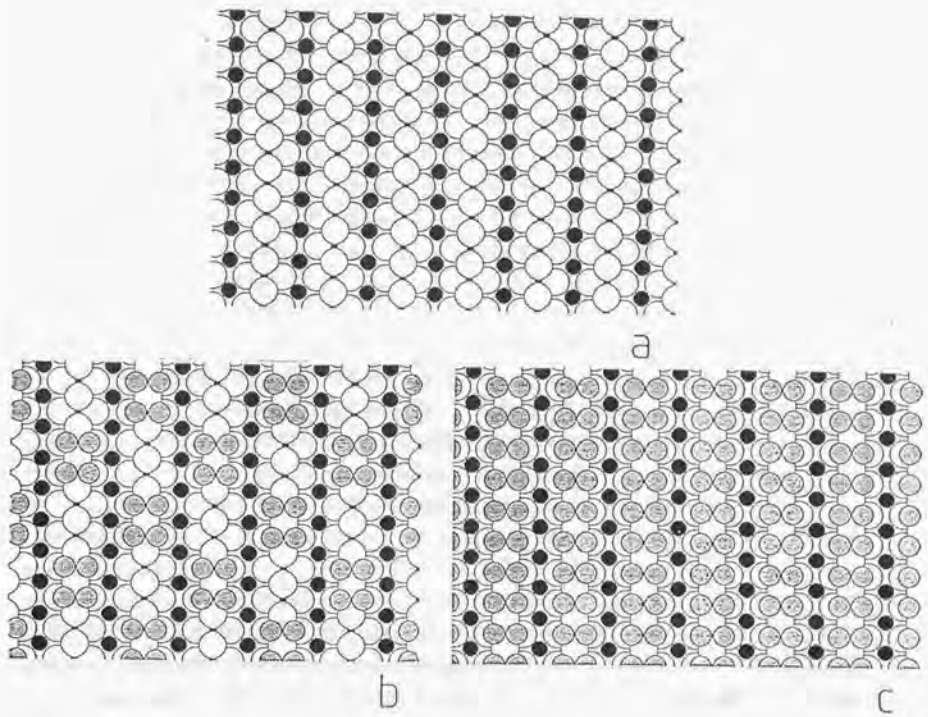

Fig.6-12. The distribution of scatterers deduced on the observed extinction in the c(4x2) diffraction. Solid and broken line show the c(4x2) and the (1x1) unit cells. Open circle represents scatterer.

Chapter 7

Active structure for chemisorption of CO_2 and NO on TiO_2(110) surfaces modified with Na adatoms

7.1. Abstract

XPS and UPS studies show that Na adatoms on a rutile TiO_2(110) surface promote the adsorption of carbon dioxide and nitric monoxide forming carbonate and nitride, respectively. The amount of adsorbed CO_2 increases with Na coverage in a S-shape curve, where a critical Na coverage of 0.3 ML is observed. The threshold coincides with the onset of a c(4x2) structure composed of ordered "Na_2O-dimer"s, demonstrating that basic reactivity of the oxygen anions on TiO_2(110) is enhanced by the "Na_2O-dimer" ensemble of four Na adatoms. Single adatoms of Na play a negligible role in the basic promotion. In contrast, NO decomposes on Ti^{3+} cation reduced by Na adatoms. The oxidation state of Ti cation dominates the decomposition process of NO.

7.2. Introduction

Alkali additives play an important role in chemisorption and catalysis over solid surface. Alkali adatom has been an intense subject in surface science on transition metals, in connection with their catalytic promotion [1]. On the other hand, alkali dopants on metal oxide catalysts remarkably enhance basic character on the catalysts. Polycrystalline MgO with sodium additives exhibits so strong basic catalysis that is called "super-base" [2]. Recently, oxidative dimerization of methane through a methyl radical intermediate was reported on alkali earth oxide catalysts promoted by alkali additives [3].

A faceted MgO(111) interacts with Na adatoms, as discussed in Chapter 3. The interaction is ascribed to coordinatively unsaturated edge-sites on microfacets. Further, Na adatoms affect surface states on TiO_2(110) through a large electron transfer, as described in Chapter 6. A c(4x2) ordered structure is performed on Na/TiO_2(110) with 0.5 ML of Na adatoms.

Here, chemical properties on TiO_2(110) promoted by Na adatoms are examined in chemisorption of carbon dioxide and nitric monoxide. Remarkable enhancement in basic character and reducing ability are observed. The structure of active sites and the mechanism of the promotion to the reactants are discussed.

7.3. Experimental

The experiments were carried out in an ultrahigh vacuum chamber (VG-ESCALAB) which has facilities for XPS, UPS and LEED measurements. The binding energy in XPS was referred to the lattice O(1s) level of 530.3 eV as an internal reference. Mg-Kα radiation was used except for C(1s) emission, for which Al-Kα line was employed to avoid superposition on Na KLL Auger emission.

A clean TiO_2(110) surface was prepared by argon sputtering and annealing up to 900 K under UHV. Atomic Na was deposited at 300 K maintaining pressure below 5×10^{-10} Torr. The coverage of Na, θ_{Na}, was determined on an uptake plot. The intensity of

Na(1s) emission increased with exposure time of Na vapor exhibiting two straight lines with a clear break. The first monolayer (θ_{Na}=1 ML) is defined at the break [4]. See Chapter 6 in detail. Reactant gases of research grade were further purified by trap-thaw cycles and introduced onto the crystal through a capillary doser.

7.4. Results

7.4.1. Chemisorption of CO_2

Exposure of Na-deposited TiO_2(110) surfaces to 10^3 L of CO_2 at 300 K led to the formation of carbonate, while no adsorption was observed on a clean TiO_2(110) surface without Na adatoms. A peak in C(1s) and a shoulder in O(1s) appeared upon CO_2 exposure as typically shown in Fig.7-1. The binding energy is listed in Table 7-1 together with reference species. The observed values are characteristic for carbonate, CO_3^{2-}.

HeI UPS difference spectra upon CO_2 exposure at different Na coverages are shown in Fig.7-2. Curves 2b and 2c are characterized by three peaks at 6.5, 11 and 13 eV assignable to carbonate [5]. Another peak at 4 eV may reflect distortion in the O(2p) valence bands affected by the adsorption of CO_2, which lies at 4-7 eV on the substrates. A reference spectrum on CO_3^{2-}/MgO(111) is inserted as curve 2d. No definite peak was, however, observed in curve 2a recorded on a surface with θ_{Na}=0.2 ML. The disparity between curves 2a (θ_{Na}=0.2 ML) and 2b (θ_{Na}=0.6 ML) suggests a threshold for the promotion.

The amount of carbonate was monitored with the intensity of C(1s) emission. The intensity is plotted with the coverage in Fig.7-3. No C(1s) peak was detected below 0.3 ML in accordance with the results of UPS, demonstrating a threshold for carbonate formation. The adsorption of CO_2 nearly is saturated above 1 ML.

The adsorption of CO_2 increased the background in LEED without extra spots.

7.4.2. Decomposition of NO

Exposure of Na/TiO_2(110) surfaces to 10^3 L of NO at 300 K gave a peak at 396.2 eV in N(1s) region. Table 7-2 shows the binding energy in N(1s) level of nitrogen-containing reference species. The observed value corresponds to nitride compounds. HeI UPS difference spectra upon NO adsorption on Na/TiO_2(110) surfaces are shown in Fig.7-4. They exhibit a singlet peak at 4 eV; it is assigned to N(2p) and O(2p) of nitride and oxide. No peak attributable to molecular adsorbates was observed. The results indicate the dissociative adsorption of NO to form nitride on Na/TiO_2(110) surfaces.

The amount of nitride was monitored with the intensity of N(1s) emission. It is plotted with the coverage of Na in Fig.7-5, exhibiting again a S-shape curve with a threshold of 0.3 ML. N(1s) emission was not detected on a clean TiO_2(110) surface. No extra spot was observed in LEED upon NO exposure.

7.4.3. Adsorption of CO_2 and NO on a TiO_2(110) surface reduced by Ar^+ sputtering

Argon ions sputter off oxygen atoms on TiO_2(110) surface to reduce Ti cations into Ti^{3+} state [6]. The reactants were admitted on a TiO_2(110) reduced by argon sputtering at 3 keV and 15 μA for 3 min. Contribution of reduced cations is examined on a Na-free condition. A prior sputtering could not lead to adsorption of CO_2 at all, whereas nitric monoxide was decomposed into nitride on the sputtered surface. Identical spectra of adsorbed nitride were observed on the sputtered and Na-deposited surfaces, as shown in Fig.7-4 and Table 7-2.

7.5. Discussion

7.5.1. Structure of Na/TiO_2(110)

The geometry and electronic states of Na adatoms on TiO_2(110)

are described in Chapter 6: Na adatoms form a atomic layer interacting with oxygen anions on ridges of the substrate. The bonding of Na adatoms with the anions causes an electron transfer into the substrate. Work function decreases as much as 3.5 eV at 1 ML. Dipole repulsion dominates the overlayers and hence prevents the adatoms from clustering at the low coverage limit. A c(4x2) ordered phase appears among 0.3-0.8 ML. Figure 7-6a shows a model for the c(4x2) structure composed of ordered "Na_2O-dimer"s. A "Na_2O-dimer" unit is composed of four Na atoms and a protruded oxygen atom surrounded by them. The c(4x2) structure is completed at 0.5 ML. The "Na_2O" units merge into a uniform monolayer in (1x1) periodicity at 1 ML as shown in Fig.7-6b. The transferred charge causes a downward band bending and reduces titanium cations to Ti^{3+} state.

7.5.2. Promotion to CO_2 chemisorption

Carbon dioxide was adsorbed neither on a TiO_2(110) surface nor on the reduced surface by argon sputtering. Na adatoms play an essential role in the promotion to CO_2. Carbon dioxide has been used as a gaseous indicator for basic property on solid surface; the amount of irreversibly adsorbed CO_2 is a scale of the amount of basic sites on metal oxide surface [8]. The present results show a negligible basic property on a TiO_2(110) surface.

The amount of CO_2 adsorbed was not proportional to the coverage of Na adatoms as shown in Fig.7-2 and Fig.7-3. The adatoms cannot promote the reactive adsorption below a threshold coverage of 0.3 ML. The threshold coincides with the onset of the c(4x2) ordering in LEED. It is hence demonstrated that the "Na_2O-dimer" ensemble is a minimal unit for CO_2 chemisorption. Single adatoms, which must be majority at the low coverage limit, cannot promote the reactive adsorption.

The XPS and UPS spectra reveal that CO_2 is adsorbed to form carbonate on Na/TiO_2. There are three possible pathways for the formation of carbonate from carbon dioxide. The first mechanism is a nucleophilic attack of promoted oxygen anion on the

substrate to the carbon atom in CO_2; this is an acid-base reaction. The second possibility is the disproportionation of CO_2 on the Na ensembles. Carbon dioxide reacts with lithium atoms in matrix to form lithium oxalate, $Li_2C_2O_4$, through a radical intermediate, CO_2^-. Lithium oxalate decomposes into lithium carbonate with heating around 600 K [10]. Disproportionation is, however, ruled out in the present case, since carbonate was detected even at 300 K on Na/TiO_2. The last possibility is direct contribution of Ti^{3+} species. It is also excluded; no carbonate was observed on the TiO_2 surface reduced by argon sputtering. Consequently, it is concluded that the "Na_2O-dimer" ensemble of four Na atoms enhances the basic property of the surrounded oxygen anion on TiO_2(110).

There remains an open question on the mechanism of promotion by the "Na_2O-dimer" ensembles. Note that the Na overlayer composed of the "Na_2O-dimer"s is not equivalent to thin film of sodium oxide supported on TiO_2 substrate. Although a (100) surface of Na_2O crystal consists of Na_2O units with square periodicity, each unit is separated by 39.2 pm. The separation is almost half of the distance between the neighboring units on a Na/TiO_2(110) surface of θ_{Na}=1 ML. The "Na_2O-dimer" overlayer has a more open structure than crystalline sodium oxide. The binding energy in Na(1s) and the work function are saturated on the overlayers composed of "Na_2O-dimer"s to be close to those of metallic Na; there must be some direct overlap of Na(3s) levels. On the contrary, Na atoms in Na_2O crystal are completely oxidized. The c(4x2) overlayer is thus regarded as a new surface material with strong basic property. The basic character on a "Na_2O-dimer" unit is ascribed to promotion of oxygen anion affected by the surrounding ensemble of four Na adatoms. Nucleophilic activity of atomic oxygen adsorbed on Au(110) was reported; the weak bond of the oxygen adatoms on the substrate results in basic reactivity [11]. Vohs et al. studied abstraction reaction of proton from alkynes on ZnO(0001)-Zn, and pointed out covalent contribution in acid-base reaction on metal oxide [12]. Covalent and/or metallic properties of the Na ensemble may participate in the basic promotion on Na/TiO_2(110).

The amount of carbonaceous species continue to increase beyond 1 ML in Fig.7-3. Multilayered Na islands cannot block encounter of CO_2 to the reaction sites. Na islands also are not able to block SO_2 on Na/CaO(100) [9]. In addition, metallic sodium islands likely absorb CO_2 to form oxalate or CO_2^-.

7.5.3. Promotion to NO decomposition

Table 7-2 and Fig.7-4 demonstrate that nitric monoxide is dissociated to form nitride on $Na/TiO_2(110)$ surfaces. The reactive adsorption to form NO_2^- or NO_3^- is excluded. The nitride is bound with titanium cation, because sodium nitride would give a lower binding energy in N(1s); Na_3N is a typical ionic nitride, though there is no XPS results on sodium nitride to my knowledge. The dissociated oxygen atom of NO could be trapped on titanium and/or sodium atom.

A sputtered TiO_2 surface with reduced Ti^{3+} species dissociates NO to give compatible nitride upon. Ti^{3+} cations are capable of decomposition of NO on a Na-free condition. The occupation in Ti(3d) states is thus essential for the promotion to NO.

A shoulder peak at 5 eV in UPS of Fig.7-4a and 7-4b is likely due to deposited nitride affected by neighbouring Na atoms, because it was not observed on the sputtered $TiO_2(110)$ (curve c).

7.6. Conclusions

Na adatoms promote $TiO_2(110)$ surface to adsorb carbon dioxide to form carbonate. An ensemble of four Na adatoms activate the surrounded oxygen anion on the substrate. The promoted anion nucleophilically attacks a CO_2 molecule. Nitric monoxide is decomposed on Ti^{3+} cation to give nitride bound to titanium cation.

7.7. References

1. H.P.Bonzel, Surf.Sci.Rept.8(1987)43.
2. J.Kijenski and S.Marinowski, Bull.Acad.Polonaise Sci.25(1977)428.
3. C.-H.Lin, J.-X.Wang and J.H.Lunsford, J.Catal.111(1988)302.
4. G.E.Rhead, J.Vac.Sci.Technol.13(1976)603.
5. J.A.Conner, M.Considine and I.H.Hiller, J.Chem.Soc.Faraday Trans.II 74(1978)1285.
6. R.H.Tait and R.V.Kasowski, Phys.Rev.B20(1979)5178.
7. V.E.Henrich, G.Dresselhaus and H.J.Zeiger, Phys.Rev.Lett.36(1987)1335.
8. K.Tanabe, in: Solid Acid and Base Catalysts, Springer-Verlag, Berlin(1981), p.231.
9. Y.C.Lee, P.A.Montano and J.M.Cook, Surf.Sci.143(1984)423.
10. Z.H.Kafafi, R.H.Hauge, W.E.Billups and J.L.Margrave, J.Am.Chem.Soc.105(1983)3886.
11. D.A.Outka and R.J.Madix, Surf.Sci.179(1987)361.
12. J.M.Vohs and M.A.Barteau, J.Phys.Chem.91(1987)4766.
13. C.T.Au, W.Hirsch and W.Hirschwald, Surf.Sci.199(1988)507.
14. P.R.Norton and R.L.Tapping,Chem. Phys.Lett.38(1976)207.
15. C.T.Au, W.Hirsch and W.Hirschwald, Surf.Sci.197(1988)391.
16. U.Gelius, F.Heden, J.Hedman, B.J.Lindberg, R.Manne, R.Nordberg, C.Nordling and K.Siegbarn, Phys.Scripta 2(1970)70.
17. R.Nordberg, R.G.Albridge, T.Bergmark, U.Ericson, J.Hedman, C.Nordling, K.Siegbarn and B.J.Lindberg, Arkiv.für Kemi.28(1968)257.
18. F.G.Fuggle and D.Menzel, Surf.Sci.79(1979)1.
19. C.Egawa, S.Naito and K.Tamaru, Surf.Sci.138(1984)279.
20. M.Grunze, M.Golze, W.Hirschwald, H.-J.Freund, H.Pulm, U.Seip, M.C.Tsai, G.Ertl and J.Küppers, Phys.Rev.Lett.53(1984)850.
21. N.Kaufherr and D.Lichtman, J.Vac.Sci.Technol.A3(1985)1969.
22. X.D.Peng, D.S.Edwards and M.A.Barteau, Surf.Sci.195(1988)103.

Table7-1. Binding energy of carbonaceous adsorbates in XPS.

Species	C(1s)/eV	O(1s)/eV	Reference
CO_2/ZnO(10$\bar{1}$0)	291.8	535.1	13
CO_2/Cu	291.8	535.4	14
CO_2/Pt	291.1	534.5	14
CO_3^{2-}/ZnO(10$\bar{1}$0)	290.4	532.2	13
CO_3^{2-}/Na/TiO_2(110)	290.2	532.1	this work
CO_3^{2-}/MgO(111)	290.1	532.6	4
$ZnCO_3$[a]	289.8	532.0	15
Na_2CO_3[a]	289.7	-----	16
$Na_2(COO)_2$[a]	289.2	-----	16

[a] bulk

Table 7-2. Binding energy of nitrogen-containing adsorbates in XPS.

Species	N(1s)/eV	Reference
$NaNO_3$[a]	407.2	17
$NaNO_2$[a]	404.3	17
NO_2/W(100)	405.1-405.8	18
NO/Ru(001)	400.0	19
N_2/Fe(111)	399.0	20
N/Ru(001)	397.0	19
N/Fe(111)	397.0	20
TiN_x film	396.0-397.0	21
N/sp-TiO_2(110)[b]	396.4	this work
N/Na/TiO_2(110)	396.2	this work
Mg_3N_2 film	396.0	22

[a] bulk

[b] a sputtered TiO_2(110).

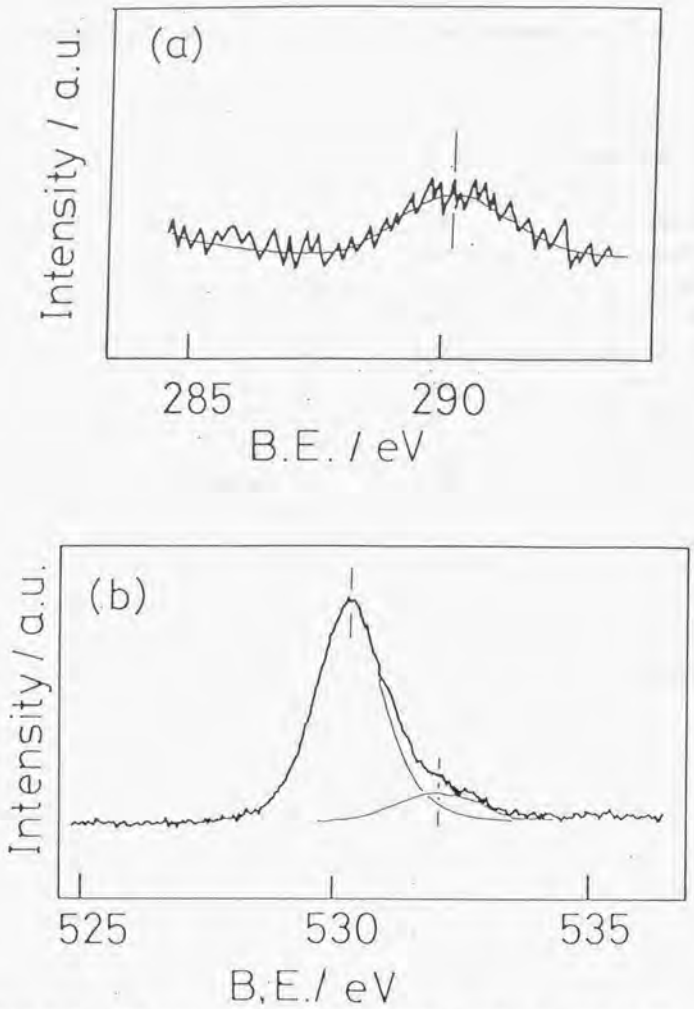

Fig.7-1. XPS spectra on a TiO_2(110) surface with 1 ML Na subsequently exposed to 10^3 L CO_2. (a): C(1s) and (b): O(1s) region

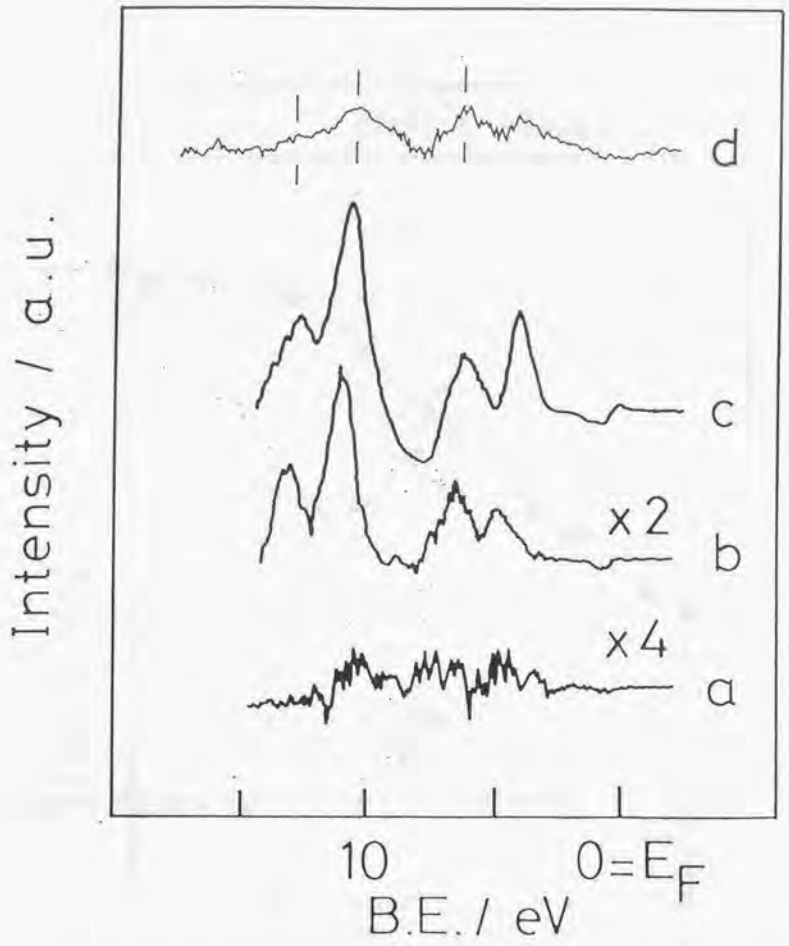

Fig.7-2. HeI UPS difference spectra upon CO_2 exposure on Na/TiO_2(110) with (a): θ_{Na}=0.2 ML, (b): 0.6 ML and (c): 1.4 ML. (d): a reference spectrum of CO_3^{2-}/MgO(111).

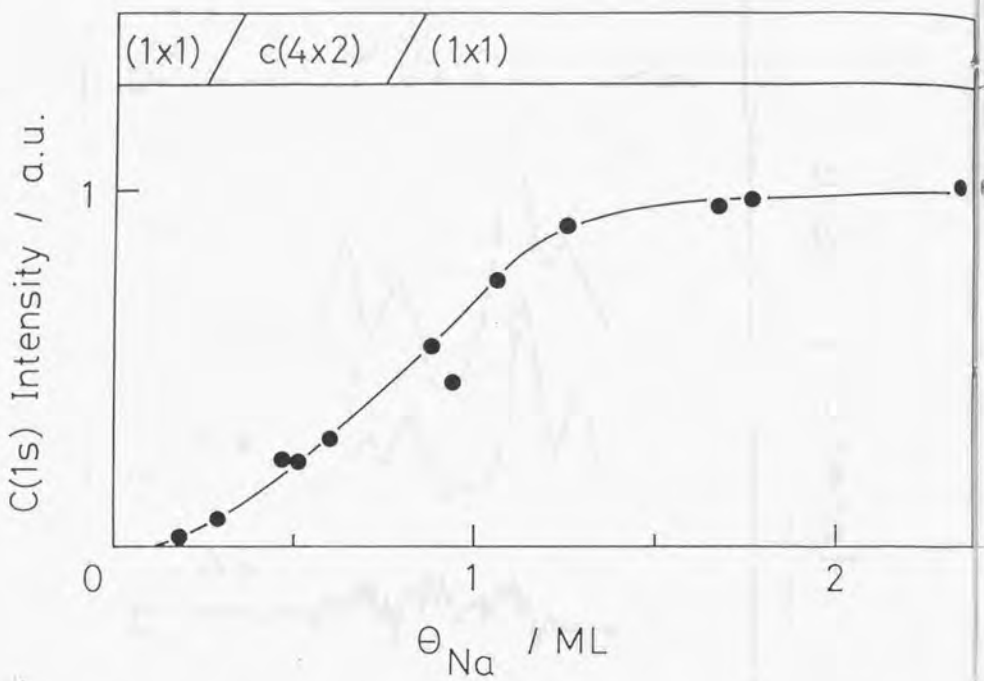

Fig.7-3. The intensity of C(1s) emission with the coverage of Na

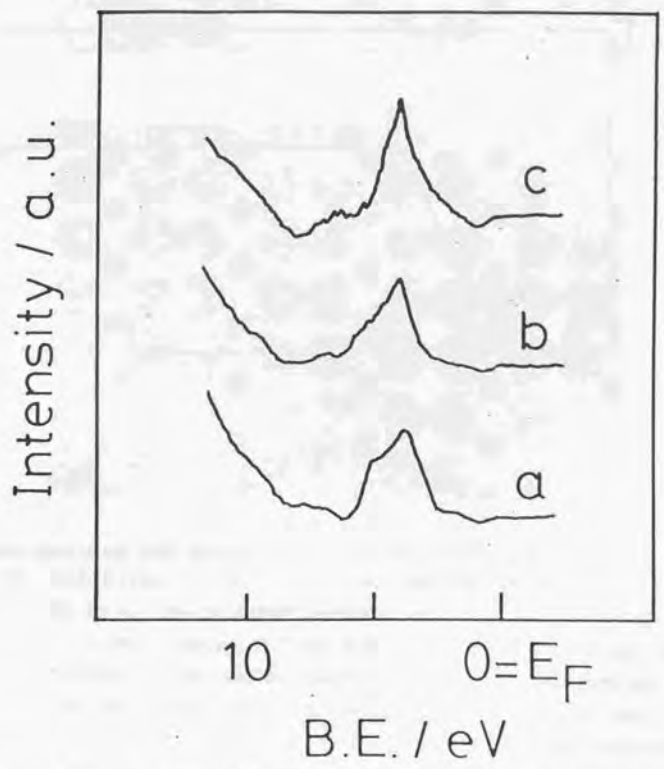

Fig.7-4. HeI UPS difference spectra upon NO adsorption on $Na/TiO_2(110)$ with (a): θ_{Na}=0.5 ML and (b): 0.9 ML. (c): recorded on a sputtered $TiO_2(110)$.

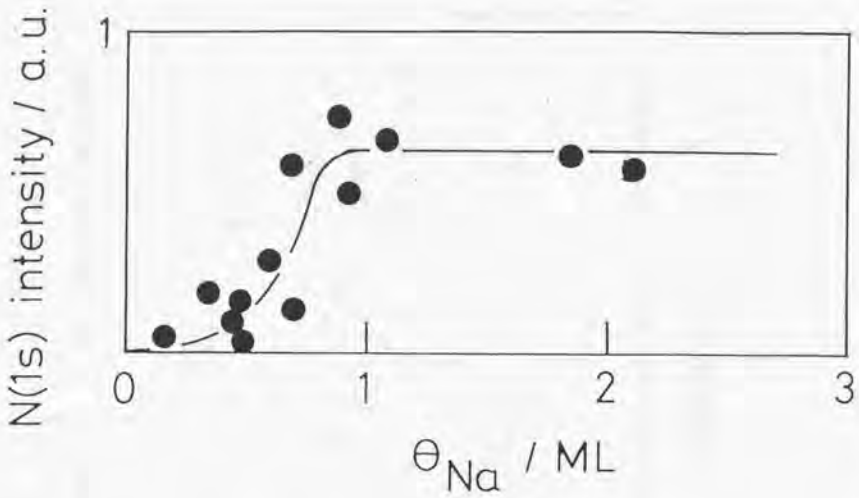

Fig.7-5. The intensity of N(1s) emission for nitride with the coverage of Na.

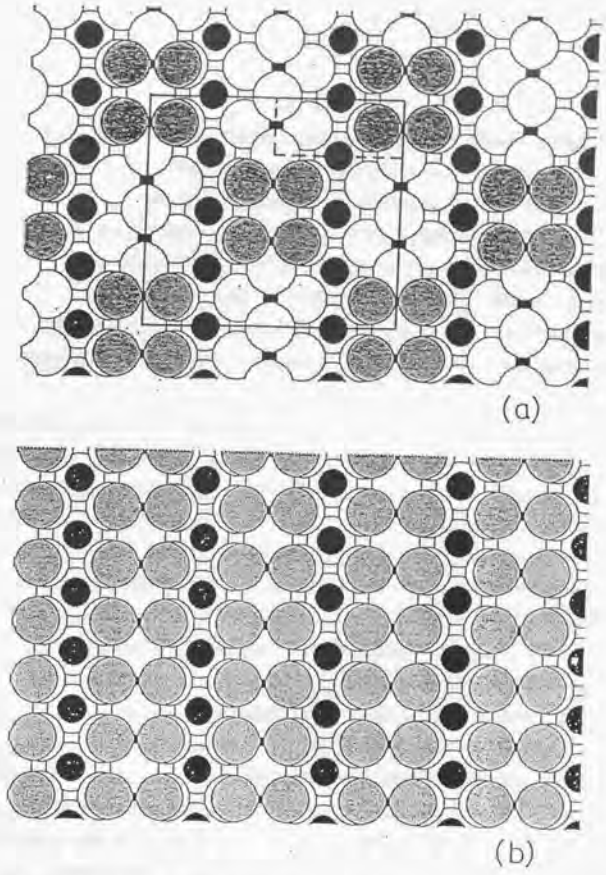

Fig.7-6. Illustration for (a) the c(4x2) overlayer at 0.5 ML of Na with "Na_2O-dimer" units; and (b) the (1x1) overlayer at 1 ML. Open, filled and hatched circles represent oxygen, titanium and sodium atoms, respectively. The vertical frame is parallel to the [001] direction. Solid and broken lines show a rectangular c(4x2) and (1x1) unit cells, respectively.

Chapter 8

Nickel adatoms on TiO_2(110)

8.1. Abstract

Nickel adatoms on a (110) surface of rutile are examined with XPS, AES, UPS and LEED. Nickel adatoms form an atomic layer at 300 K with a density of 8×10^{18} m^{-2}, followed by three-dimensional agglomelation. Forward scattering of photoelectrons of Ni(2p) level is analyzed to detect anisotropic crystallization of multi-layered islands. Work function decreases with Ni coverage having a minimum at 0.5 ML. The initial decrease by 0.7 eV evaluates an outward dipole of 0.5 Debye per Ni adatom. The dipole is attributed to an electron transfer into the substrate, less than 0.1 electron per Ni adatom. As overlayer grows dense, the lateral interaction between Ni adatoms overrides and inhibits the electron transfer. CO is molecularly adsorbed on the Ni/TiO_2(110) surfaces at 300 K. The saturated coverage of CO proportionally increases with Ni coverage within 1 ML.

8.2. Introduction

Metal-insulator interface plays an important role in heterogeneous catalysis. Catalytic properties of metal particle supported on metal oxide are often affected by the nature of the support [1] as well as the size of the metal particle [2]. Both the effects are attributed to interaction of metal with metal oxide. Few investigations, however, have been performed on well-characterized metal-insulator interfaces, though metal-metal or metal-semiconductor [5] interfaces has been extensively studied.

Here, nickel adatoms are examined on TiO_2(110) as a typical interface of transition metal and metal oxide. The morphology, the electronic states and the reactivity to carbon monoxide of the Ni adatoms are discussed. Nickel particles supported on TiO_2 powder exhibits a higher activity for the hydrogenation reaction of CO to mathane than nickel particles on other supports [3].

Rutile (110) surface has an open structure, where coordinatively unsaturated oxygen and titanium atoms lay ridges and ditches respectively along the [001] azimuth [4,6,7]. Although metal oxide is thought inert substrate in surface science, such an open structure is expected to interact with transition metal adatoms. A large electron transfer from sodium adatoms into TiO_2(110) substrate is detected on Na/TiO_2(110) interfaces, as shown in Chapter 6.

8.3. Experimental

All the experiments were carried out in a chamber (VG-ESCALAB). XPS spectrum excited by Mg-Kα radiation was recorded with a hemispherical analyser. The sample wafer was rotated in photoelectron diffraction measurement, while the X-ray source and the analyser were fixed. The binding energy in XPS was referred to O(1s) level of 530.3 eV in the substrate. Work function was measured from cutoff in HeI UPS [8].

A TiO_2(110) wafer was cleaned in annealing to 900 K under UHV by electron bombardment following Ar^+ sputtering. No contami-

nation was detected in XPS nor in AES. A clear (1x1) rectangular pattern was obtained in LEED. Nickel was evaporated with a Ni droplet welded on tungusten wire by resistive heating. The wafer was maintained at 300 K during deposition. The rate of Ni deposition was constant in a course of experiments. A capillary doser introduced CO molecules on the crystal.

8.4. Results and Discussion

8.4.1. Structure

Ni(2p3/2) emission of Ni deposits and X-ray excited O KLL emission of the substrate were monitored as a function of deposition time. Their peak height is plotted in Fig.8-1. There is a break at 18 min for both the signals, which is characteristic of a layer growth mode. No more break was observed until 50 min exposure, suggesting subsequent three-dimensional nucleation of Ni adatoms, i.e. the Stranski-Krastanov mechanism of growth [9]. The coverage of Ni is thus defined as 1 ML at 18 min. The surface density of the Ni monolayer was estimated to be 8×10^{18} m^{-2} on the intensity of Ni(2p3/2) emission compared with that of the O(1s) level, taking cross section and escape depth into account. A constant flux of Ni is also assumed here; it is reasonable because the source was stable enough in a course of experiments.

The intensity of Ni(2p3/2) emission was recorded further as a function of emission polar angle, to discuss morphology of Ni adlayers. Angular distribution of fast photoelectrons gives insights into a short range order around photoexcited atoms, because the photoelectrons are diffracted by overlying atoms. Attractive potential of the scattering nuclei gives a forward scattering and hence yields an enhanced diffraction along the axis connecting emitting and scattering atoms [10]. Ni(2p3/2) level has a kinetic energy of 440 eV enough for this analysis. Figure 8-2 shows the dependence of Ni(2p3/2) intensity on two kinds of off-normal polar angle, θ_{001} and $\theta_{1\bar{1}0}$, in the [001] and [1$\bar{1}$0] azimuth, respectively. The polar angle are defined to

be 0° at the surface normal. No diffraction can be distinguished from background below 1 ML, suggesting again a single atomic layer of Ni adatoms.

The adatoms starts to aggregate into islands atl ML, since an enhanced diffraction at 0° was observed at 1.2 ML in Figs.8-2A and 8-2B. New peaks grow at 0°, 10°, 30° and 45° in θ_{001} above 1 ML, demonstrating three-dimensional thickening of Ni adatoms. The diffraction at 0° suggests triply stuck island at least, because a crystalline double layer in fcc structure could not yield overlying atoms at the on-top position. Hence, the enhancement at 0° observed at 1.2 ML supports multilayered aggregation above 1 ML. Layer-by-layer grown deposits could not stick triply below 2 ML.

Assuming a crystalline sticking, the diffraction at 45° is attributed to nickel islands with (100) basal plane facing the substrate [10]. The peaks at 30° and 10° recorded above 2.5 ML can be assigned to a particle with (111) basal plane. A fcc crystal with (111) basal plane have enhancement at 30° and 20°. Platinum deposits on a TiO_2(110) surface form fcc-crystalline particles with their closed packed (111) plane facing the substrate after annealing at 823 K [11].

The sticking of the adatoms reflects the atomic channels on the substrate. Comparing Fig.8-2A and 8-2B, more pronounced enhancements are observed in θ_{001} axis than in $\theta_{1\bar{1}0}$ axis. They indicate that the adatoms crystallize better in the [001] direction, i.e. along the channels, than in the [1$\bar{1}$0] direction, i.e. across the channels, if it is assumed that the diffracted amplitude corresponds to the spatial distribution of Ni-Ni interatomic axis vector. The oxygen ridges perturb and prevent the deposits from crystallization across the channels.

No new long range order was observable in LEED during deposition. The background was increased in intensity without extra spots or streaks. This results from random location of the deposits over the substrate. Random location of the adatoms over the Ti cations is supported by photoelectron diffraction in Ti(2p3/2) level. The intensity is plotted with the two kinds of polar angles in Figs.8-3A and 8-3B at various coverages of the

deposits. They represents local coordination around titanium cations. There are four peaks at 0°, 25°, 40° and 55° for θ_{221} in Fig.8-3A, while enhancement is observed at 0°, 25° and 45° for θ_{112} in Fig.8-3B. The seven peaks are predicted on the crystal structure of rutile bulk. They were averaged out with larger nickel coverage, suggesting an averaged location of the deposits over the surface Ti cations.

A model for the nickel adatoms at 1 ML is illustrated in Fig.8-4. Here it is assumed that nickel atoms fill the channels on the substrate; the adatoms draw wavy lines in the ditches to squeeze as possible. A nickel atom has an atomic radius of 13 pm in the fcc crystal. (110) surface of rutile has a periodicity of 649 pm along the [1$\bar{1}$0] direction. Efficient width of a channel should be 370 pm, considering an ionic radius of 140 pm for O^{2-} anion. Thus, two nickel atoms could not stand side by side across a channel. The closed packed wavy arrays would give a Ni density of 8×10^{18} m^{-2} which is in a good agreement with the observed value. If subsequent aggregation occurs on these arrays, a prior crystallization along the [001] direction is expected.

Straight chain of rhodium atoms was observed on a polycrystalline catalyst. A TEM (Transmission electron microscopy) study reported linear images on a Rh/TiO_2 catalyst prepared by ion-exchange method [12]. They were assigned to nickel chains along the [001] direction on (110) facets of polycrystalline supports. The catalyst preparation including H_2 reduction was proposed to remove the ridges of oxygen anions to give a space enough for two Ni atoms to sit side by side [13].

8.4.2. Electronic states

Figure 8-5 shows work function with Ni coverage. Work function is one of the most direct measures of the net exchange of charge between adatom and substrate. The work function decreases straight from 5.3 eV to a minimum of 4.6 eV at 0.5 ML, and then turns into a saturated value of 4.8 eV. This type of behavior is often observed in alkali adatoms on transition metal,

and ascribed to electron transfer and resultant dipole [14]. Drawing an analogy to the case of alkali adatoms, an outward dipole of 0.5 Debye per Ni atom is estimated to reduce work function by 0.7 eV at 0.5 ML, where the estimated density of the adatoms is employed. The evaluated dipole per adatom is as small as 12% of that observed on Na/TiO_2(110) interface in Chapter 6. The electron transfer from Na adatoms to the substrate resulted in a dipole of 4.3 Debye per Na adatom. The small dipole of Ni adatom suggests that the amount of transferred electron is 0.1 electron per Ni adatom or less. Such a small ability of nickel in charge transfer reflects its large electronegativity of 1.8 on the Pauling's scale, compared with 0.9 for Na.

Electron transfer from transition metal adatoms to rutile was reported on Pt/TiO_2(100) by means of PAX (photoelectron spectroscopy of adsorbed xenon) [15]. PAX is a method to determine local surface potential. Platinum islands on a TiO_2 (100) has a deficient electron density, which increases the binding energy in the 5p3/2 level of Xe atoms physisorbed on the islands by 2 eV than that on bulk platinum [15].

Above 0.5 ML, the work function turned to increase into the value of Ni bulk. This indicates that Ni overlayers increase metallic property and reserve their electrons for themselves. The minimum demonstrates that the dipole decreases with the density of Ni adatoms. As Ni overlayer grows dense in the channels, each adatom has neighbouring Ni atoms to overlap their 3d orbitals to form and to stabilize 3d bands. The resultant metallic bands inhibits charge transfer, leading to the minimum in the work function [16].

An evolution of Ni 3d states was observed in HeI UPS. Some typical spectra are shown in Fig.8-6. The valence band at 3-9 eV is composed of O(2p) orbitals in the substrate. Ni 3d states grow just below the Fermi level with coverage. The emission are magnified into an equal height in Fig.8-7. The 3d states shift towards the Fermi level with broadening, being saturated above 0.8 ML. The shift and the broadening result from the formation of 3d-band in Ni adlayers. Evolution of d-bands was observed on Pd/SiO_2 [17] and Ni/TiO_2(110) [18] interfaces.

The binding energy in Ni(2p3/2) level is plotted with nickel coverage in Fig.8-8. A decrease of 0.4 eV until 1 ML is observed, followed by a residual small gradient above 1 ML. There are two possible origins for the shifts; partial ionization of nickel atoms is plausible first. A formal Ni^{2+} cation has a larger shift of 2.2 eV at ionization [19]. The observed shift of 0.4 eV is consistent with the estimated charge transfer of 0.1 electron or less. Second, final state relaxation should be considered for the core hole created with photoionization. If the nickel adatoms are poorly coordinated to restrict the delocalizing hole, apparent binding energy increases [20]. Additionally, the evolved 3d-band affects the hybridization among 4s, 4p and 3d states on Ni adatoms to alter the final relaxation. Neither Ti(2p3/2) nor O(1s) level shifted at all. The valence of Ti cations kept 4+ state, contrasting to Na/TiO_2(110) interface where reduced Ti^{3+} species are detected. The charge exchange on the Ni/TiO_2 interfaces is too small to reduce the cations.

Let me discuss the interaction between nickel adatoms and rutile substrate. Primarily, electron transfer is detected through the interfaces. Similar exchange was observed on Na/TiO_2(110), Na/MgO(111) and Pt/TiO_2(100) [15] interfaces. It thus seems a general feature on metal/metal-oxide interfaces, when substrate has its highest valence. Electron transfer in the reverse direction, from substrate to adatoms, was reported on Rh/reduced-TiO_2(110) [21], Ni/reduced-TiO_2(110) [18] and Ni/SiO_x/n-Si [22] interfaces; it is ascribed to one of the origins for the SMSI (strong metal-support interaction) phenomena [1] in catalytic chemistry. An inward dipole, however, was not observed in the present Ni/TiO_2(110) interfaces. Note that the substrate was not reduced here. The transferred electron is small, 0.1 electron per adatom or less. The small dipole and the consequent small lateral repulsion prevents the overlayer from ordering, having a contrast to alkali/metal [14], Na/TiO_2(110) and Cs/ZnO(000$\bar{1}$) [23] interfaces. The lateral interaction between Ni adatoms overrides and inhibits the electron transfer at higher coverage above 0.5 ML. The work function, Ni(2p) core level and

3d bands were saturated into those of Ni bulk at 4.8 ML, the largest coverage in the present experiments.

8.4.3. Chemisorption of CO

Carbon monoxide was molecularly adsorbed at 300 K on Ni/TiO_2(110) surfaces. 10^3 L of CO was exposed to the wafer. A single peak at 285.0 eV was observed in C(1s) region; it is a characteristic value for CO molecularly adsorbed on transition metals [24]. HeII UPS difference spectra upon CO exposure are shown in Fig.8-9. There are two peaks at 7.9 and 11.1 eV, assignable to $5\sigma+1\pi$ and 4σ orbitals of molecular CO. The former is barely distinguished from background at 0.3 ML, due to superimposed emission of the valence bands on the substrate. The molecular peaks keep binding energy against Ni coverage. Those results in XPS and UPS suggest that the bonding of molecular CO is not affected by the coverage and thickness of Ni deposits. It is consistent with a TPD study over Pt adatoms on Al_2O_3 crystal [25] where CO gives similar desorption peaks to Pt bulk.

An additional peak was detected at 4 eV in UPS; the signal is more prominent at less coverage in Fig.8-9. A possible origin for the peak is rearrangement in Ni 3d electrons induced by adsorbed CO. A LSD-SW (local spin density scattered wave) calculation for a on-top CO/Ni_9 cluster [26] predicted a "resonance peak" at 3-4 eV induced by CO, due to a readjustment of 3d electrons.

The coverage of molecular CO proportionally increased with the coverage of Ni adatoms until 1 ML, as shown in Fig.8-10. Constant affinity per Ni atom to CO is consistent with the spectroscopic results above. Residual increment beyond 1 ML is attributed to a slow increase in surface area of Ni deposits during three-dimensional thickening. The electron exchange observed on Ni/TiO_2(110) surfaces does not affect the bonding to molecular CO. This contrasts to a Ni/SiOx/n-Si interface [22] where transferred charge prohibited CO adsorption through the interface.

8.5. Conclusions

Nickel adatoms form an atomic layer on TiO_2(110) at 300 K, followed by three-dimensional aggregation. A small electron transfer less than 0.1 electron per adatom from the deposits into the substrate is detected below 0.5 ML. Neighboring adatoms form 3d band and inhibit the charge transfer in dense overlayers. The ridges and the ditches along the [001] direction on the substrate perturbed the crystallization of thick deposits. Carbon monoxide is adsorbed on the Ni adlayers in a constant manner against coverage despite the charge transfer.

8.6. References

1. G.L.Haller and D.E.Resasco, Adv.Catal.36(1989)173.
2. M.Che and C.O.Bennett, Adv.Catal.36(1989)55.
3. M.A.Vannice and R.L.Garten, J.Catal.56(1979)236.
4. V.E.Henrich and R.L.Kurtz, Phys.Rev.B36(1981)6280.
5. H.Yasunaga and A.Natori, Surf.Sci.Rept.15(1992).
6. R.H.Tait and R.V.Kasowski, Phys.Rev.B20(1979)5178.
7. Y.W.Chung, W.J.Lo and G.A.Somorjai, Surf.Sci.64(1977)588.
8. S.Evans, Chem.Phys.Lett.23(1973)134.
9. G.E.Rhead, J.Vac.Sci.Technol.13(1976)603.
10. W.F.Egelhoff,Jr., J.Vac.Sci.Tech.A2(1984)350.
11. K.Tamura, U.Bardi and Y.Nihei, Surf.Sci.216(1989)209.
12. S.Fuentes, A.Vázquez, J.G.Perez and M.J.Yacamán, J.Catal.99(1986)492.
13. H.R.Sadeghi, D.E.Resasco, V.E.Henrich and G.L.Haller, J.Catal.104(1987)252.
14. H.P.Bonzel, Surf.Sci.Rept.8(1987)43.
15. P.Dolle, K.Markert, W.Heichler, N.R.Armstrong, K.Wandelt, K.S.Kim and R.A.Fiato, J.Vac.Sci.Technol.A4(1986)1465.
16. T.Aruga, H.Tochihara and Y.Murata, Phys.Rev.B34(1986)8237.
17. S.Kohiki, Appl.Surf.Sci.25(1986)81.
18. C.C.Kao, S.C.Tsai, M.K.Bahl, Y.W.Chung and W.J.Lo, Surf.Sci.95(1980)1.
19. R.Holm and S.Storp, Appl.Phys.9(1976)217.
20. W.F.Egelhoff,Jr., Surf.Sci.Rept.6(1987)253.
21. H.R.Sadeghi and V.E.Henrich, J.Catal.109(1988)1.
22. T.Asakawa, K.Tanaka and I.Toyoshima, Langmuir 4(1988)521.
23. R.Leysen, B.J.Hopkins and P.A.Taylor, J.Phys.C8(1975)907.
24. S.Ishi and Y.Ohmo, Surf.Sci.143(1984)L405.
25. E.I.Altman and R.J.Gorte, Surf.Sci.172(1986)71.
26. F.Raatz and D.R.Salahub, Surf.Sci.156(1985)982.

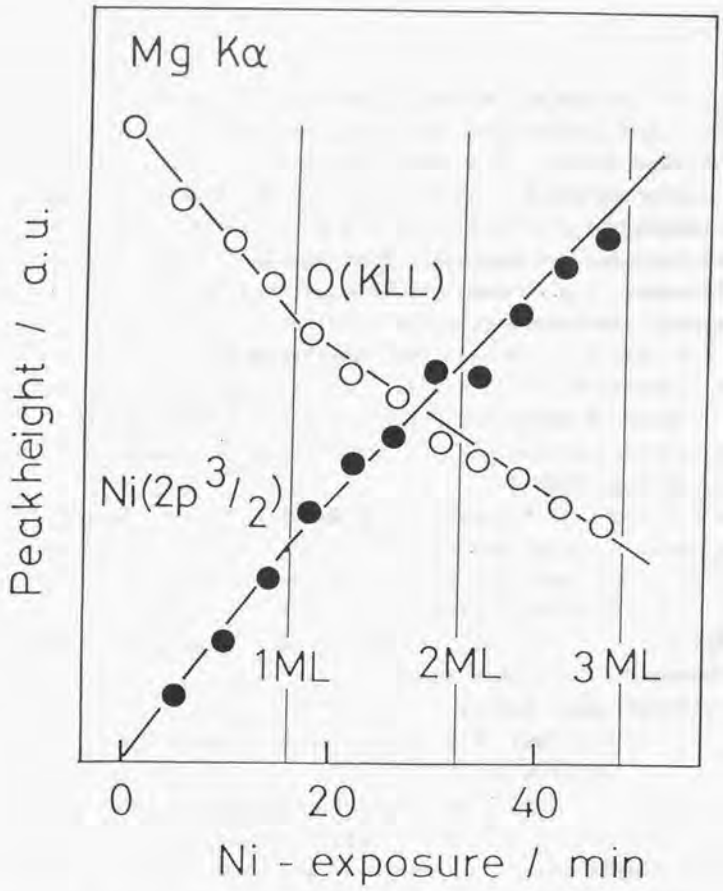

Fig.8-1. Peak height of Ni(2p3/2) and O KLL emissions as a function of deposition time at 300 K. Filled and open circles represent the emission of nickel and oxygen, respectively.

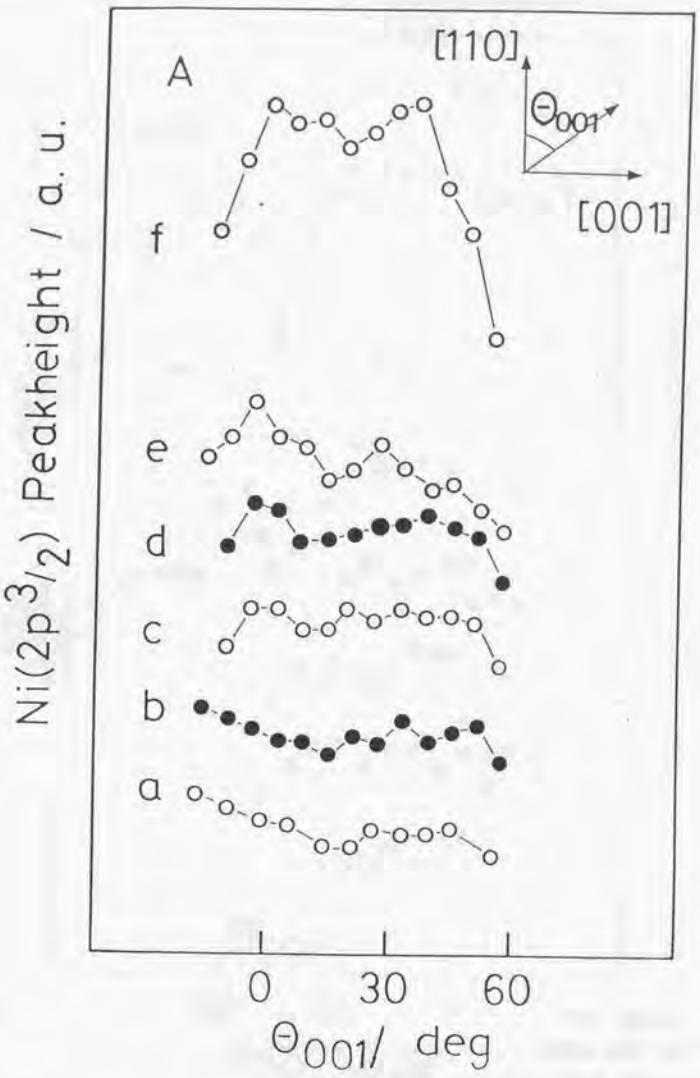

Fig.8-2. Angle resolved intensity in Ni(2p3/2) level as a function of a polar angle in (A) the [001] and (B) the [1$\bar{1}$0] azimuth. Curves (a)-(f) were recorded at 0.6, 1.0, 1.2, 1.9, 2.5 and 3.8 ML.

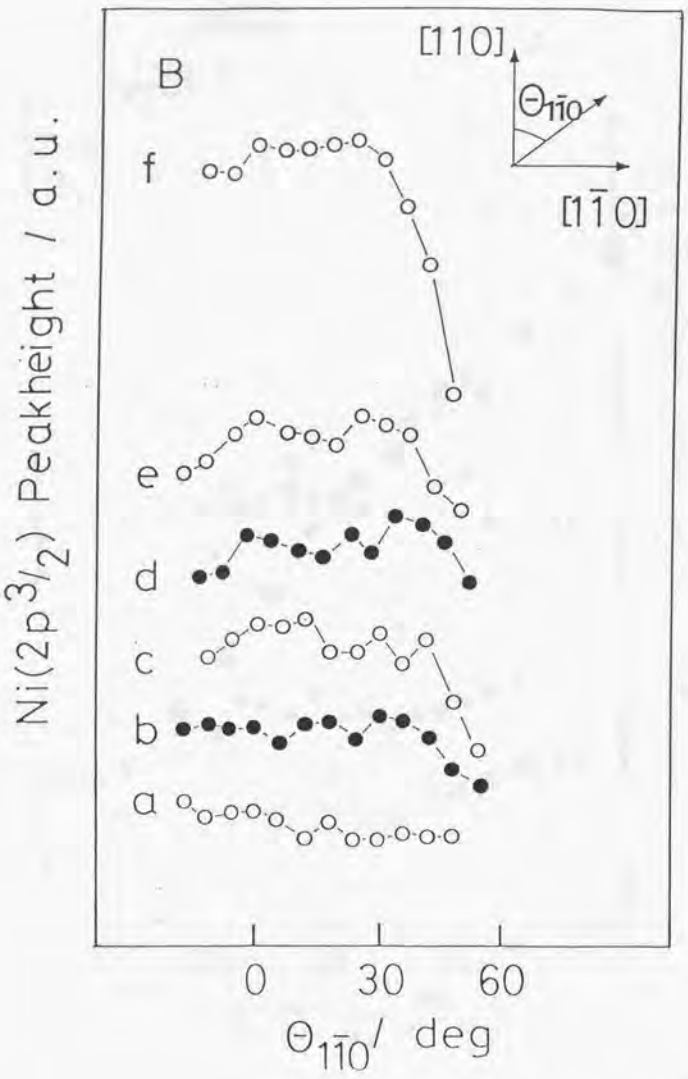

Fig.8-2. cintinued.

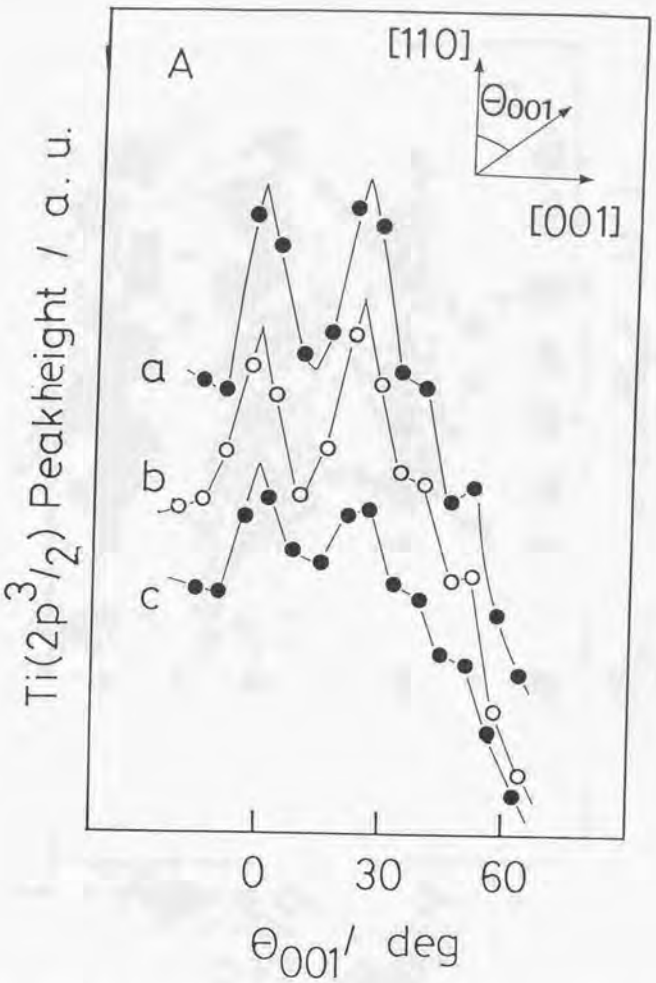

Fig.8-3. Angle resolved intensity in Ti(2p3/2) level as a function of a polar angle in (A) the [001] and (B) the [1$\bar{1}$0] azimuth. Curves (a),(b) and (c) were recorded on 1.2, 2.5 and 3.8 ML of Ni adlayers on the substrate.

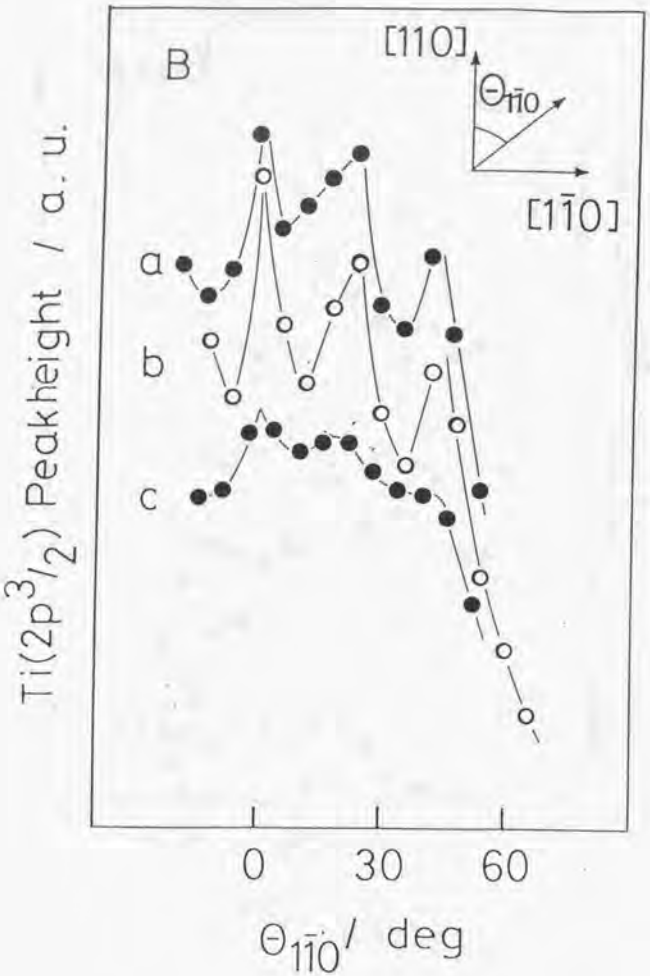

Fig.8-3. continued.

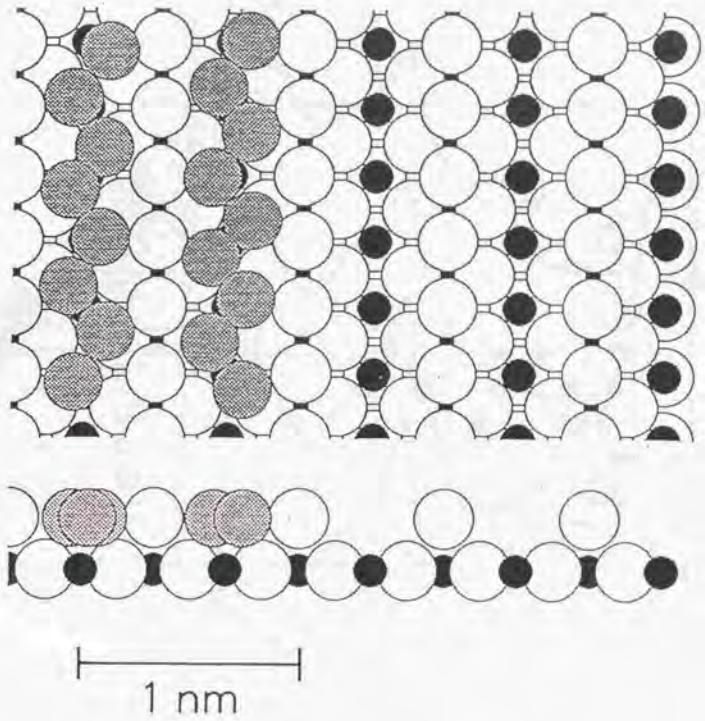

Fig.8-4. A model for Ni adatoms at 1 ML. Open, filled and shaded circles represent oxygen, titanium and nickel atoms, respectively. The upper panel shows an on-top view. A vertical section is in the lower panel. Nickel adatoms cover left two channels for illustration. The [1$\bar{1}$0] direction is horizontal the panels.

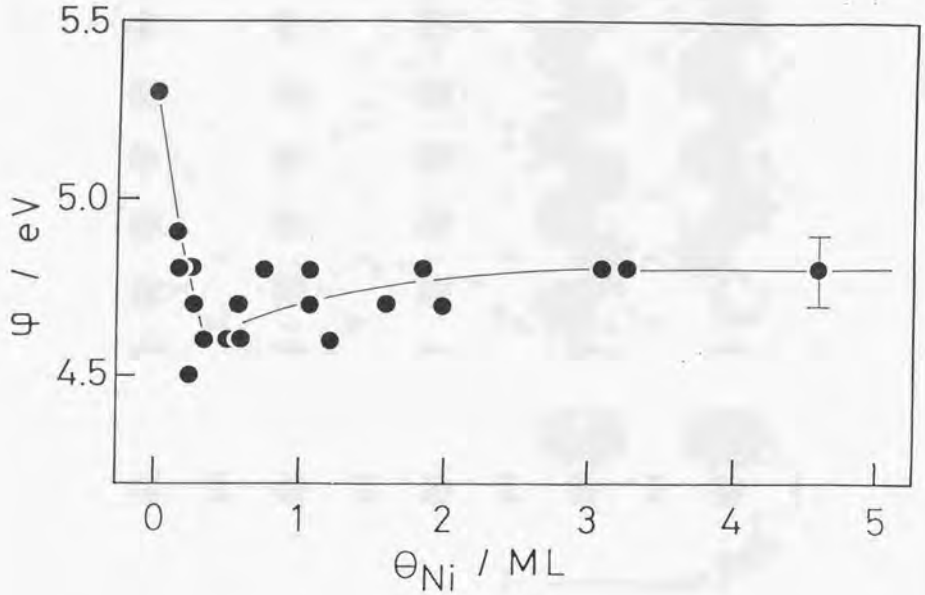

Fig.8-5. The work function on Ni/TiO_2(110) surfaces with Ni coverage.

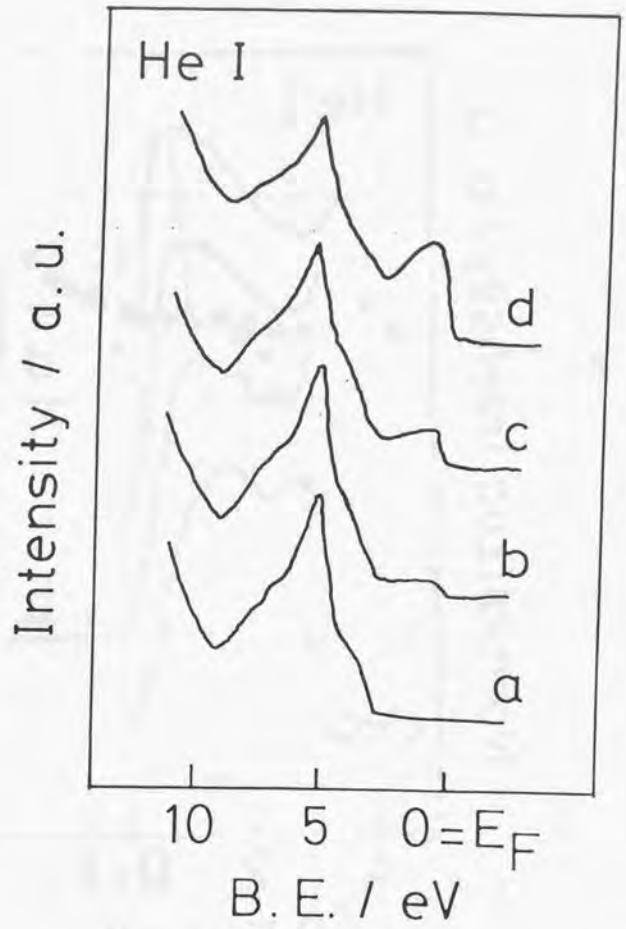

Fig.8-6. HeI UPS spectra on Ni/TiO_2(110) surfaces. (a): TiO_2(110); (b)-(d): recorded at 0.3, 0.8 and 3.0 ML. The spectra are normalized to equal height at the top of the valence bands.

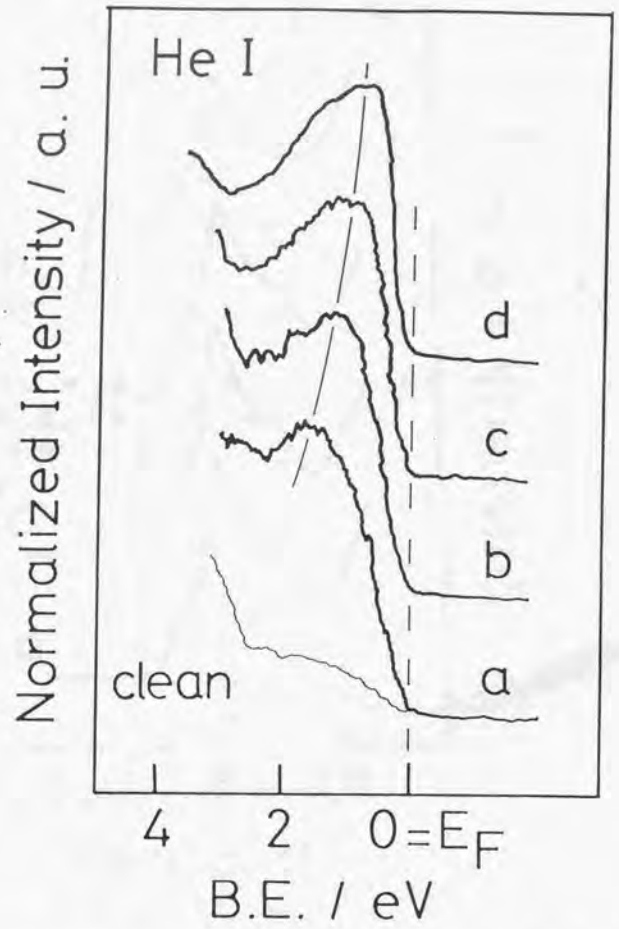

Fig.8-7. HeI UPS spectra just below the Fermi level E_F. (a)-(d) were recorded at 0.1, 0.5, 0.8 and 4.8 ML, respectively. A typical spectrum on TiO_2(110) is inserted with thin line for comparison.

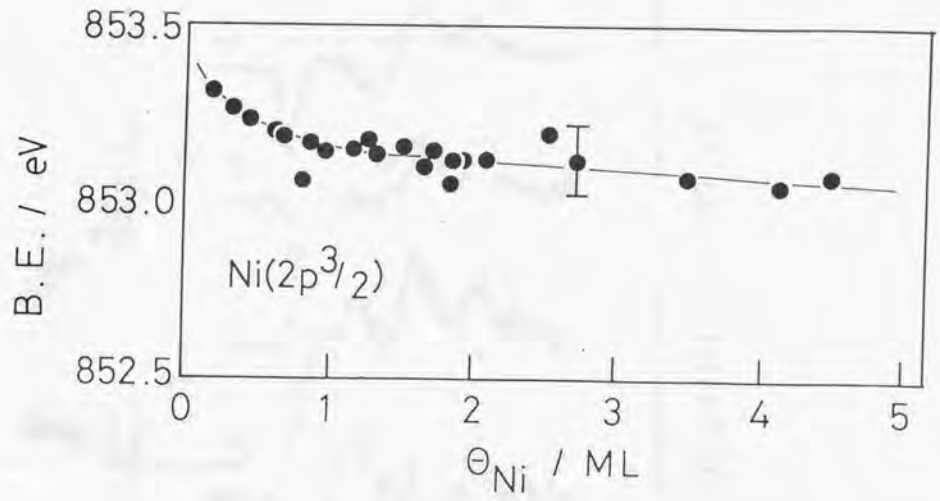

Fig.8-8. The binding energy in Ni(2p3/2) level of Ni adlayers with the coverage.

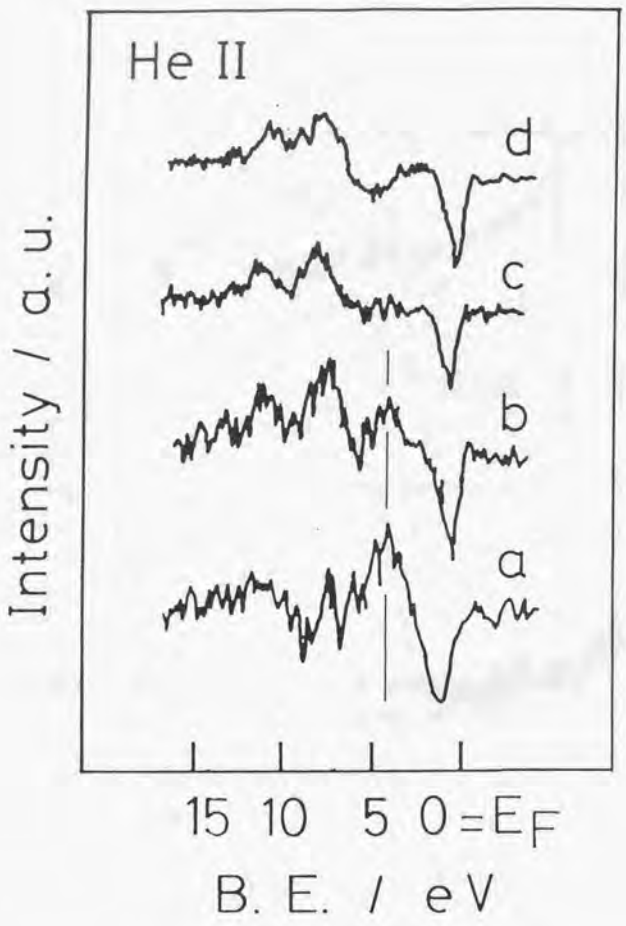

Fig.8-9. HeII UPS difference spectra upon 10^3 L CO exposure to $Ni/TiO_2(110)$ surfaces at 300 K. (a)-(d) were recorded with 0.3, 1.0, 1.6 and 7.0 ML of nickel adlayers, respectively.

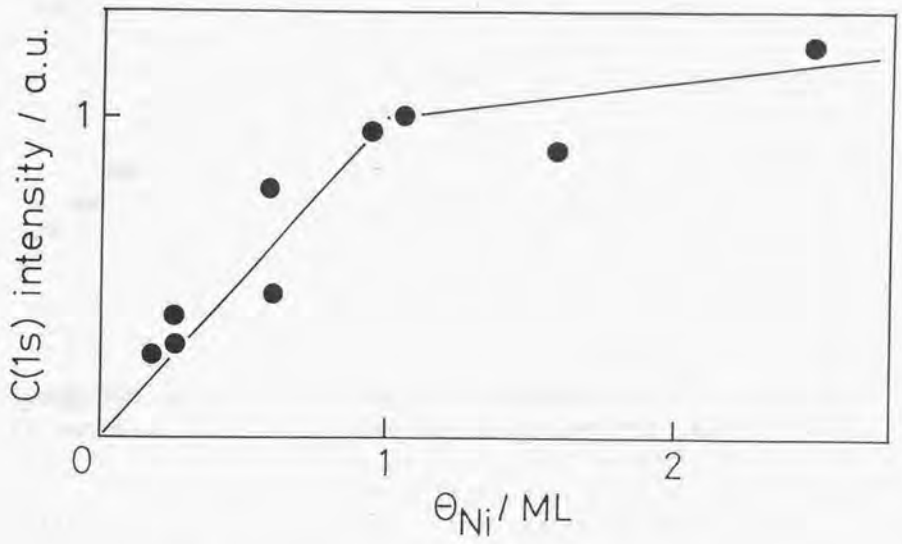

Fig.8-10. The intensity of C(1s) emission recorded following 10^3 L CO exposure on $Ni/TiO_2(110)$ as a function of Ni coverage. CO was exposed at 300 K.

Chapter 9

Concluding remarks

I have studied chemistry on well-defined surface of metal oxide. Chemisorption of atoms and molecules on pure surfaces is discussed in Chapter 3 and 4. Comparing a faceted (111) surface with a (100) surface, an enhanced reactivity on coordinatively unsaturated edge-sites is revealed on MgO. On the other hand, regular step structure on TiO_2(441) yields equivalent environments in local coordination as on (110) terrace. Several adsorbates cannot distinguish the steps on (441) surface from (110) plane, as a result. It is thus concluded that local coordination environment is the primary factor for chemisorption on metal oxide.

Catalytic decomposition reaction of formic acid is studied on TiO_2(110) in Chapter 5. Reactant molecules coexisting in gas phase drastically affect reaction mechanism and hence selectivity in a steady state. Unimolecular decomposition of adsorbed formate leads to selective dehydration reaction, while dehydrogenation reaction is catalyzed in a bimolecular process. Further catalytic studies on other surfaces, and also under higher pressure will help us to understand traditional acid-base character in the light of microscopic structure of reaction sites.

The latter three chapters deal with metal adatoms on TiO_2 (110). Sodium adatoms interact with the coordinative unsaturated oxygen anions on the substrate to be partially ionized, as shown in Chapter 6. The transferred charge causes a downward band bending in the substrate, to control the valence of Ti^{4+} cation through the position of the Fermi level. This type of electron transfer is also detected on Ni adatoms in a much smaller scale in Chapter 8. The electron transfer in this direction, from adatoms into substrate, seems a popular phenomenon over metal adatoms on metal oxide which is in its highest valence.

Chapter 7 demonstrates that the Na adatoms promote TiO_2(110) surface to adsorb carbon dioxide to form carbonate. An ensemble of four Na adatoms activates the surrounded oxygen anion on the substrate. The promoted anion nucleophilically attacks a CO_2 molecule. Note that the basic promotion requires an ensemble of adatoms.

Finally, I am getting believed through this work that surface chemistry is accessible on metal oxide crystals.

Acknowledgements

First of all, I give my greatest gratitude to Professor Y. Iwasawa. He introduced me to this fruitful field of surface chemistry. He also continued to guide me in my work. I hope to answer his confidence.

Professor C.Egawa and Dr. T.Aruga led me in this challenging work for 4 and 7 years, respectively. I started my career imitating them; how to design experiment, how to work under UHV condition, how to discuss result, etc.

Dr. K.Asakura gave me warm encouragement. I enjoyed stimulating discussion with Dr. R.Sekine on surface electronic states of metal oxide. Students in Iwasawa's group share my thanks for the exciting discussions on their and my works. Surface science groups in the Institute for Solid State Physics kindly allowed me to prepare sample wafers in their laboratories

Finally, I thank all the staffs in the Department of Chemistry for their technical and official supports.

Single Crystal Surfaces of Metal Oxides